Draft version February 12, 2019
Typeset using LaTeX **twocolumn** style in AASTeX62

Type Ia Supernovae are Excellent Standard Candles in the Near-Infrared

Arturo Avelino,[1] Andrew S. Friedman,[2] Kaisey S. Mandel,[3,4] David O. Jones,[5] Peter J. Challis,[1] and Robert P. Kirshner[1,6]

[1] *Harvard-Smithsonian Center for Astrophysics, 60 Garden Street, Cambridge, MA 02138*
[2] *University of California, San Diego, La Jolla, California 92093, USA*
[3] *Institute of Astronomy and Kavli Institute for Cosmology, Madingley Road, Cambridge, CB3 0HA, UK*
[4] *Statistical Laboratory, DPMMS, University of Cambridge, Wilberforce Road, Cambridge, CB3 0WB, UK*
[5] *University of California, Santa Cruz, Santa Cruz, California 95064, USA*
[6] *Gordon and Betty Moore Foundation, 1661 Page Mill Road, Palo Alto, CA 94304*

(Dated: February 12, 2019)

Submitted to ApJ

ABSTRACT

We analyze a set of 89 Type Ia supernovae (SN Ia) that have both optical and near-infrared (NIR) photometry to derive distances and construct low redshift ($z \leq 0.04$) Hubble diagrams. We construct mean light curve (LC) templates using a hierarchical Bayesian model. We explore both Gaussian process (GP) and template methods for fitting the LCs and estimating distances, while including peculiar velocity and photometric uncertainties. For the 56 SN Ia with both optical and NIR observations near maximum light, the GP method yields a NIR-only Hubble-diagram with a RMS of 0.117 ± 0.014 mag when referenced to the NIR maxima. For each NIR band, a comparable GP method RMS is obtained when referencing to NIR-max or B-max. Using NIR LC templates referenced to B-max yields a larger RMS value of 0.138 ± 0.014 mag. Fitting the corresponding optical data using standard LC fitters that use LC shape and color corrections yields larger RMS values of 0.179 ± 0.018 mag with SALT2 and 0.174 ± 0.021 mag with SNooPy. Applying our GP method to subsets of SN Ia NIR LCs at NIR maximum light, even without corrections for LC shape, color, or host-galaxy dust reddening, provides smaller RMS in the inferred distances, at the ~ 2.3-4.1σ level, than standard optical methods that do correct for those effects. Our ongoing RAISIN program on the Hubble Space Telescope will exploit this promising infrared approach to limit systematic errors when measuring the expansion history of the universe to constrain dark energy.

Keywords: distance scale – supernovae: cosmology, general, infrared observations, optical observations, photometry

1. INTRODUCTION

The increasing sample of high quality, low-redshift (low-z), near-infrared (NIR) light curves (LCs) of Type Ia supernovae (SN Ia) provides an opportunity to further investigate their utility as cosmological standard candles. Optical samples of SN Ia are large enough now that systematic uncertainties are major limitation to accurate cosmological constraints. Infrared observations of SN Ia can help in that essential way because supernovae are more nearly standard candles in the NIR and the effects of dust are diminished. This paper explores ways to use NIR observations of SN Ia to measure distances. This investigation is for a low-z sample, but we are working to extend this technique to cosmologically-interesting distances with the Hubble Space Telescope (HST).

Before NIR photometry became practical for large samples of SN Ia, photometry and spectroscopy of SN Ia at optical wavelengths enabled the unexpected 1998 dis-

aavelino@cfa.harvard.edu
asf@ucsd.edu

covery of cosmic acceleration (Riess et al. 1998; Schmidt et al. 1998; Perlmutter et al. 1999). Since then, a suite of independent cosmological methods has confirmed the SN Ia results (see Frieman et al. 2008; Weinberg et al. 2013 for reviews). The prevailing view is that the mechanism behind cosmic acceleration is some form of dark energy. The constraints on cosmological parameters from the SN Ia Pantheon sample (Scolnic et al. 2018) combined with the Planck 2015/2018 Cosmic Microwave Background data (Planck Collaboration et al. 2016b, 2018), as well as Baryon Acoustic Oscillations (Alam et al. 2017) and local Hubble constant measurements (Riess et al. 2016, 2018c,b,a) are consistent with this view. Among the major cosmological techniques, SN Ia provide precise measurements of extragalactic distances and the most direct evidence for cosmic acceleration (see Goobar & Leibundgut 2011; Kirshner 2013; Goobar 2015; Davis & Parkinson 2016; Riess et al. 2018c for reviews).

Optical SN Ia LCs are known to be excellent *standardizable* candles that exploit correlations between intrinsic luminosity and LC shape and color (Phillips 1993; Phillips et al. 1999; Hamuy et al. 1996; Riess et al. 1996, 1998; Perlmutter et al. 1997; Goldhaber et al. 2001; Tonry et al. 2003; Wang et al. 2003; Prieto et al. 2006; Jha et al. 2006, 2007; Astier et al. 2006; Takanashi et al. 2008; Conley et al. 2008; Mandel et al. 2009; Guy et al. 2005, 2007, 2010; Mandel et al. 2011, 2017). Recent work has demonstrated that SN Ia in the NIR are more nearly *standard* candles, even before correction for LC shape or host galaxy dust reddening (e.g. Krisciunas et al. 2004a; Wood-Vasey et al. 2008; Mandel et al. 2009; Krisciunas et al. 2009; Friedman 2012; Kattner et al. 2012). NIR LCs are ∼5–11 times less sensitive to dust extinction than optical B-band data (Cardelli et al. 1989). When constructing SN Ia Hubble diagrams using NIR data, the distance errors produced by extinction are small: ignoring dust would be fatal for optical studies, but nearly not as serious for NIR studies like Wood-Vasey et al. 2008 or the present work. An improved approach would use optical and infrared data simultaneously to determine the extinction (Mandel et al. 2011).

Optical-only samples yield typical Hubble diagram intrinsic scatter of $\sigma_{\rm int} \sim 0.12$ mag and a RMS of 0.141 mag after applying light-curve shape, host-galaxy dust, and host-galaxy mass corrections, assuming a peculiar-velocity uncertainty of 250 km s^{-1} (e.g. Scolnic et al. 2018). For simplicity, we adopt a conservative peculiar-velocity uncertainty for the host galaxies in our sample of 150 km s^{-1}. If the typical redshifts in the sample were large enough, this would be of no consequence, but for our nearby sample, the inferred intrinsic scatter of the supernova luminosities depends on the value we choose. As a result, though we have confidence when comparing the RMS and intrinsic scatter for various subsamples containing the same SN with both optical and infrared data, the real value of the scatter should be determined from observations that are securely in the Hubble flow beyond 10,000 km s^{-1}.

When including a peculiar-velocity uncertainty of 150 km s^{-1}, our best method yields intrinsic scatters as small as $\sim$ 0.03-0.11 mag, depending on the NIR filter subset, and a RMS of $\sim 0.087 \pm 0.013$ mag for the best NIR YJH-band subset, confirming and strengthening previous results for NIR methods (Meikle 2000; Krisciunas et al. 2004a, 2005, 2007; Folatelli et al. 2010; Burns et al. 2011; Wood-Vasey et al. 2008; Mandel et al. 2009, 2011; Kattner et al. 2012; Dhawan et al. 2015). Assuming a larger peculiar-velocity uncertainty, such as 250 km s^{-1}, makes our estimated intrinsic scatter even *smaller*. In addition, our best NIR method using any of the $YJHK_s$ bands yields an RMS of only 0.117 ± 0.014 mag, compared to 0.179 ± 0.018 mag and 0.174 ± 0.021 mag for SALT2 and SNooPy fits to optical BVR data for the same 56 SN Ia, respectively. While using LC shape, color, and host galaxy dust corrections would likely lead to improvements, the simpler approaches in this paper are still remarkably effective.

Overall, a substantial body of evidence indicates that rest-frame LCs of SN Ia in NIR are both better standard candles than at optical wavelengths and less sensitive to the confounding effects of dust. When NIR data are combined with $UBVRI$ photometry, this yields accurate and precise distance estimates (Krisciunas et al. 2004b, 2007; Wood-Vasey et al. 2008; Folatelli et al. 2010; Burns et al. 2011; Friedman 2012; Phillips 2012; Kattner et al. 2012; Burns et al. 2014; Mandel et al. 2009, 2011, 2014, 2017).

This is significant for supernova cosmology because, along with photometric-calibration uncertainties (Scolnic et al. 2015; Foley et al. 2018), uncertain dust extinction estimates and the intrinsic variability of SN Ia colors present challenging and important systematic problems for dark energy measurements (Wang et al. 2006; Jha et al. 2007; Wood-Vasey et al. 2007; Hicken et al. 2009a; Kessler et al. 2009; Guy et al. 2007, 2010; Conley et al. 2007, 2011; Komatsu et al. 2011; Campbell et al. 2013; Rest et al. 2013; Scolnic et al. 2013; Narayan 2013; Betoule et al. 2014; Rest et al. 2014; Mosher et al. 2014; Scolnic et al. 2014b,a, 2015; Narayan et al. 2016; Scolnic et al. 2017; Mandel et al. 2017; Foley et al. 2018; Scolnic et al. 2018; Brout et al. 2018a; Kessler et al. 2018). Combining optical and NIR LCs promises to reduce these systematic distance uncertainties (Folatelli et al. 2010; Burns et al. 2011; Kattner et al. 2012; Mandel et al. 2011, 2014).

This work is organized as follows. In §2, we review previous results with SN Ia in NIR, detail our analysis selection criteria, and discuss host galaxy redshifts. In §3, we outline our Gaussian process (GP) procedure to fit LCs and our hierarchical Bayesian model to construct mean $YJHK_s$ LC templates. In §4, we use these templates and GP fits to individual LCs to construct Hubble diagrams in each NIR band, as well as a combined $YJHK_s$ NIR Hubble diagram. We compare this to optical BVR Hubble diagrams for the very same set of 56 supernovae that use the SALT2 and SNooPy LC fitters. We end with §5 by documenting how, even without correcting for LC shape or dust, SN Ia in the NIR using our GP fits at NIR maximum are better standard candles than optical SN Ia observations corrected for these effects. Mathematical details of the Gaussian process, the hierarchical Bayesian model, and the method for determining the intrinsic scatter are presented in the Appendices.

2. SN Ia IN NIR AS STANDARD CANDLES

Pioneering studies by Meikle (2000) and Krisciunas et al. (2004a) demonstrated that SN Ia have smaller luminosity variation in the NIR JHK_s bands than in the optical BV bands at the time of B-band maximum light ($t_{\rm Bmax}$). Krisciunas et al. (2004a) found that optical LC shape and intrinsic NIR luminosity were uncorrelated in a sample of 16 SN Ia, while measuring a NIR absolute magnitude scatter of $\sigma_J = 0.14$, $\sigma_H = 0.18$, and $\sigma_{K_s} = 0.12$ mag. Following this, Wood-Vasey et al. (2008) used a homogeneously-observed sample of 18 spectroscopically-normal SN Ia in the JHK_s bands, with intrinsic root-mean-square (RMS) absolute magnitudes of 0.15 mag in the H-band, *without applying any reddening or LC shape corrections*. By combining these 18 objects with 23 SN Ia from the literature, the sample in Wood-Vasey et al. (2008) yielded an H-band RMS of 0.16 mag, strengthening the evidence that normal SN Ia are excellent NIR standard candles. In the present work, we show that SN Ia in NIR yield a narrow distribution of $YJHK_s$ peak magnitudes with RMS Hubble Diagram scatter as small as 0.087 ± 0.013 mag for the combined YJH bands and as large as 0.179 ± 0.029 mag for the K_s band, consistent with previous results.

Following Wood-Vasey et al. 2008, Mandel et al. 2009 developed a new hierarchical Bayesian model (BayeSN) and a template model to account for J-band LC shape variation to the existing SN Ia in NIR sample, finding a marginal scatter in the peak absolute magnitudes of 0.17, 0.11, and 0.19 mag, in JHK_s, respectively, while finding that J-band LC shape does correlate with NIR intrinsic luminosity. Subsequent work by Folatelli et al. 2010 applied a different LC shape correction method, but found scatters of 0.12–0.16 mag in $YJHK_s$, consistent with the results of Mandel et al. (2009).

Additional work by Kattner et al. (2012) found an absolute magnitude scatter of 0.12, 0.12, and 0.09 mag in YJH, respectively, by analyzing a subset of 13 well-sampled normal NIR SN Ia LCs with relatively little host galaxy dust extinction. Kattner et al. 2012 also showed evidence for a correlation between the JH-band absolute magnitudes at $t_{\rm Bmax}$ and, $\Delta m_{15}(B)$, the light-curve decline rate parameter in B-band after 15 days of $t_{\rm Bmax}$ (Phillips 1993), with no evidence for strong correlation in the Y-band. This is also consistent with the results of Mandel et al. 2009, who found that J-band LC shape and luminosity are correlated.

Using a small data set of 12 SN Ia JH-band LCs, each with only 3-5 data points, Barone-Nugent et al. 2012, 2013 find a scatter of 0.116 mag and 0.085 mag in the J and H-bands, respectively. In the first data release of the SweetSpot survey, Weyant et al. 2014 present a similarly small sample of 13 low-z SN Ia, each with 1-3 LC points, finding an H-band scatter of 0.164 mag. This was followed by a second SweetSpot data release, which included a total of 33 SN Ia with 168 JHK_s observations in the redshift range $0.02 < z < 0.09$, well into the smooth Hubble flow, but which did not yet include NIR Hubble diagrams (Weyant et al. 2018).

By analyzing 45 NIR LCs with data near NIR-maximum, Stanishev et al. 2018 find an intrinsic Hubble diagram scatter of ~ 0.10 mag, after accounting for potential new correlations between light curve shape, color excess, and $J-H$ color at NIR-max. Stanishev et al. 2018 also present single-epoch JH photometry for 16 new SN Ia with $z > 0.037$. The Carnegie Supernova Project (CSP) final data release (CSP-I; Krisciunas et al. 2017), was recently analyzed in Burns et al. (2018), which found peculiar velocity corrected Hubble diagram dispersions of $\sim 0.08 - 0.15$ mag, depending on the subset of the 120 SN Ia they considered. Additional CSP-II photometric data, to be published in 2019, was recently described in Phillips et al. 2019. Hsiao et al. (2019) present an overview of the NIR SN Ia spectroscopy obtained by the CSP and the Center for Astrophysics (CfA) Supernova Group.

While the current sample of optical SN Ia LCs exceeds 1000 (Scolnic et al. 2018), and will be increased by orders of magnitude by ongoing and future surveys including the Dark Energy Survey (DES; DES Collaboration et al. 2018a,b; Brout et al. 2018b; D'Andrea et al. 2018), the

Zwicky Transient Facility (ZTF; Smith et al. 2014), and the Large Synoptic Survey Telescope (LSST; Ivezic et al. 2008; Zhan & Tyson 2017), the number of normal SN Ia with published NIR LCs is still less than 250. Nevertheless, the NIR sample has the potential to improve systematics compared to optical-only SN Ia cosmology samples, which are already systematics limited (Scolnic et al. 2018).

Overall, the growing sample of photometric data suggests that NIR observations of SN Ia present a promising path to standardize SN Ia for distance estimates (Dhawan et al. 2015; Shariff et al. 2016; Burns et al. 2018; Stanishev et al. 2018), Hubble constant estimates (Cartier et al. 2014; Efstathiou 2014; Riess et al. 2016; Cardona et al. 2017; Dhawan et al. 2018; Burns et al. 2018), and eventually, cosmological parameter estimates, when the nearby and high-z samples are combined as in the HST RAISIN program (**RAISIN**: *Tracers of cosmic expansion with* **SN IA** *in the* **IR**, PI. R. Kirshner, HST GO-13046, GO-14216).

2.1. *Nearby SN Ia in NIR Sample and Data Cuts*

This work analyzes a suitable subset including 89 objects from the current sample of low-redshift photometric data for SN Ia NIR $YJHK_s$-band LCs including data releases 1 and 2 from the Carnegie Supernova Project (Schweizer et al. 2008; Contreras et al. 2010; Stritzinger et al. 2010, 2011; Taddia et al. 2012), now superseded by CSP data release 3 (Krisciunas et al. 2017), the CfA (Wood-Vasey et al. 2008; Friedman 2012; Friedman et al. 2015), and other groups (e.g. Krisciunas et al. 2000, 2004b,c, 2005, 2007). We limit our analysis to spectroscopically normal SN Ia from Table 3 of Friedman et al. 2015, plus the definitive version of the CSP-I DR3 sample of low-z SN Ia (Krisciunas et al. 2017), and other groups. Additional CSP-II photometric data, to be published in 2019, was recently described in Phillips et al. 2019 and will be analyzed in future work. We apply the following data cuts to analyze a subset of 89 SN Ia with NIR data. Table 1 shows how the initial sample of 177 SN Ia decreases after applying the different cuts, and Table 2 lists the general properties of the remaining 89 SN Ia. We determine $\Delta m_{15}(B)$ and $E(B-V)_{\rm host}$ with SNooPy.

- Optical light curve shape parameter $0.8 < \Delta m_{15}(B) < 1.6$, to consider *normal* SN Ia only (Hicken et al. 2009b). Objects must have accompanying B-band optical data to measure $\Delta m_{15}(B)$.
- Host galaxy reddening: $-0.15 < E(B-V)_{\rm host} < 0.4$. This cut is inspired by the standard SALT2 cut in color, $-0.3 < c < 0.3$, in optical-only analysis (Betoule et al. 2014; Scolnic et al. 2018) but with a less stringent cut considering that SN Ia in the NIR are less sensitive to dust.
- One advantage of the relative NIR insensitivity to dust reddening is that it also allows us to set a large threshold for Milky Way color excess: $E(B-V)_{\rm MW} < 1$ mag, to exclude highly reddened SN Ia. All 177 SN Ia in the sample passed this cut. SN2006lf with $E(B-V)_{\rm MW} = 0.8135$ mag has the largest color excess in the initial sample.
- Redshift range: $z < 0.04$. The maximum redshift cut limits the effects of Malmquist bias. Section 2.2 describes corrections to deal with SN Ia at $z < 0.01$, that suffer from peculiar velocity bias.
- Duplicates: For a given supernova observed by multiple surveys, we use the CSP data (Krisciunas et al. 2017), which typically has smaller photometric uncertainties than the CfA PAIRITEL data (Friedman et al. 2015).
- We include only spectroscopically normal SN Ia as identified by the Supernova Identification Code (SNID) Blondin & Tonry (2007).
- At least 3 photometric points in a given band for each SN Ia LC. A large fraction of the NIR data from Barone-Nugent et al. (2012), Stanishev et al. (2018), and the SweetSPOT survey with WIYN (Weyant et al. 2014, 2018) did not meet this criterion, so we chose not to analyze these data in this work.

Table 1. Data cuts

Cuts	# SN Ia after cuts
Initial sample	177
$0.8 < \Delta m_{15} < 1.6$	138
$-0.15 < E(B-V)_{\rm host} < 0.4$	122
$E(B-V)_{\rm MW} < 1$	122
$z_{\rm CMB} < 0.04$	111
Remove duplicates	100
Normal spectrum	95
≥ 3 LC points	89

Reduction of the initial sample based on data cuts

2.2. *Host Galaxy Redshifts*

Heliocentric galaxy recession velocities and CMB frame redshifts are shown in Tables 2 and 3. We obtained heliocentric host galaxy recession velocities using

Table 2. SN Ia Light Curve Parameters

SN name	$z^a_{(\mathrm{helio})}$	z^b_{CMB}	σ^c_{pec} (mag)	LC Data Source[d]	$t^e_{B\max}$ (MJD days)	$\Delta m_{15}(B)^f$ (mag)	$E(B-V)^g_{\mathrm{host}}$ (mag)	$E(B-V)^h_{\mathrm{MW}}$ (mag)
SN1998bu	0.0030 ± 0.000003	0.0025 ± 0.00023	0.475	CfA	50953.11 ± 0.08	1.076 ± 0.012	0.351 ± 0.006	0.022 ± 0.0002
SN1999ee	0.0114 ± 0.000010	0.0112 ± 0.00050	0.137	CSP	51469.61 ± 0.04	0.802 ± 0.007	0.384 ± 0.004	0.017 ± 0.0001
SN1999ek	0.0176 ± 0.000007	0.0178 ± 0.00050	0.086	K04c	51482.60 ± 0.19	1.113 ± 0.031	0.277 ± 0.014	0.479 ± 0.0187
SN2000bh	0.0229 ± 0.000027	0.0240 ± 0.00050	0.064	CSP	51636.16 ± 0.25	1.055 ± 0.019	0.065 ± 0.012	0.047 ± 0.0064
SN2000ca	0.0236 ± 0.000200	0.0239 ± 0.00050	0.064	CSP	51666.25 ± 0.18	0.917 ± 0.019	-0.033 ± 0.010	0.057 ± 0.0025
SN2000E	0.0047 ± 0.000003	0.0056 ± 0.00050	0.273	V03	51577.20 ± 0.13	1.041 ± 0.027	0.217 ± 0.011	0.319 ± 0.0086
SN2001ba	0.0296 ± 0.000033	0.0302 ± 0.00050	0.051	CSP	52034.47 ± 0.17	0.997 ± 0.020	-0.072 ± 0.009	0.054 ± 0.0017
SN2001bt	0.0146 ± 0.000033	0.0142 ± 0.00050	0.108	K04c	52064.69 ± 0.07	1.199 ± 0.009	0.216 ± 0.008	0.056 ± 0.0007
SN2001cn	0.0152 ± 0.000127	0.0154 ± 0.00050	0.100	K04c	52071.93 ± 0.19	1.044 ± 0.012	0.176 ± 0.008	0.051 ± 0.0008
SN2001cz	0.0155 ± 0.000027	0.0171 ± 0.00050	0.090	K04c	52104.10 ± 0.10	0.956 ± 0.014	0.136 ± 0.008	0.079 ± 0.0005
SN2001el	0.0039 ± 0.000007	0.0045 ± 0.00014	0.000	K03	52182.38 ± 0.10	1.080 ± 0.019	0.277 ± 0.010	0.012 ± 0.0003
SN2002dj	0.0094 ± 0.000003	0.0083 ± 0.00152	0.421	P08	52451.04 ± 0.14	1.111 ± 0.019	0.093 ± 0.013	0.082 ± 0.0009
SN2003du	0.0064 ± 0.000013	0.0094 ± 0.00035	0.000	St07	52766.01 ± 0.09	1.010 ± 0.015	-0.033 ± 0.010	0.008 ± 0.0008
SN2003hv	0.0056 ± 0.000037	0.0049 ± 0.00034	0.267	L09	52891.49 ± 0.11	1.501 ± 0.006	-0.092 ± 0.007	0.013 ± 0.0008
SN2004ef	0.0310 ± 0.000017	0.0301 ± 0.00050	0.051	CSP	53264.90 ± 0.05	1.422 ± 0.011	0.116 ± 0.006	0.046 ± 0.0013
SN2004eo	0.0156 ± 0.000003	0.0152 ± 0.00050	0.101	CSP	53278.90 ± 0.04	1.318 ± 0.006	0.077 ± 0.005	0.093 ± 0.0010
SN2004ey	0.0158 ± 0.000003	0.0154 ± 0.00050	0.100	CSP	53304.81 ± 0.04	1.025 ± 0.011	0.006 ± 0.004	0.120 ± 0.0139
SN2004gs	0.0274 ± 0.000007	0.0287 ± 0.00050	0.054	CSP	53356.75 ± 0.05	1.546 ± 0.006	0.189 ± 0.006	0.026 ± 0.0006
SN2004S	0.0093 ± 0.000003	0.0107 ± 0.00050	0.143	K07	53040.00 ± 0.29	1.052 ± 0.021	0.112 ± 0.014	0.086 ± 0.0014
SN2005bo	0.0139 ± 0.000027	0.0144 ± 0.00050	0.107	CfA	53479.63 ± 0.15	1.310 ± 0.020	0.272 ± 0.007	0.044 ± 0.0006
SN2005cf	0.0064 ± 0.000017	0.0069 ± 0.00036	0.000	CfA	53534.31 ± 0.06	1.072 ± 0.023	0.088 ± 0.010	0.084 ± 0.0013
SN2005el	0.0149 ± 0.000017	0.0153 ± 0.00050	0.101	CSP	53647.42 ± 0.04	1.370 ± 0.006	-0.102 ± 0.005	0.098 ± 0.0004
SN2005iq	0.0340 ± 0.000123	0.0336 ± 0.00050	0.046	CSP	53688.14 ± 0.06	1.280 ± 0.012	-0.049 ± 0.006	0.018 ± 0.0007
SN2005kc	0.0151 ± 0.000003	0.0145 ± 0.00050	0.106	CSP	53698.31 ± 0.08	1.112 ± 0.023	0.350 ± 0.012	0.114 ± 0.0023
SN2005ki	0.0195 ± 0.000010	0.0203 ± 0.00050	0.076	CSP	53706.01 ± 0.04	1.365 ± 0.004	-0.065 ± 0.004	0.027 ± 0.0009
SN2005lu	0.0320 ± 0.000037	0.0317 ± 0.00050	0.048	CSP	53712.08 ± 0.23	0.834 ± 0.008	0.324 ± 0.011	0.022 ± 0.0009
SN2005na	0.0263 ± 0.000083	0.0272 ± 0.00050	0.056	CfA	53739.37 ± 0.30	1.027 ± 0.014	-0.050 ± 0.012	0.068 ± 0.0025
SN2006ac	0.0231 ± 0.000010	0.0237 ± 0.00050	0.065	CfA	53781.55 ± 0.10	1.189 ± 0.008	0.066 ± 0.010	0.014 ± 0.0006
SN2006ax	0.0167 ± 0.000020	0.0180 ± 0.00050	0.085	CSP	53827.78 ± 0.04	1.058 ± 0.012	-0.009 ± 0.005	0.041 ± 0.0019
SN2006bh	0.0108 ± 0.000013	0.0107 ± 0.00050	0.143	CSP	53834.14 ± 0.06	1.408 ± 0.007	-0.043 ± 0.004	0.023 ± 0.0004
SN2006bt	0.0321 ± 0.000007	0.0307 ± 0.00050	0.050	CSP	53859.29 ± 0.26	1.093 ± 0.042	0.313 ± 0.023	0.042 ± 0.0013
SN2006cp	0.0223 ± 0.000003	0.0223 ± 0.00050	0.069	CfA	53897.45 ± 0.15	1.023 ± 0.046	0.134 ± 0.022	0.022 ± 0.0011
SN2006D	0.0085 ± 0.000017	0.0090 ± 0.00050	0.171	CfA	53757.84 ± 0.08	1.460 ± 0.013	0.062 ± 0.009	0.039 ± 0.0004
SN2006ej	0.0204 ± 0.000007	0.0205 ± 0.00050	0.075	CSP	53977.24 ± 0.25	1.394 ± 0.013	0.016 ± 0.011	0.030 ± 0.0008
SN2006kf	0.0200 ± 0.000010	0.0194 ± 0.00050	0.079	CSP	54041.86 ± 0.05	1.517 ± 0.008	0.007 ± 0.006	0.210 ± 0.0020
SN2006lf	0.0132 ± 0.000017	0.0121 ± 0.00050	0.127	CfA	54045.56 ± 0.06	1.406 ± 0.010	-0.054 ± 0.010	0.814 ± 0.0503
SN2006N	0.0143 ± 0.000083	0.0145 ± 0.00050	0.106	CfA	53761.48 ± 0.15	1.457 ± 0.013	-0.030 ± 0.007	0.083 ± 0.0010
SN2007A	0.0176 ± 0.000087	0.0172 ± 0.00050	0.089	CSP	54113.67 ± 0.13	1.037 ± 0.034	0.225 ± 0.014	0.063 ± 0.0016
SN2007af	0.0055 ± 0.000013	0.0056 ± 0.00018	0.000	CSP	54174.97 ± 0.04	1.116 ± 0.010	0.183 ± 0.005	0.034 ± 0.0008
SN2007ai	0.0317 ± 0.000137	0.0327 ± 0.00050	0.047	CSP	54174.03 ± 0.26	0.844 ± 0.021	0.339 ± 0.013	0.286 ± 0.0035
SN2007as	0.0176 ± 0.000460	0.0184 ± 0.00050	0.084	CSP	54181.15 ± 0.23	1.120 ± 0.023	0.138 ± 0.010	0.123 ± 0.0007
SN2007bc	0.0208 ± 0.000007	0.0211 ± 0.00050	0.073	CSP	54200.82 ± 0.09	1.282 ± 0.012	0.039 ± 0.006	0.019 ± 0.0006
SN2007bd	0.0304 ± 0.000100	0.0311 ± 0.00050	0.049	CSP	54207.43 ± 0.06	1.270 ± 0.012	-0.018 ± 0.010	0.029 ± 0.0009
SN2007ca	0.0141 ± 0.000010	0.0145 ± 0.00050	0.106	CSP	54228.20 ± 0.14	1.037 ± 0.024	0.376 ± 0.012	0.057 ± 0.0016
SN2007co	0.0270 ± 0.000110	0.0274 ± 0.00050	0.056	CfA	54264.91 ± 0.23	1.040 ± 0.040	0.208 ± 0.017	0.096 ± 0.0037
SN2007cq	0.0260 ± 0.000080	0.0252 ± 0.00050	0.061	CfA	54280.90 ± 0.10	1.062 ± 0.021	0.051 ± 0.011	0.092 ± 0.0020
SN2007jg	0.0371 ± 0.000013	0.0380 ± 0.00050	0.040	CSP	54366.64 ± 0.25	1.088 ± 0.034	0.150 ± 0.017	0.090 ± 0.0020
SN2007le	0.0067 ± 0.000003	0.0065 ± 0.00050	0.237	CSP	54399.85 ± 0.07	1.027 ± 0.016	0.379 ± 0.008	0.029 ± 0.0003
SN2007qe	0.0240 ± 0.000050	0.0236 ± 0.00050	0.065	CfA	54429.59 ± 0.10	0.988 ± 0.023	0.069 ± 0.014	0.033 ± 0.0008
SN2007sr	0.0055 ± 0.000030	0.0044 ± 0.00025	0.000	CSP	54449.73 ± 0.19	1.084 ± 0.015	0.173 ± 0.009	0.040 ± 0.0010
SN2007st	0.0212 ± 0.000030	0.0211 ± 0.00050	0.073	CSP	54455.09 ± 0.32	1.486 ± 0.019	0.101 ± 0.018	0.014 ± 0.0004
SN2008af	0.0334 ± 0.000007	0.0340 ± 0.00050	0.045	CfA	54499.69 ± 0.43	1.178 ± 0.010	-0.028 ± 0.023	0.029 ± 0.0012
SN2008ar	0.0262 ± 0.000010	0.0290 ± 0.00050	0.053	CSP	54535.22 ± 0.07	1.032 ± 0.014	0.081 ± 0.008	0.031 ± 0.0011
SN2008bc	0.0151 ± 0.000120	0.0156 ± 0.00050	0.098	CSP	54550.41 ± 0.08	1.015 ± 0.019	0.003 ± 0.008	0.225 ± 0.0042
SN2008bf	0.0235 ± 0.000167	0.0254 ± 0.00050	0.061	CSP	54555.31 ± 0.06	0.967 ± 0.012	-0.013 ± 0.006	0.030 ± 0.0027
SN2008C	0.0166 ± 0.000013	0.0175 ± 0.00050	0.088	CSP	54466.60 ± 0.23	1.075 ± 0.019	0.239 ± 0.010	0.072 ± 0.0023
SN2008fl	0.0199 ± 0.000103	0.0199 ± 0.00050	0.077	CSP	54721.85 ± 0.13	1.328 ± 0.006	0.080 ± 0.005	0.157 ± 0.0058
SN2008fr	0.0390 ± 0.002001	0.0384 ± 0.00050	0.040	CSP	54733.93 ± 0.26	0.920 ± 0.014	-0.002 ± 0.011	0.040 ± 0.0012
SN2008fw	0.0085 ± 0.000017	0.0086 ± 0.00050	0.178	CSP	54732.29 ± 0.15	0.844 ± 0.009	0.112 ± 0.008	0.112 ± 0.0030
SN2008gb	0.0370 ± 0.000167	0.0381 ± 0.00050	0.040	CfA	54748.22 ± 0.34	1.183 ± 0.014	0.080 ± 0.018	0.171 ± 0.0035
SN2008gg	0.0320 ± 0.000023	0.0311 ± 0.00050	0.049	CSP	54750.93 ± 0.34	1.036 ± 0.028	0.155 ± 0.013	0.019 ± 0.0010
SN2008gl	0.0340 ± 0.000117	0.0332 ± 0.00050	0.046	CSP	54768.70 ± 0.09	1.319 ± 0.010	0.030 ± 0.006	0.024 ± 0.0008
SN2008gp	0.0330 ± 0.000070	0.0335 ± 0.00050	0.046	CSP	54779.62 ± 0.04	1.017 ± 0.008	-0.018 ± 0.004	0.104 ± 0.0051
SN2008hj	0.0379 ± 0.000130	0.0372 ± 0.00050	0.041	CSP	54802.26 ± 0.12	1.055 ± 0.027	0.038 ± 0.012	0.030 ± 0.0008
SN2008hm	0.0197 ± 0.000077	0.0210 ± 0.00050	0.073	CfA	54804.74 ± 0.21	0.993 ± 0.025	0.182 ± 0.014	0.380 ± 0.0085
SN2008hs	0.0174 ± 0.000070	0.0189 ± 0.00004	0.058	CfA	54812.94 ± 0.14	1.531 ± 0.015	0.122 ± 0.024	0.050 ± 0.0003
SN2008hv	0.0126 ± 0.000007	0.0140 ± 0.00050	0.110	CSP	54817.65 ± 0.04	1.328 ± 0.006	-0.065 ± 0.006	0.028 ± 0.0008
SN2008ia	0.0219 ± 0.000097	0.0225 ± 0.00050	0.068	CSP	54813.67 ± 0.09	1.340 ± 0.009	0.003 ± 0.007	0.195 ± 0.0050
SN2009aa	0.0273 ± 0.000047	0.0287 ± 0.00050	0.054	CSP	54878.81 ± 0.04	1.172 ± 0.008	0.020 ± 0.005	0.029 ± 0.0009
SN2009ab	0.0112 ± 0.000020	0.0103 ± 0.00050	0.149	CSP	54883.89 ± 0.08	1.288 ± 0.016	0.050 ± 0.010	0.184 ± 0.0028
SN2009ad	0.0284 ± 0.000003	0.0287 ± 0.00050	0.054	CSP	54886.91 ± 0.07	0.949 ± 0.013	0.020 ± 0.007	0.095 ± 0.0011
SN2009ag	0.0086 ± 0.000007	0.0102 ± 0.00050	0.151	CSP	54890.23 ± 0.16	1.088 ± 0.019	0.343 ± 0.009	0.218 ± 0.0012
SN2009al	0.0221 ± 0.000080	0.0234 ± 0.00050	0.066	CfA	54897.20 ± 0.18	1.079 ± 0.033	0.236 ± 0.020	0.021 ± 0.0004
SN2009an	0.0092 ± 0.000007	0.0107 ± 0.00050	0.144	CfA	54898.56 ± 0.09	1.327 ± 0.010	0.063 ± 0.010	0.016 ± 0.0003
SN2009bv	0.0366 ± 0.000017	0.0385 ± 0.00050	0.040	CfA	54927.07 ± 0.20	0.948 ± 0.033	-0.026 ± 0.019	0.008 ± 0.0008
SN2009cz	0.0212 ± 0.000010	0.0218 ± 0.00050	0.070	CSP	54943.50 ± 0.09	0.899 ± 0.014	0.102 ± 0.007	0.022 ± 0.0003
SN2009D	0.0250 ± 0.000033	0.0243 ± 0.00050	0.063	CSP	54841.65 ± 0.11	1.025 ± 0.024	0.054 ± 0.009	0.044 ± 0.0012
SN2009kk	0.0129 ± 0.000150	0.0122 ± 0.00050	0.126	CfA	55126.37 ± 0.20	1.189 ± 0.006	-0.055 ± 0.011	0.116 ± 0.0025
SN2009kq	0.0117 ± 0.000020	0.0126 ± 0.00050	0.122	CfA	55154.81 ± 0.17	0.992 ± 0.025	0.089 ± 0.010	0.035 ± 0.0005
SN2009Y	0.0093 ± 0.000027	0.0094 ± 0.00050	0.163	CSP	54877.10 ± 0.10	1.063 ± 0.023	0.169 ± 0.010	0.087 ± 0.0005
SN2010ai	0.0184 ± 0.000123	0.0239 ± 0.00018	0.048	CfA	55277.50 ± 0.08	1.421 ± 0.016	-0.075 ± 0.016	0.008 ± 0.0010
SN2010dw	0.0381 ± 0.000150	0.0392 ± 0.00050	0.039	CfA	55358.25 ± 0.35	0.844 ± 0.058	0.177 ± 0.028	0.080 ± 0.0009
SN2010iw	0.0215 ± 0.000007	0.0228 ± 0.00050	0.067	CfA	55497.14 ± 0.26	0.876 ± 0.019	0.084 ± 0.012	0.047 ± 0.0006
SN2010kg	0.0166 ± 0.000007	0.0171 ± 0.00050	0.090	CfA	55543.96 ± 0.10	1.194 ± 0.011	0.183 ± 0.014	0.131 ± 0.0022
SN2011ao	0.0107 ± 0.000003	0.0120 ± 0.00050	0.128	CfA	55639.61 ± 0.11	1.012 ± 0.018	0.035 ± 0.019	0.017 ± 0.0001
SN2011B	0.0047 ± 0.000003	0.0056 ± 0.00050	0.276	CfA	55583.38 ± 0.06	1.174 ± 0.005	0.112 ± 0.008	0.026 ± 0.0011
SN2011by	0.0028 ± 0.000003	0.0051 ± 0.00020	0.000	CfA	55690.95 ± 0.05	1.053 ± 0.008	0.067 ± 0.005	0.012 ± 0.0002
SN2011df	0.0145 ± 0.000020	0.0150 ± 0.00050	0.102	CfA	55716.40 ± 0.11	0.923 ± 0.015	0.072 ± 0.010	0.112 ± 0.0034
SNf20080514-002	0.0219 ± 0.000010	0.0216 ± 0.00050	0.071	CfA	54612.80 ± 0.00	1.360 ± 0.000	-0.143 ± 0.000	0.027 ± 0.0014

NOTE—
[a] Heliocentric redshift from NED or the literature using v_{helio} from Table 3.
[b] Redshift corrected to the CMB frame and using the C15 local flow model or redshift-independent distance information from Table 4.
[c] Uncertainty in the theoretical distance modulus because of the peculiar velocity, defined in Eq. (8).
[d] LC-data source. CfA: Wood-Vasey et al. 2008; Friedman et al. 2015, CSP: Krisciunas et al. 2017, Others: K04c: Krisciunas et al. 2004c; V03: Valentini et al. 2003; K03: Krisciunas et al. 2003; P08: Pignata et al. 2008; St07: Stanishev et al. 2007; L09: Leloudas et al. 2009; K07: Krisciunas et al. 2007. Also see Table 3 of Friedman et al. 2015 for references.
[e] Determined by fitting the optical and NIR LCs data with SNooPy.
[f] LC shape parameter: apparent-magnitude decline between B-band peak luminosity and 15 days after peak.
[g] Host-galaxy color excess, as measured by SNooPy fits to the optical and NIR LCs.
[h] Milky-Way color excess, from the Schlafly & Finkbeiner (2011) Milky Way dust maps.

Table 3. SN Ia Recession Velocities

SN name[a]	RA (deg) $\alpha(2000)^b$	DEC (deg) $\delta(2000)^b$	Host Galaxy (or cluster)[c]	$v_{\rm helio}$ (km s^{-1})[d]	$v_{\rm CMB}$ (km s^{-1})[e]	$v_{\rm CMB,flow}$ (km s^{-1})[f]	Ref(s).[g]	Code[h]
SN1998bu	161.69167	11.83528	NGC 3368	888 ± 1	757 ± 70	242 ± 150	NED;F01	Cepheid
SN1999ee	334.04167	-36.84444	IC 5179	3419 ± 3	3160 ± 3	3368 ± 150	NED;C15	Flow
SN1999ek	84.13167	16.63833	UGC 03329	5266 ± 2	5292 ± 2	5340 ± 150	NED;C15	Flow
SN2000E	309.30750	66.09722	NGC 6951	1424 ± 1	1267 ± 1	1685 ± 150	NED;C15	Flow
SN2000bh	185.31292	-21.99889	ESO 573-G 014	6854 ± 8	7196 ± 8	7188 ± 150	NED;C15	Flow
SN2000ca	203.84583	-34.16028	ESO 383-G 032	7080 ± 60	7351 ± 62	7167 ± 150	NED;C15	Flow
SN2001ba	174.50750	-32.33083	MCG -05-28-001	8861 ± 10	9193 ± 10	9060 ± 150	NED;C15	Flow
SN2001bt	288.44500	-59.28972	IC 4830	4388 ± 10	4331 ± 10	4260 ± 150	NED;C15	Flow
SN2001cn	281.57417	-65.76167	IC 4758	4543 ± 38	4523 ± 38	4626 ± 150	NED;C15	Flow
SN2001cz	191.87583	-39.58000	NGC 4679	4643 ± 8	4930 ± 8	5124 ± 150	NED;C15	Flow
SN2001el	56.12750	-44.63972	NGC 1448	1168 ± 2	1340 ± 42	1568 ± 150	NED;R16	Cepheid
SN2002dj	198.25125	-19.51917	NGC 5018	2816 ± 1	2479 ± 457	2023 ± 150	NED;Co12	SBF/TF
SN2003du	218.64917	59.33444	UGC 9391	1914 ± 4	2809 ± 105	3165 ± 150	NED;R16	Cepheid
SN2003hv	46.03875	-26.08556	NGC 1201	1686 ± 11	1470 ± 101	1723 ± 150	NED;Tu13	SBF/TF
SN2004S	101.43125	-31.23111	MCG -05-16-021	2788 ± 1	2937 ± 1	3213 ± 150	NED;C15	Flow
SN2004ef	340.54175	19.99456	UGC 12158	9289 ± 5	8931 ± 5	9015 ± 150	NED;C15	Flow
SN2004eo	308.22579	9.92853	NGC 6928	4684 ± 1	4398 ± 1	4560 ± 150	NED;C15	Flow
SN2004ey	327.28254	0.44422	UGC 11816	4749 ± 1	4405 ± 1	4617 ± 150	NED;C15	Flow
SN2004gs	129.59658	17.62772	MCG +03-22-020	8214 ± 2	8475 ± 2	8590 ± 150	NED;C15	Flow
SN2005bo	192.42096	-11.09647	NGC 4708	4166 ± 8	4503 ± 9	4314 ± 150	NED;C15	Flow
SN2005cf	230.38417	-7.41306	MCG -01-39-003	1929 ± 5	2077 ± 109	2034 ± 150	NED;R16	Cepheid
SN2005el	77.95300	5.19428	NGC 1819	4470 ± 5	4466 ± 5	4574 ± 150	NED;C15	Flow
SN2005iq	359.63542	-18.70917	ESO 538- G 013	10206 ± 37	9880 ± 36	10058 ± 150	NED;C15	Flow
SN2005kc	338.53058	5.56842	NGC 7311	4524 ± 1	4159 ± 1	4343 ± 150	NED;C15	Flow
SN2005ki	160.11758	9.20233	NGC 3332	5833 ± 3	6185 ± 3	6080 ± 150	NED;C15	Flow
SN2005lu	39.01546	-17.26389	ESO 545-G038	9596 ± 11	9389 ± 11	9515 ± 150	NED;C15	Flow
SN2005na	105.40258	14.13325	UGC 3634	7891 ± 25	8045 ± 25	8162 ± 150	NED;C15	Flow
SN2006D	193.14142	-9.77522	MCG -01-33-034	2556 ± 5	2891 ± 6	2691 ± 150	NED;C15	Flow
SN2006N	92.13000	64.72361	CGCG 308-009	4280 ± 25	4278 ± 25	4354 ± 150	NED;C15	Flow
SN2006ac	190.43708	35.08528	NGC 4619	6923 ± 3	7175 ± 3	7113 ± 150	NED;C15	Flow
SN2006ax	171.01442	-12.29144	NGC 3663	5014 ± 6	5382 ± 6	5386 ± 150	NED;C15	Flow
SN2006bh	340.06708	-66.48508	NGC 7329	3252 ± 4	3148 ± 4	3222 ± 150	NED;C15	Flow
SN2006bt	239.12721	20.04592	CGCG 108-013	9618 ± 2	9714 ± 2	9211 ± 150	NED;K17	Flow
SN2006cp	184.81208	22.42722	UGC 7357	6682 ± 1	6990 ± 1	6673 ± 150	NED;C15	Flow
SN2006ej	9.74904	-9.01572	NGC 191A	6110 ± 2	5780 ± 2	6152 ± 150	NED;C15	Flow
SN2006kf	55.46033	8.15694	UGC 2829	6007 ± 3	5862 ± 3	5821 ± 150	NED;C15	Flow
SN2006lf	69.62292	44.03361	UGC 3108	3954 ± 5	3885 ± 5	3627 ± 150	NED;C15	Flow
SN2007A	6.31942	12.88681	NGC 105	5290 ± 26	4940 ± 24	5162 ± 150	NED;C15	Flow
SN2007af	215.58763	-0.39378	NGC 5584	1638 ± 4	1667 ± 53	1418 ± 150	NED;R16	Cepheid
SN2007ai	243.22392	-21.63019	MCG-04-38-004	9492 ± 41	9595 ± 41	9815 ± 150	NED;C15	Flow
SN2007as	141.90004	-80.17756	ESO 018-G 018	5268 ± 138	5368 ± 141	5503 ± 150	NED;C15	Flow
SN2007bc	169.81071	20.80903	UGC 6332	6221 ± 2	6548 ± 2	6333 ± 150	NED;C15	Flow
SN2007bd	127.88867	-1.19944	UGC 4455	9126 ± 30	9408 ± 31	9318 ± 150	NED;C15	Flow
SN2007ca	202.77421	-15.10183	MCG -02-34-061	4217 ± 3	4520 ± 3	4339 ± 150	NED;C15	Flow
SN2007co	275.76500	29.89722	MCG +05-43-016	8083 ± 33	7963 ± 33	8229 ± 150	NED;C15	Flow
SN2007cq	333.66833	5.08028	2MASX J22144070+0504435	7807 ± 24	7448 ± 23	7564 ± 150	Ch13;C15	Flow
SN2007jg	52.46175	0.05683	SDSS J032950.83+000316.0	11113 ± 4	10955 ± 4	11379 ± 150	NED;C15	Flow
SN2007le	354.70171	-6.52258	NGC 7721	2017 ± 1	1660 ± 1	1939 ± 150	NED;C15	Flow
SN2007qe	358.55417	27.40917	NSF J235412.09+272432.3	7183 ± 15	6842 ± 14	7067 ± 150	Ch13;C15	Flow
SN2007sr	180.47000	-18.97269	NGC 4038	1641 ± 9	1327 ± 75	611 ± 150	NED;R16	Cepheid
SN2007st	27.17696	-48.64939	NGC 692	6350 ± 9	6195 ± 9	6330 ± 150	NED;C15	Flow
SN2008C	104.29804	20.43714	UGC 3611	4983 ± 4	5121 ± 4	5260 ± 150	NED;C15	Flow
SN2008af	224.86875	16.65333	UGC 9640	10020 ± 2	10199 ± 2	10195 ± 150	NED;C15	Flow
SN2008ar	186.15800	10.83817	IC 3284	7846 ± 3	8180 ± 3	8680 ± 150	NED;C15	Flow
SN2008bc	144.63012	-63.97378	KK 1524	4523 ± 36	4711 ± 37	4677 ± 150	NED;C15	Flow
SN2008bf	181.01208	20.24517	ambiguous	7045 ± 50	7365 ± 52	7608 ± 150	K17;C15	Flow
SN2008fl	294.18683	-37.55125	NGC 6805	5960 ± 31	5815 ± 30	5980 ± 150	NED;C15	Flow
SN2008fr	17.95475	14.64083	SDSS J011149.19+143826.5	11692 ± 600	11373 ± 584	11503 ± 150	NED;C15	Flow
SN2008fw	157.23321	-44.66544	NGC 3261	2563 ± 5	2851 ± 6	2587 ± 150	NED;C15	Flow
SN2008gb	44.48792	46.86583	UGC 2427	11092 ± 50	10921 ± 49	11428 ± 150	NED;C15	Flow
SN2008gg	21.34600	-18.17244	NGC 539	9598 ± 7	9321 ± 7	9330 ± 150	NED;C15	Flow
SN2008gl	20.22842	4.80531	UGC 881	10198 ± 35	9885 ± 34	9954 ± 150	NED;C15	Flow
SN2008gp	50.75304	1.36189	MCG +00-9-74	9901 ± 21	9732 ± 21	10030 ± 150	NED;C15	Flow
SN2008hj	1.00796	-11.16875	MCG -02-01-014	11360 ± 39	11018 ± 38	11140 ± 150	NED;C15	Flow
SN2008hm	51.79542	46.94444	2MFGC 02845	5895 ± 23	5752 ± 22	6282 ± 150	NED;C15	Flow
SN2008hs	36.37333	41.84306	NGC 0910 (Abell 347)	5207 ± 21	5655 ± 13	6186 ± 150	NED;Dh18	Cluster
SN2008hv	136.89192	3.39225	NGC 2765	3775 ± 2	4087 ± 2	4185 ± 150	NED;C15	Flow
SN2008ia	132.64646	-61.27794	ESO 125-G 006	6578 ± 29	6761 ± 30	6754 ± 150	NED;C15	Flow
SN2009D	58.59512	-19.18172	MCG -03-10-052	7497 ± 10	7397 ± 10	7275 ± 150	NED;C15	Flow
SN2009Y	220.59938	-17.24678	NGC 5728	2793 ± 8	3019 ± 9	2827 ± 150	NED;C15	Flow
SN2009aa	170.92617	-22.27069	ESO 570-G20	8187 ± 14	8543 ± 15	8597 ± 150	NED;C15	Flow
SN2009ab	64.15162	2.76417	UGC 2998	3349 ± 6	3260 ± 6	3090 ± 150	NED;C15	Flow
SN2009ad	75.88908	6.65992	UGC 3236	8514 ± 1	8496 ± 1	8602 ± 150	NED;C15	Flow
SN2009ag	107.92004	-26.68508	ESO 492-2	2590 ± 2	2774 ± 2	3056 ± 150	NED;C15	Flow
SN2009al	162.84196	8.57853	NGC 3425	6627 ± 24	6982 ± 25	7007 ± 150	NED;C15	Flow
SN2009an	185.69750	65.85111	NGC 4332	2764 ± 2	2867 ± 2	3207 ± 150	NED;C15	Flow
SN2009bv	196.83542	35.78444	MCG +06-29-039	10966 ± 5	11201 ± 5	11539 ± 150	NED;C15	Flow
SN2009cz	138.75008	29.73531	NGC 2789	6344 ± 3	6601 ± 3	6548 ± 150	NED;C15	Flow
SN2009kk	57.43458	-3.26444	2MFGC 03182	3855 ± 45	3729 ± 44	3653 ± 150	NED;C15	Flow
SN2009kq	129.06292	28.06722	MCG +05-21-001	3507 ± 6	3739 ± 6	3766 ± 150	NED;C15	Flow
SN2010ai	194.85000	27.99639	SDSS J125925.04+275948.2 (Coma)	5507 ± 37	7166 ± 54	7298 ± 150	NED;P14	Cluster
SN2010dw	230.66792	-5.92111	2MASX J15224062-0555214	11428 ± 45	11600 ± 46	11759 ± 150	NED;C15	Flow
SN2010iw	131.31250	27.82278	UGC 4570	6458 ± 2	6698 ± 2	6833 ± 150	NED;C15	Flow
SN2010kg	70.03500	7.35000	NGC 1633	4986 ± 2	4931 ± 2	5128 ± 150	NED;C15	Flow
SN2011B	133.95208	78.21750	NGC 2655	1400 ± 1	1419 ± 1	1670 ± 150	NED;C15	Flow
SN2011ao	178.46250	33.36278	IC 2973	3210 ± 1	3487 ± 1	3592 ± 150	NED;C15	Flow
SN2011by	178.94000	55.32611	NGC 3972	852 ± 1	1521 ± 61	1796 ± 150	NED;R16	Cepheid
SN2011df	291.89000	54.38639	NGC 6801	4361 ± 6	4205 ± 6	4500 ± 150	NED;C15	Flow
SNf20080514-002	202.30625	11.26889	UGC 8472	6577 ± 3	6866 ± 3	6480 ± 150	NED;C15	Flow

NOTE—
[a] SN Ia name. All SN Ia in this work are spectroscopically normal (see §2.1).
[b] Epoch J2000 equatorial coordinates in decimal degrees.
[c] Host galaxy or cluster from NASA/IPAC Extragalactic Database (NED) or the literature. See Ref(s) column.
[d] Heliocentric recession velocity from NED with smallest reported uncertainty (SDSS DR13 values are used even if earlier SDSS reported smaller uncertainties). When no uncertainty is reported we assume an error of 50 km/s.
[e] CMB frame recession velocity $v_{\rm CMB}$ using $v_{\rm helio}$, RA, DEC, and CMB dipole from (Planck Collaboration et al. 2016a).
[f] $v_{\rm CMB,flow}$ takes $v_{\rm CMB}$, RA, DEC as input and further corrects to the CMB frame via the local velocity flow model of Carrick et al. (2015) (hereafter C15), with assumed uncertainty of 150 km/s (see §2.2).
[g] The first reference listed is for $v_{\rm helio}$ from NED or the literature. The second reference is for the effective $v_{\rm CMB}$ derived using either the C15 local flow model or independent distance information for nearby galaxies with $v_{\rm helio} \lesssim 3000$ km/s, special cases where host galaxy identification from NED is ambiguous, or some clusters which may have $v > 3000$km/s (see §2.2 and Table 4). Reference codes: C15: Carrick et al. 2015; Ch11: Childress et al. 2011; Ch13: Childress et al. 2013; Co12: Courtois & Tully 2012; Dh18: Dhawan et al. 2018; F01: Freedman et al. 2001; F15: Friedman et al. 2015; H12: Hicken et al. 2012; K17: Krisciunas et al. 2017; MO00: Mould et al. 2000; P14: Pimbblet et al. 2014; Pr07: Prieto et al. 2007; R14: Rest et al. 2014; R16: Riess et al. 2016; Tu13: Tully et al. 2013; Tu16: Tully et al. 2016.
[h] If Code=Flow, we use $v_{\rm CMB,flow}$ from C15 in our Hubble diagram. If Code ≠ Flow, we use $v_{\rm CMB}$. Other codes include Cepheid: HST Cepheid distances from SHOES Riess et al. 2016 or HST Key Project Freedman et al. 2001; Cluster: Mean redshift of galaxy cluster from NED (e.g. Virgo, Coma, Abell*); SBF/TF: Surface Brightness Fluctuations (SBF) or Tully-Fisher relation (TF) (e.g. Courtois & Tully 2012; Tully et al. 2013, 2016).

Table 4. SN Ia With Redshift-Independent Distance Moduli

SN name	Host Galaxy (or cluster)	μ' (mag)[a]	H_0' ($\mathrm{km\,s^{-1}\,Mpc^{-1}}$)	μ_{eff} (mag)[b]	Ref.[c]	Code[d]
SN1998bu	NGC 3368	30.110 ± 0.200	72.00 ± 8.00	30.073 ± 0.200	F01	Cepheid
SN2001el	NGC 1448	31.311 ± 0.045	73.24 ± 1.74	31.311 ± 0.045	R16	Cepheid
SN2002dj	NGC 5018	32.570 ± 0.400	75.90 ± 3.80	32.647 ± 0.400	Co12	SBF/TF
SN2003du	UGC 9391	32.919 ± 0.063	73.24 ± 1.74	32.919 ± 0.063	R16	Cepheid
SN2003hv	NGC 1201	31.120 ± 0.250	74.40 ± 3.00	31.154 ± 0.250	Tu13	SBF/TF
SN2005cf	MCG -01-39-003	32.263 ± 0.102	73.24 ± 1.74	32.263 ± 0.102	R16	Cepheid
SN2007af	NGC 5584	31.786 ± 0.046	73.24 ± 1.74	31.786 ± 0.046	R16	Cepheid
SN2007sr	NGC 4038	31.290 ± 0.112	73.24 ± 1.74	31.290 ± 0.112	R16	Cepheid
SN2011by	NGC 3972	31.587 ± 0.070	73.24 ± 1.74	31.587 ± 0.070	R16	Cepheid

NOTE—
[a] Reported distance modulus μ' on Hubble scale H_0'.
[b] This is converted to a distance modulus μ_{eff} on the Hubble scale of $H_0 = 73.24\ \mathrm{km\,s^{-1}\,Mpc^{-1}}$ via Eq. (1). For SN Ia with Cepheid distances from Riess et al. 2016, since $H_0' = H_0$ and $\mu' = \mu_{\mathrm{eff}}$, effective distance moduli μ_{eff} are already on the Hubble scale used for this paper. We compute the effective CMB frame recession velocity v_{eff} in Table 3 via Eqs. 2-3 using μ' and H_0' (or equivalently μ_{eff} and H_0). This is then used to construct an effective redshift or recession velocity for use in Hubble diagrams.
[c] Reference codes: Co12: Courtois & Tully 2012; F01: Freedman et al. 2001; R16: Riess et al. 2016; Tu13: Tully et al. 2013; Tu16: Tully et al. 2016
[d] Same as in Table 3.

the NASA/IPAC Extragalactic Database (NED), using measurements with the smallest reported uncertainty.[1] If the host galaxy was anonymous or had no reported NED redshift, we used redshifts reported in the literature. When no uncertainties are available, we assume a recession velocity uncertainty of 50 km/s.

To further correct the CMB frame redshifts for local velocity flows and to estimate uncertainties, we used the model of Carrick et al. 2015.[2] Such corrections are most important for SN Ia with $z < 0.01$ ($v < 3000$ km/s), but we also use them for SN Ia further into the Hubble flow.

In special cases, we did not use the Carrick et al. 2015 flow model and instead used independent information for individual objects. For several SN Ia that have $v_{\rm helio} > 3000$ km/s, but are members of known galaxy clusters, to avoid large peculiar velocities from the cluster velocity dispersion, following Dhawan et al. 2018, we used the mean recession velocity of the cluster based on the cluster redshift from NED to estimate the CMB frame recession velocity for the SN Ia host galaxy. For SN 2008hs in Abell 347, we used $v_{\rm CMB} = 5655 \pm 13$ km/s. For SN 2010ai in the Coma cluster, we used $v_{\rm CMB} = 7166 \pm 54$ km/s (Pimbblet et al. 2014).

To further avoid peculiar velocity systematics for SN Ia with $v_{\rm helio} < 3000$ km/s, where available, we also used redshift-independent distance information from Cepheid variable stars, surface brightness fluctuations (SBF), or the Tully-Fisher method (TF) to estimate an effective CMB frame redshift (see Tables 3-4 for references).

Of the 19 SN Ia with Cepheid distances $\mu_{\rm Ceph}$ and uncertainties $\sigma_{\mu_{\rm Ceph}}$ in the HST SHOES program (Table 5 of Riess et al. 2016), 7 with NIR data are included in our Table 3 (SN 2001el, SN 2003du, SN 2005cf, SN 2007af, SN 2007sr, and SN 2011by). One other SN Ia (SN 1998bu) also has Cepheid distance from the HST Key Project (Table 4 of Freedman et al. 2001).[3] Lastly, 2 more SN Ia with NIR data (SN 2002dj, SN 2003hv) had redshift-independent host galaxy distance information from TF and/or SBF (Courtois & Tully 2012; Tully et al. 2013, 2016).

[1] However, even if earlier SDSS data releases report a smaller redshift error, we use the SDSS DR13 (2016) reported heliocentric redshift from NED where available (Albareti et al. 2017; http://www.sdss.org/dr13/data_access/bulk/).

[2] http://cosmicflows.iap.fr/table_query.html. We used defaults of $\Omega_M = 0.3$ (implicitly $\Omega_\Lambda = 0.7$ for a flat universe), $H_0 = 73.24$ km s^{-1}Mpc^{-1} (Riess et al. 2016), $\beta = 0.43$, and bulk flows of $(V_x, V_y, V_z) = (89, -131, 17)$ km/s (Carrick et al. 2015).

[3] We use the metallicity corrected values μ_Z and σ_Z from Table 4 of Freedman et al. 2001.

For all of these methods, we convert the reported distance modulus μ' on a given Hubble scale H_0' to the Hubble scale of $H_0 = 73.24$ km s^{-1}Mpc^{-1} as measured by Riess et al. 2016 and use this value of H_0 throughout the rest of the paper. More specifically, for Hubble constants in units of km s^{-1}Mpc^{-1}, the distance modulus $\mu_{\rm eff}$ on our fiducial Hubble scale H_0 is given by

$$\mu_{\rm eff} = 5 \log_{10}\left(\frac{H_0'}{H_0}\right) + \mu' \tag{1}$$

See Table 4.

For these objects, we convert the redshift independent distance modulus $\mu_{\rm eff}$ to an effective CMB frame recession velocity with Hubble's law in the linear regime:

$$v_{\rm eff} = c\ z_{\rm eff} = H_0\ d_L(\mu_{\rm eff}) = H_0 \times 1{\rm Mpc} \times 10^{\frac{\mu_{\rm eff}-25}{5}} \tag{2}$$

with an uncertainty given by[4]

$$\sigma_{v_{\rm eff}} = c\ \sigma_{z_{\rm eff}} = c\ z_{\rm eff}\left(\frac{\ln 10}{5}\sigma_{\mu_{\rm eff}}\right) \tag{3}$$

For SN Ia with Cepheid distances, we assume that the only contribution to the recession velocity uncertainty comes from Eq. 3 and therefore adopt a peculiar velocity uncertainty of 0 km/s for these objects.

For objects without Cepheid or other redshift-independent distances, we assume a peculiar velocity uncertainty of $\sigma_{\rm pec} = 150$ km/s, following Radburn-Smith et al. 2004.[5] As shown in Section 5, the value of $\sigma_{\rm pec} = 150$ km/s yields a more conservative determination of the Hubble diagram intrinsic scatter compared with larger values of $\sigma_{\rm pec}$ that tend to produce a misleadingly small value. However, statistics like the RMS, which we also use to compare various methods, are relatively insensitive to the assumed value of $\sigma_{\rm pec}$.

3. NIR LC TEMPLATES

We determine the normalized mean $YJHK_s$ LC templates, as shown in Figure 1 and Table 5, using the SN Ia in Table 2 as follows. In each band, we convert the photometry from the observer-frame apparent magnitude to the rest-frame absolute magnitude. We further apply K-corrections to the rest-frame and correct for Milky Way dust extinction. These steps are detailed in §3.1. We then use a *Gaussian process* method, as described in §3.2, to fit the LC in each NIR band. Finally, in §3.3,

[4] We do not propagate the uncertainty on H_0 in Eq. 2 because we have fixed the Hubble scale for this work.

[5] Estimates in the literature range from $\sigma_{\rm pec} = 150-400$ km/s: $\sigma_{\rm pec} = 150$ km/s (Radburn-Smith et al. 2004), 300 km/s (Davis et al. 2011), $\sigma_{\rm pec} = 360$ km/s (Kessler et al. 2009), or $\sigma_{\rm pec} = 400$ km/s (Wood-Vasey et al. 2007).

Table 5. Normalized $YJHK_s$ LC Templates

t^* (days)	$\theta^{(Y)}$ (mag)	$\sigma_\theta^{(Y)}$ (mag)	$\theta^{(J)}$ (mag)	$\sigma_\theta^{(J)}$ (mag)	$\theta^{(H)}$ (mag)	$\sigma_\theta^{(H)}$ (mag)	$\theta^{(K)}$ (mag)	$\sigma_\theta^{(K)}$ (mag)
-10	0.303 ± 0.067	0.168	0.428 ± 0.037	0.136	0.367 ± 0.047	0.184	0.439 ± 0.290	0.178
-9	0.152 ± 0.034	0.108	0.261 ± 0.025	0.106	0.213 ± 0.032	0.136	0.289 ± 0.335	0.194
-8	-0.007 ± 0.026	0.092	0.092 ± 0.020	0.094	0.075 ± 0.023	0.104	0.150 ± 0.125	0.112
-7	-0.135 ± 0.023	0.092	-0.038 ± 0.015	0.076	-0.010 ± 0.016	0.070	0.001 ± 0.058	0.106
-6	-0.204 ± 0.018	0.078	-0.115 ± 0.013	0.070	-0.065 ± 0.012	0.054	-0.058 ± 0.034	0.066
-5	-0.228 ± 0.016	0.072	-0.153 ± 0.012	0.070	-0.093 ± 0.010	0.046	-0.088 ± 0.021	0.034
-4	-0.224 ± 0.012	0.056	-0.159 ± 0.010	0.060	-0.102 ± 0.007	0.034	-0.103 ± 0.016	0.020
-3	-0.200 ± 0.008	0.042	-0.148 ± 0.008	0.050	-0.092 ± 0.006	0.032	-0.096 ± 0.011	0.014
-2	-0.151 ± 0.005	0.028	-0.116 ± 0.005	0.038	-0.069 ± 0.004	0.024	-0.073 ± 0.008	0.010
-1	-0.082 ± 0.003	0.014	-0.065 ± 0.003	0.022	-0.037 ± 0.002	0.014	-0.040 ± 0.004	0.006
0	0.000 ± 0.000	0.000	0.000 ± 0.000	0.000	0.000 ± 0.000	0.000	0.000 ± 0.000	0.000
1	0.090 ± 0.002	0.012	0.075 ± 0.003	0.024	0.039 ± 0.002	0.016	0.041 ± 0.005	0.014
2	0.184 ± 0.005	0.024	0.162 ± 0.007	0.050	0.079 ± 0.005	0.032	0.083 ± 0.011	0.030
3	0.276 ± 0.007	0.036	0.259 ± 0.010	0.080	0.115 ± 0.007	0.048	0.125 ± 0.017	0.046
4	0.363 ± 0.009	0.050	0.369 ± 0.014	0.108	0.147 ± 0.009	0.064	0.163 ± 0.022	0.062
5	0.441 ± 0.011	0.060	0.492 ± 0.018	0.140	0.173 ± 0.012	0.078	0.200 ± 0.026	0.074
6	0.510 ± 0.013	0.072	0.628 ± 0.022	0.168	0.194 ± 0.013	0.092	0.233 ± 0.030	0.086
7	0.568 ± 0.015	0.080	0.774 ± 0.025	0.188	0.207 ± 0.015	0.104	0.262 ± 0.034	0.096
8	0.612 ± 0.016	0.086	0.921 ± 0.026	0.202	0.214 ± 0.017	0.114	0.284 ± 0.037	0.100
9	0.650 ± 0.016	0.088	1.066 ± 0.028	0.210	0.214 ± 0.018	0.122	0.298 ± 0.037	0.100
10	0.670 ± 0.017	0.092	1.199 ± 0.027	0.208	0.208 ± 0.018	0.128	0.306 ± 0.038	0.094
11	0.676 ± 0.017	0.096	1.316 ± 0.027	0.200	0.198 ± 0.019	0.134	0.309 ± 0.035	0.086
12	0.666 ± 0.019	0.104	1.419 ± 0.026	0.186	0.179 ± 0.020	0.138	0.309 ± 0.035	0.080
13	0.640 ± 0.020	0.108	1.487 ± 0.024	0.170	0.156 ± 0.020	0.138	0.305 ± 0.034	0.078
14	0.600 ± 0.022	0.116	1.525 ± 0.024	0.166	0.127 ± 0.021	0.138	0.295 ± 0.033	0.074
15	0.540 ± 0.023	0.118	1.529 ± 0.024	0.170	0.089 ± 0.019	0.134	0.278 ± 0.032	0.068
16	0.477 ± 0.024	0.126	1.513 ± 0.026	0.182	0.053 ± 0.019	0.128	0.257 ± 0.028	0.058
17	0.409 ± 0.025	0.132	1.478 ± 0.028	0.195	0.017 ± 0.019	0.122	0.234 ± 0.027	0.056
18	0.336 ± 0.026	0.138	1.429 ± 0.029	0.208	-0.018 ± 0.018	0.116	0.211 ± 0.028	0.064
19	0.261 ± 0.026	0.142	1.373 ± 0.030	0.216	-0.049 ± 0.017	0.108	0.188 ± 0.030	0.074
20	0.183 ± 0.027	0.144	1.312 ± 0.032	0.226	-0.079 ± 0.016	0.100	0.169 ± 0.031	0.082
21	0.114 ± 0.029	0.150	1.263 ± 0.033	0.232	-0.091 ± 0.014	0.080	0.149 ± 0.033	0.088
22	0.054 ± 0.028	0.148	1.221 ± 0.034	0.236	-0.102 ± 0.014	0.076	0.138 ± 0.034	0.094
23	-0.007 ± 0.027	0.142	1.183 ± 0.032	0.228	-0.108 ± 0.014	0.082	0.130 ± 0.036	0.100
24	-0.056 ± 0.026	0.134	1.151 ± 0.032	0.218	-0.102 ± 0.016	0.094	0.126 ± 0.039	0.110
25	-0.095 ± 0.025	0.126	1.124 ± 0.029	0.198	-0.092 ± 0.019	0.120	0.132 ± 0.043	0.122
26	-0.123 ± 0.024	0.120	1.106 ± 0.026	0.180	-0.075 ± 0.023	0.152	0.147 ± 0.047	0.134
27	-0.144 ± 0.024	0.124	1.091 ± 0.025	0.170	-0.050 ± 0.027	0.182	0.172 ± 0.054	0.156
28	-0.147 ± 0.026	0.134	1.085 ± 0.024	0.154	-0.018 ± 0.031	0.214	0.205 ± 0.060	0.174
29	-0.151 ± 0.031	0.162	1.081 ± 0.028	0.178	0.021 ± 0.036	0.244	0.248 ± 0.068	0.200
30	-0.149 ± 0.038	0.196	1.082 ± 0.034	0.224	0.067 ± 0.041	0.272	0.302 ± 0.084	0.238
31	-0.137 ± 0.046	0.238	1.090 ± 0.040	0.274	0.124 ± 0.043	0.294	0.356 ± 0.095	0.262
32	-0.115 ± 0.053	0.274	1.112 ± 0.048	0.322	0.183 ± 0.046	0.312	0.414 ± 0.111	0.306
33	-0.083 ± 0.058	0.304	1.134 ± 0.054	0.354	0.248 ± 0.049	0.316	0.484 ± 0.118	0.322
34	-0.038 ± 0.065	0.332	1.186 ± 0.059	0.382	0.324 ± 0.052	0.326	0.566 ± 0.133	0.342
35	0.007 ± 0.070	0.340	1.232 ± 0.063	0.396	0.375 ± 0.052	0.320	0.636 ± 0.138	0.350
36	0.054 ± 0.075	0.356	1.305 ± 0.065	0.408	0.438 ± 0.053	0.320	0.699 ± 0.144	0.358
37	0.105 ± 0.078	0.364	1.378 ± 0.065	0.396	0.472 ± 0.050	0.298	0.762 ± 0.146	0.362
38	0.156 ± 0.077	0.370	1.464 ± 0.068	0.408	0.545 ± 0.050	0.294	0.816 ± 0.148	0.372
39	0.208 ± 0.077	0.372	1.555 ± 0.069	0.408	0.605 ± 0.050	0.294	0.868 ± 0.141	0.368
40	0.256 ± 0.082	0.384	1.647 ± 0.068	0.402	0.672 ± 0.050	0.292	0.912 ± 0.148	0.370
41	0.325 ± 0.084	0.388	1.736 ± 0.069	0.406	0.703 ± 0.049	0.274	0.955 ± 0.142	0.356
42	0.390 ± 0.086	0.396	1.820 ± 0.071	0.418	0.759 ± 0.050	0.282	0.947 ± 0.140	0.334
43	0.469 ± 0.090	0.404	1.922 ± 0.076	0.436	0.818 ± 0.053	0.294	0.981 ± 0.133	0.332
44	0.507 ± 0.094	0.404	1.992 ± 0.077	0.440	0.852 ± 0.055	0.302	0.987 ± 0.149	0.335
45	0.557 ± 0.091	0.400	2.055 ± 0.081	0.454	0.908 ± 0.060	0.312	1.028 ± 0.149	0.338

Note— Mean NIR LC templates in the $YJHK_s$-bands using the hierarchical Bayesian model and Gaussian process method described in §3. These are referenced to the time of B-band maximum light, such that $t^* = 0$ at $t_{B\max}$. See Fig. 1.

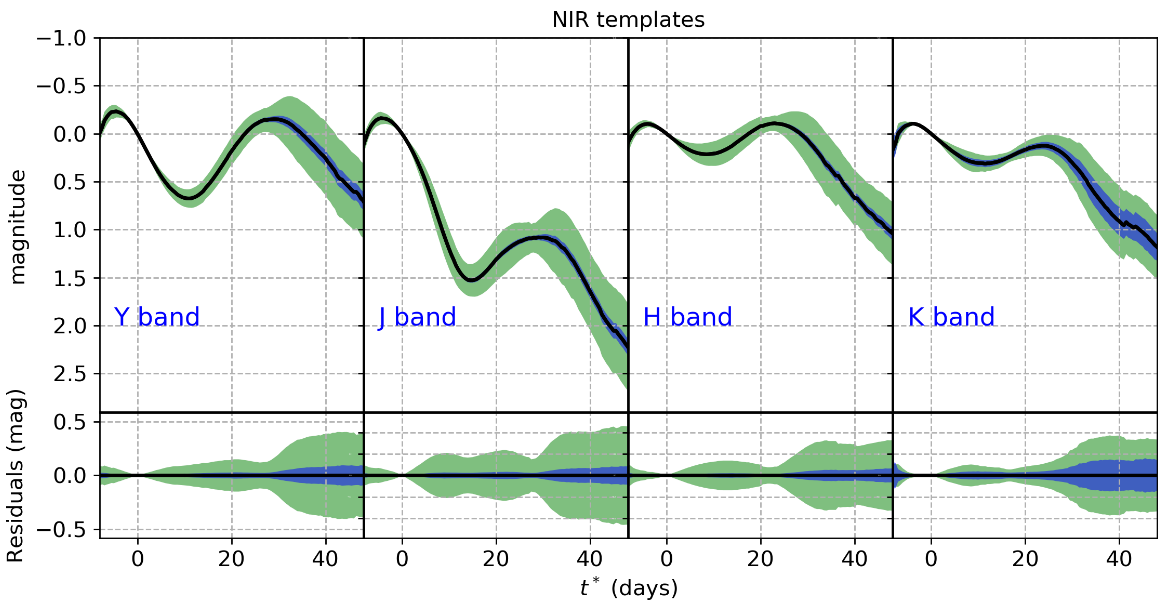

Figure 1. Upper and lower panels show the normalized mean $YJHK_s$ templates and residual plots, respectively. By construction, we normalize the templates so that they have magnitude zero at $t^* = 0$, with reference to the time of B-band maximum light. The numerical values of these templates are tabulated with 1-day sampling in Table 5. The black curves show the normalized mean magnitude $\theta(t^*)$ vs. rest-frame phase t^*, while the green and blue bands correspond to the population standard deviation, $\sigma_\theta(t^*)$, and the uncertainty in θ, respectively, determined using the hierarchical Bayesian model and Gaussian process method described in §3. We use 28, 67, 68 and 25 SN Ia that we can determine $\boldsymbol{\mu}^{\mathrm{L}}$ as described in §3.2 to build the Y, J, H and K_s templates respectively.

using a hierarchical Bayesian model we average all the LCs in a given NIR band to determine the normalized mean LC template, its uncertainty, and the population standard deviation.

3.1. *Rest-Frame Absolute Magnitudes*

For a given supernova s observed through filter O, we convert the apparent magnitude m_s datum observed at the modified Julian day (MJD) $t_{\rm MJD}$ to the absolute magnitude M_s at rest-frame phase t, via

$$M_s(t) = m_s(t) - \mu_{\Lambda\rm CDM}(z_s) - K^s_{OQ} - A^s_O, \qquad (4)$$

where z_s is the spectroscopic redshift of the supernova s with respect to the CMB, including any local flow models (see Table 2). The phase $t \equiv (t_{\rm MJD} - t_{B\max,s})/(1+z_{{\rm helio},s})$ is the rest-frame observation time, corrected for cosmological time dilation, $z_{{\rm helio},s}$ is the heliocentric redshift, and $t_{B\max}$ is the time of B-band maximum light. The term K_{OQ} is the K-correction from the observed band O to the rest-frame band Q, and A_O is the Milky Way foreground extinction defined as $A_O = R_O E(B-V)_{\rm MW}$, where R_O is the total-to-selective extinction ratio in filter O and $E(B-V)_{\rm MW}$ is the Milky Way color excess. We use the Schlafly & Finkbeiner (2011) dust reddening map for $E(B-V)_{\rm MW}$, and the CCM+O (O'Donnell 1994) reddening laws to determine R_O for the NIR and optical bands respectively. We assume a V-band total-to-selective extinction ratio for the Milky Way of $R_V = 3.1$.

We determine $t_{B\max}$ and compute the K-correction K^s_{OQ} terms using a module in the SNooPy LC package (Burns et al. 2011), which uses the normal SN Ia spectroscopic template of Hsiao et al. 2007 that is "mangled" to match the actual colors derived from the data.

The theoretical distance modulus is defined as

$$\mu_{\Lambda\rm CDM}(z_s) = 5\log_{10}\left[\frac{d_L(z_s)}{1\rm Mpc}\right] + 25 \qquad (5)$$

We assume the luminosity distance $d_L(z)$ for a spatially flat ΛCDM Universe, ignoring radiation, is approximately given by

$$d_L(z) = \left(\frac{c}{H_0}\right)(1+z)\int_0^z \frac{dz}{E(z)} \qquad (6)$$

where $E(z) = \sqrt{\Omega_{\rm m}(1+z)^3 + \Omega_\Lambda}$ and c is the speed of light. We assume fiducial values for the matter and energy density fractions of $\Omega_{\rm m} = 0.28$ and $\Omega_\Lambda = 0.72$ and a Hubble constant of $H_0 = 73.24$ km s^{-1} Mpc^{-1} (Riess et al. 2016).

Every value of M_s has an error variance

$$\sigma^2_M = \sigma^2_m + \sigma^2_{\mu_{\rm pec}} + \sigma^2_A + \sigma^2_{\rm Kcorr}, \qquad (7)$$

where σ_m is the measurement uncertainty of the apparent magnitude m_s, $\sigma_{\mu_{\rm pec}}$ is the uncertainty in the distance modulus $\mu_{\Lambda\rm CDM}(z_s)$ due to the peculiar velocity and redshift uncertainties, given as

$$\sigma^2_{\mu_{{\rm pec},s}}(z_s) = \left(\frac{5}{z_s\ln(10)}\right)^2\left[\left(\frac{\sigma_{\rm pec}}{c}\right)^2 + \sigma^2_{z,s}\right]. \qquad (8)$$

For the SN in Table 4 with independent distance estimates, we use those corresponding distance modulus uncertainties. The term σ_A in Eq. (7) is the uncertainty in the Milky Way dust extinction A_O computed as, $\sigma_A = R_O\,\sigma_{\rm EBV}$, where $\sigma_{\rm EBV}$ is the uncertainty in the Milky Way color excess $E(B-V)_{\rm MW}$, and $\sigma_{\rm Kcorr}$ is the K-correction uncertainty estimated using Monte Carlo simulations of the full optical and NIR dataset $\{m_s\}$ for a given SN. In this Monte Carlo approach, for each photometric datum at a given MJD time and band, $m_s(T_{\rm MJD})$, we simulate a realization of this datum by drawing a random value from a Gaussian distribution with mean and standard deviation equal to the measured values m_s and σ_m. For each simulated full optical+NIR dataset, we compute the K-corrections and then determine the mean and standard deviation of the distribution of the K-correction values for each photometric datum at a given MJD time and band. We use this standard deviation as an estimation of the uncertainty of the K-correction value for that datum.

3.2. *LC Fitting: Gaussian process*

The Gaussian process technique is a non-parametric Bayesian method that we use to fit the NIR LCs for each SN Ia in Table 2. A Gaussian process defines a prior over functions. Realizations from a GP, evaluated on a discrete set of times, are random vectors drawn from a joint multivariate Gaussian distribution, $\mathcal{N}$, of dimension equal to the number of components in the vector. Given a dataset, the GP formalism allows us to coherently determine the posterior mean function that fits the dataset along with its posterior covariance. The GP methodology is especially helpful in accounting for missing data (in our cases, phases with no observations), and when the data are correlated as in the case of the SN Ia LCs. Rasmussen & Williams (2006) provide an introduction to GPs for machine learning.

The following description applies to a LC of a single supernova in a given NIR band. We model the absolute magnitude M at phase t as a noisy measurement of the latent (true) absolute magnitude $\mathcal{M}$ at that phase, given by $M(t) = \mathcal{M}(t) + \epsilon$, where $\epsilon \sim \mathcal{N}(0, \sigma^2_M)$. In vector notation we express the collection of absolute magnitude data of a given LC as $\mathbf{M} \equiv [M(t_1), M(t_2), ..., M(t_n)]^\top$, measured at phases $\mathbf{t} \equiv [t_1, t_2, ..., t_n]^\top$, where n is the number of data in the LC, and $\top$ means the transpose.

Using GP, we estimate the posterior mean, $\boldsymbol{\mu}^{\rm post}$, and the posterior covariance, $\boldsymbol{\Sigma}^{\rm post}$, of the latent absolute magnitudes $\boldsymbol{\mathcal{M}}^* \equiv [\mathcal{M}(t_1^*), \mathcal{M}(t_2^*), ..., \mathcal{M}(t_{n^*}^*)]^\top$ on a regular grid of phases $\mathbf{t}^* \equiv [t_1^*, t_2^*, ..., t_{n^*}^*]^\top$, where n^* is the number of times in the grid determined from a sequence of phases between $t_{\min,s}$ and $t_{\max,s}$ in steps of 0.5 days, where $t_{\min,s}$ and $t_{\max,s}$ are the minimum and maximum phases in $\mathbf{t}^*$. Thus the number of times in the regular grid is $n^* = (t_{\max,s} - t_{\min,s})/0.5$. In Appendix A, we provide the mathematical details to determine $\boldsymbol{\mu}^{\rm post}$ and $\boldsymbol{\Sigma}^{\rm post}$.

3.2.1. *Normalization of the GP light curves*

Our goal with the GP fitting is to determine the *shape* of the LC to be used later in Section 3.3 to construct NIR templates to fit the data and estimate distance moduli. So once we determine the posterior mean and covariance of the latent absolute magnitude LC for a given supernova s using GP, we *normalize* the LCs to extract the information about their shape regardless of their absolute magnitudes. The normalized LC $L(t)$ is the function, over phase, of the difference in magnitudes relative to the peak phase, so that $L(t_{Bmax}) = 0$.

To estimate the distance moduli, we choose to use the phase of B-band maximum light, $t_{B\max}$, as the reference time to derive the distances. In Section 4.2, we also implement the estimation of distance moduli using the time of NIR-band maximum light instead of $t_{B\max}$ as the reference time.

We define the vector $\mathbf{L}$, corresponding to the normalized LC derived from the latent absolute magnitude LC $\boldsymbol{\mathcal{M}}^*$, evaluated on the phase grid $\mathbf{t}^*$, as

$$\mathbf{L} \equiv \boldsymbol{\mathcal{M}}^* - \mathcal{M}_0 \mathbf{1} \tag{9}$$

where $\mathcal{M}_0$ is the latent absolute magnitude at $t_{B\max}$ and $\mathbf{1}$ is a vector of dimension n^* with all its elements equal to one. Since this is a linear transformation of $\boldsymbol{\mathcal{M}}^*$ into $\mathbf{L}$, and $\boldsymbol{\mathcal{M}}^*$ is Gaussian, therefore $\mathbf{L}$ is also Gaussian and described completely by its mean $\boldsymbol{\mu}^{\rm L}$ and covariance $\boldsymbol{\Sigma}^{\rm L}$. See Appendix A.1 for details. In the next section we use $(\boldsymbol{\mu}^{\rm L}, \boldsymbol{\Sigma}^{\rm L})$ to construct the NIR light curve templates.

3.3. *Hierarchical Bayesian Model for the Normalized Magnitudes*

In this section, we describe how we construct NIR LC templates for the Y, J, H, and K_s bands that correspond to the mean *shape* of SN Ia LCs in each of these bands. To do so, we combine the normalized LCs described by $(\boldsymbol{\mu}^{\rm L}, \boldsymbol{\Sigma}^{\rm L})$, from all the supernovae at a given phase t^* using a hierarchical Bayesian model to determine the mean normalized magnitude. Then we repeat the procedure described below over all the phases in $\mathbf{t}^*$ to construct the final NIR LC templates.

First, we assume the normalized magnitude at phase t^*, $\mu_s^{\rm L}$, for the supernova s is drawn from a Gaussian distribution with true value η_s and standard deviation $\sigma_{\eta,s}$,

$$\mu_s^{\rm L} \sim \mathcal{N}(\eta_s, \sigma_{\eta,s}^2) \tag{10}$$

where the value of $\sigma_{\eta,s}^2$ is given by the (t_s^*, t_s^*) element in the diagonal of the covariance matrix $\boldsymbol{\Sigma}_s^{\rm L}$ [see Eq. (A11)]. Next, we assume that the set of values $\{\eta_s\}$ from all the $N_{\rm T}^*$ supernovae at phase t^*, are independent draws from a Gaussian population distribution with population mean θ and variance σ_θ^2,

$$p\left(\{\eta_s\}|\theta, \sigma_\theta^2\right) = \prod_{s=1}^{N_{\rm T}^*} \mathcal{N}\left(\eta_s|\theta, \sigma_\theta^2\right) \tag{11}$$

In Appendix B, we write the expression for the joint posterior distribution of the hierarchical model and describe additional decompositions in order to make the computations more tractable to determine the posterior inference[6] of $(\{\eta_s\}, \theta, \sigma_\theta)$ given the data $\{(\mu_s^{\rm L}, \sigma_{\eta,s})\}$ at phase t^*.

We repeat the above procedure for all phases in the range $t^* = (-10, 45)$ days, every 0.5 days, to determine (θ, σ_θ) for all t^* in this range. Figure 1 shows the $YJHK_s$ templates constructed with this procedure and Table 5 reports the numerical values of the templates. The posterior estimates of the population mean and variance of the normalized LC, $(\theta, \sigma_\theta^2)$, and the uncertainty in the determination of θ, are shown in Figure 1 as black curves, green bands, and blue bands, respectively.

4. HUBBLE DIAGRAM

We implement two different methods to derive the distance modulus for each supernova from the NIR LCs. We call them the *template method* and the *Gaussian-process method* (GP). The GP method requires data near the NIR maximum for all NIR bands being used, while the template method works for arbitrarily sampled data, even if the LC is sparse near maximum. For this reason, we have more objects in the template method Hubble diagrams. We describe these methods in more detail in the following sections.

Any of these NIR-only approaches approximately treat the information in each of the $YJHK_s$ bands as independent. However, this simple approach does

[6] We use the *median* of the posterior probability distribution as the best estimated value.

not take maximal advantage of the cross-band correlations between each of the NIR and optical bands, as is done using a more sophisticated hierarchical Bayesian model (e.g. BayeSN: Mandel et al. 2009, 2011, 2014). Nor does this approach use the fact that there is only one true distance to the supernova.

To alleviate this problem, we also derive the distance modulus for each supernova from the *combined* distance moduli in each NIR band. However, instead of computing a simple average distance modulus from the individual distance moduli, we instead estimate the covariance matrix of the $YJHK_s$ distance moduli (and submatrices of it) and then derive the *weighted* average distance modulus. The advantage of this procedure is that it takes into account the correlations among the magnitudes in the NIR bands and then derives more realistic mean distance moduli and their uncertainties. More details are in Section 4.3.

For our NIR-only Hubble diagrams, only NIR LCs are used to directly construct distance moduli. However, auxiliary optical data is used to estimate $t_{B\max}$, $\Delta m_{15}(B)$, and mangled K-corrections, and is employed in the input data selection cuts described in §2.1.

4.1. *Distance Modulus: Template method*

To determine the photometric distance modulus μ_s of the supernova s in a given NIR band, we use the normalized mean template, θ, computed in Section 3, to determine the apparent magnitude at phase zero, $m_{0,s} \equiv m_s(t=0)$, by fitting the template to the sometimes sparse photometric LC data $\{m_s(t)\}$. We define the difference

$$\Delta m_s(t) \equiv m_s(t) - \theta(t) - m_{0,s} \tag{12}$$

where $m_s(t)$ and $\theta(t)$ are the apparent magnitude and the magnitude of the normalized template at phase t, respectively. We can express this difference for all the n phases in a given LC as the vector,

$$\boldsymbol{\Delta m}_s \equiv \begin{pmatrix} \Delta m_s(t_1) \\ \Delta m_s(t_2) \\ \vdots \\ \Delta m_s(t_n) \end{pmatrix}. \tag{13}$$

Then, to determine $m_{0,s}$ we minimize the negative of the log likelihood function $\mathcal{L}(m_{0,s})$ defined as

$$-2\ln\mathcal{L}(m_{0,s}) = \boldsymbol{\Delta m}_s^\top \cdot \mathbf{C}^{-1} \cdot \boldsymbol{\Delta m}_s + \text{constant}, \tag{14}$$

where $\mathbf{C}$ is the n-dimensional covariance matrix where the (t_i, t_j) component is given by:

$$C_{ij} \equiv \mathrm{Cov}\left(\Delta m_s(t_i), \Delta m_s(t_j)\right) \tag{15}$$

$$= \sigma_\theta(t_i)\sigma_\theta(t_j)\exp\left[-\frac{(t_i-t_j)^2}{2l^2}\right] + \hat{\sigma}^2_{m,s}(t_i)\delta_{ij}, \tag{16}$$

where $\sigma_\theta(t)$ is the population standard deviation of the sample distribution of magnitudes at phase t, determined from Eq. (B14) during the training process used to construct the mean LC template, $\hat{\sigma}^2_{m,s}(t_i)$ is the photometric error of the datum $m_s(t_i)$, and l is the hyperparameter of GP kernel determined from Eq. (A9) and with values shown in Table 15.

From Eq. (14), we can calculate an analytic expression for the maximum likelihood estimator (MLE) of the apparent magnitude at B-band maximum light, $\hat{m}_{0,s}$, given by:

$$\hat{m}_{0,s} = \left[\sum_{i,j}^{n} (C^{-1})_{ij}\right]^{-1} \times \sum_{i}^{n}\left[\Big(m_s(t_i) - \theta(t_i)\Big)\sum_{j}^{n}(C^{-1})_{ij}\right], \tag{17}$$

with the MLE of the uncertainty of $\hat{m}_{0,s}$ given as

$$\hat{\sigma}_{\mathrm{fit},s} = \left[\sum_{i,j}^{n}(C^{-1})_{ij}\right]^{-1/2}, \tag{18}$$

which corresponds to the fitting error of the light curve. This error incorporates the photometric measurement error and the sparsity of the actual data points.

Now, from the distribution of absolute magnitudes at phase zero estimated as $M_{0,s} \equiv \hat{m}_{0,s} - \mu_{\Lambda\mathrm{CDM}}(z_s)$ (see Fig. 2), we compute the sample mean absolute magnitude, $\langle M_0 \rangle$, and the sample standard deviation of the distribution, obtaining the values reported in Table 6. The sample standard deviation describes the total scatter of the absolute magnitude estimates. Below, we decompose this into the contributions from peculiar velocity-distance errors, measurement/fitting errors, and intrinsic dispersion.

Finally, we estimate the photometric distance modulus for supernova s in a given NIR band as

$$\hat{\mu}_s = \hat{m}_{0,s} - \langle M_0 \rangle\,. \tag{19}$$

The uncertainty on $\hat{\mu}_s$ is composed of two sources of errors: the fitting uncertainty $\hat{\sigma}_{\mathrm{fit},s}$ estimated in Eq.

Table 6. Mean $YJHK_s$ absolute magnitudes at $t_{B\max}$ or $t_{\rm NIR}$ max.

Band	$N_{\rm SN}$	$\langle M \rangle$ (mag)	Std. deviation (mag)
Template method			
Y	44	−18.12	0.15
J	87	−18.34	0.17
H	81	−18.18	0.17
K_s	32	−18.35	0.21
Gaussian-process method at NIR max			
Y	29	−18.39	0.11
J	52	−18.52	0.14
H	44	−18.30	0.11
K_s	14	−18.37	0.18
Gaussian-process method at B max			
Y	29	−18.16	0.12
J	52	−18.34	0.15
H	44	−18.19	0.12
K_s	14	−18.28	0.17

NOTE— We use the sample mean values of the absolute magnitudes, $\langle M \rangle$, in each band to determine the distance modulus in the template and GP methods using Eqs. (19) and (23) respectively. For the template method $\langle M \rangle \equiv \langle M_0 \rangle$ and for the GP method $\langle M \rangle \equiv \langle M_{\rm NIRmax} \rangle$, $\langle M_{\rm Bmax} \rangle$. Figs. 2, 3 and 4 show the histograms of $M_{0,s}$ and $M_{{\rm NIRmax},s}$, respectively. In this table, we also present the sample standard deviation of the absolute magnitude sample distribution just as a reference, we do not use those values in any part of the computations.

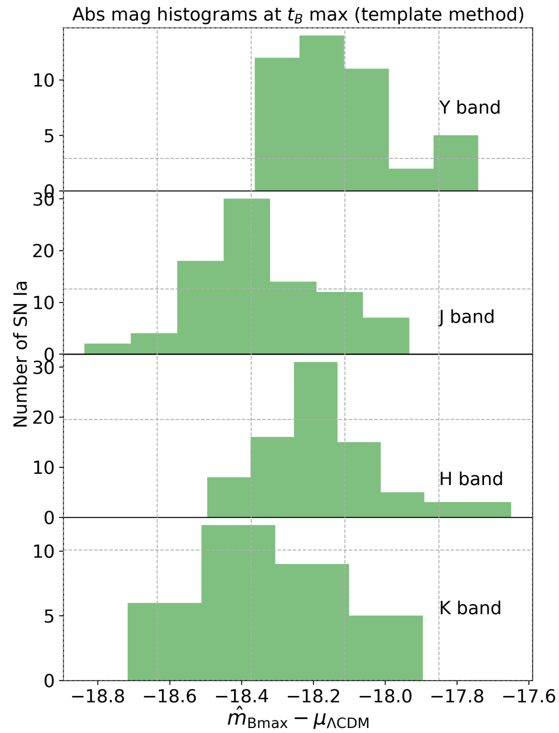

Figure 2. Histograms of the absolute magnitudes at phase zero ($t^* = t_{B\max}$), defined as $M_{0,s} \equiv \hat{m}_{0,s} - \mu_{\Lambda\rm CDM}(z_s)$ for the SN Ia sample using the template method. The sample mean, standard deviation, and the number of supernovae in each histogram are shown in Table 6.

(18) for each individual supernova, and the *intrinsic scatter*, $\sigma_{\rm int}$, which primarily comes from the intrinsic variation of SN Ia absolute magnitudes and is estimated by fitting an entire sample of SN Ia on the Hubble diagram (see Appendix C for more details). So the variance of the photometric distance modulus is given as

$$\hat{\sigma}^2_{\mu,s} = \hat{\sigma}^2_{{\rm fit},s} + \hat{\sigma}^2_{\rm int}. \tag{20}$$

The Hubble residual for supernova s is defined as

$$\Delta\mu_s \equiv \hat{\mu}_s - \mu_{\Lambda\rm CDM}(z_s). \tag{21}$$

The uncertainty on $\mu_{\Lambda\rm CDM}(z_s)$ is given by Eq. (8). The variance on the Hubble residual for supernova s, $\sigma^2_{\Delta,s}$, comes from the propagation of uncertainties on $\hat{\mu}_s$ and $\mu_{\Lambda\rm CDM}(z_s)$, it is,

$$\sigma^2_{\Delta,s} = \hat{\sigma}^2_{{\rm fit},s} + \hat{\sigma}^2_{\rm int} + \sigma^2_{\mu_{\rm pec},s}. \tag{22}$$

In addition to $\sigma_{\rm int}$, to quantify the dispersion in the Hubble residuals, we also compute both the RMS and the inverse-variance weighted root-mean-square (wRMS, see Appendix C). The RMS and wRMS are measures of the total scatter in the Hubble Diagram. The wRMS is relatively insensitive to the assumed value of the peculiar velocity uncertainty, and the formula for the RMS does not depend on the asssumed value of $\sigma_{\rm pec}$ at all and is therefore more straightforward to compare with other works.

For the template method, the values of $\hat{\mu}_s$, $\sigma_{\rm int}$ and wRMS in the Hubble diagram residual for a given NIR band depend on the phase range of the NIR LC template used to determine the distance modulus. We found that phase range of $t^* = (-8, 30)$ days in each of the $YJHK_s$ bands minimized the scatter in the Hubble residual, as measured by $\sigma_{\rm int}$ or wRMS.

Table 11 reports the distance moduli $\hat{\mu}_s$ and their fitting uncertainty $\hat{\sigma}_{{\rm fit},s}$ we obtain with this procedure for

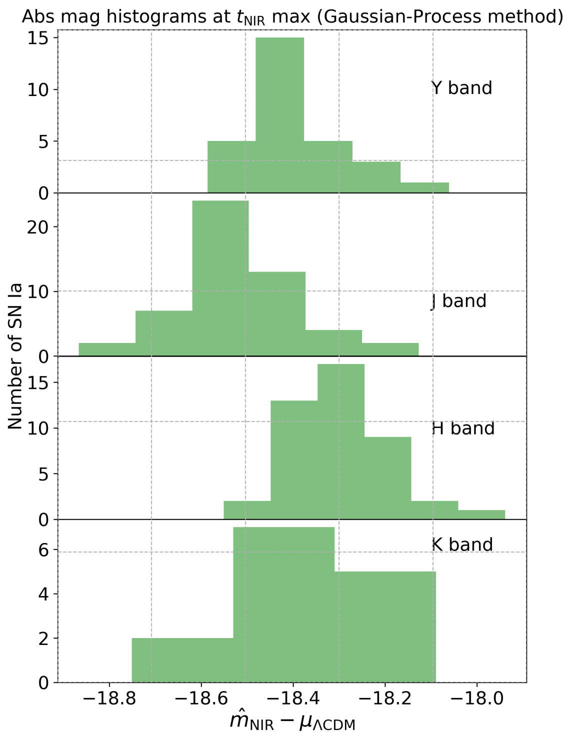

Figure 3. Histograms of the absolute magnitudes at phase $= \mathrm{NIR}_{\max}$, defined as $M_{\mathrm{NIR}_{\max},s} \equiv \hat{m}_{\mathrm{NIRmax},s} - \mu_{\Lambda\mathrm{CDM}}(z_s)$ for the SN Ia sample in the GP method at NIR max. The sample mean, standard deviation, and the number of supernovae in each histogram are shown in Table 6.

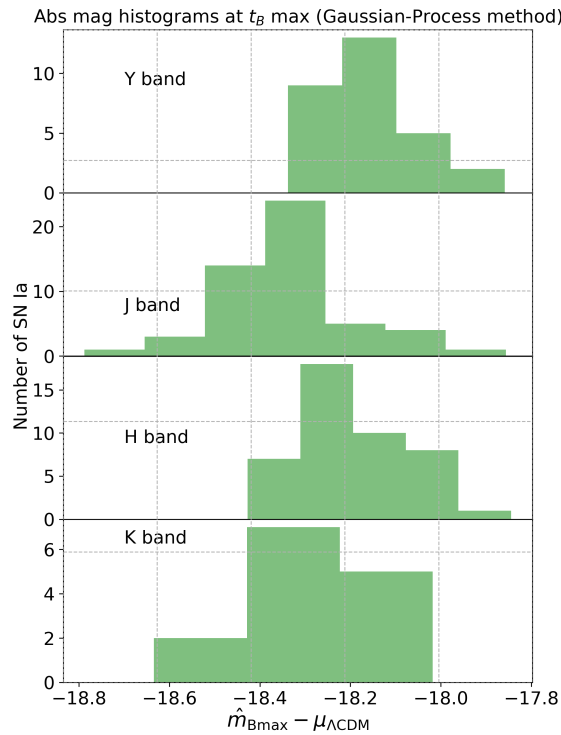

Figure 4. Histograms of the absolute magnitudes at phase $= B_{\max}$, defined as $M_{B_{\max},s} \equiv \hat{m}_{B\mathrm{max},s} - \mu_{\Lambda\mathrm{CDM}}(z_s)$ for the SN Ia sample in the GP method at B max. The sample mean, standard deviation, and the number of supernovae in each histogram are shown in Table 6.

each supernova in each band, and Fig. 11 shows the Hubble diagram and residuals.

4.2. *Distance Modulus: Gaussian-process Method*

The nearby low-z NIR sample now contains a sufficient number of SN Ia well-sampled around maximum light in the $YJHK_s$-bands, that we can explore referencing various distance estimation approaches to the times of these NIR maxima, rather than B-max, for which there has long been sufficiently well sampled optical photometry.

An alternative approach that we implement to derive distance moduli is by determining the apparent magnitude at the time of NIR maximum light, t_{NIRmax}, and B maximum light, $t_{B\mathrm{max}}$, using the GP technique to interpolate the LC data. The method follows the same procedure as the one described in Section 3.2, but instead of GP fitting the absolute magnitude LCs, $\{M_s(t)\}$, we directly GP fit the *apparent* magnitude LCs, $\{m_s(t)\}$. By doing this, we do not include $\sigma_{\mu_{\mathrm{pec}}}$ in the error budget for each $m_s(t)$ because we do not subtract $\mu_{\Lambda\mathrm{CDM}}(z)$.

To determine the posterior mean of the apparent magnitude LC, $\{\bar{m}_s(t^*)\}$, and the posterior covariance of a GP fit to $\{m_s(t)\}$ we use the Eqs. (A7) and (A8) where we set $\sigma^2_{\mu_{\mathrm{pec}},s} = 0$. For each LC, we use the average of the apparent magnitude data as the GP prior mean, and use the same values for the hyperparameters of the GP kernel shown in Table 15, given that the shape and dispersion of the apparent magnitude LC data is very similar to the absolute magnitude LCs we fitted with GP in Section 3.2 for each supernova. We verified that the GP fits to the LCs are insensitive to these choices.

We only consider LCs that have data either around t_{NIRmax} or $t_{B\mathrm{max}}$ so that we can determine the GP fit at those references phases. By construction, $t_{B\mathrm{max}}$ corresponds to the phase $= 0$ days. For the case of t_{NIRmax} we limit the search for the maximum to the phase range $-8.5 < t_{\mathrm{NIRmax}} < -2.5$ days to remove cases where maximum of the posterior mean happens *after* $t_{B\mathrm{max}}$, which we found can be artifacts of the GP fit when there are too few data points before $t_{B\mathrm{max}}$. For the rest of this section we denote the subscripts "NIRmax" and "Bmax" simply as "max".

From each set $\{\bar{m}_s(t^*)\}$, we estimate, $\hat{m}_{\max,s}$, the GP interpolated apparent magnitude at $t_{\max,s}$. Then we estimate the distance modulus as

$$\hat{\mu}_s = \hat{m}_{\max,s} - \langle M_{\max} \rangle \tag{23}$$

where $\langle M_{\max} \rangle$ is the mean absolute magnitude at $t_{\max,s}$ from all the supernovae in a given NIR band (see Fig. 3), with $M_{\max,s} \equiv \hat{m}_{\max,s} - \mu_{\Lambda\mathrm{CDM}}(z_s)$. The uncertainty on the photometric distance modulus $\hat{\mu}_s$ in this case is $\hat{\sigma}_{\mathrm{fit},s}$, which is equal to the uncertainty in the apparent magnitude at $t_{\max,s}$ inferred from the GP fit to the LC.

Figure 12 shows Hubble diagrams constructed from the distance moduli inferred from the GP method for each of the $YJHK_s$ bands, with numerical values reported in Table 12.

4.3. *Distance modulus from the combined NIR bands*

From the estimated distance moduli $(\hat{\mu}_s^Y, \hat{\mu}_s^J, \hat{\mu}_s^H, \hat{\mu}_s^K)$ for a given supernova s determined from each NIR band using either of the three methods described above, we estimate the weighted average of the distance modulus μ_s from each method. First we define the vector of residuals

$$\delta\boldsymbol{\mu}_s \equiv \begin{pmatrix} \hat{\mu}_s^Y - \mu_s \\ \hat{\mu}_s^J - \mu_s \\ \hat{\mu}_s^H - \mu_s \\ \hat{\mu}_s^K - \mu_s \end{pmatrix}. \tag{24}$$

where $\hat{\mu}_s^Y, \hat{\mu}_s^J, \hat{\mu}_s^H, \hat{\mu}_s^K$ are determined by either Eqs. (19) or (23), for the template or GP methods, respectively. Then, to estimate μ_s, we minimize the negative of the likelihood function $\mathcal{L}(\mu_s)$ defined as

$$-2\ln\mathcal{L}(\mu_s) = \delta\boldsymbol{\mu}_s^\top \cdot C_\mu^{-1} \cdot \delta\boldsymbol{\mu}_s + \text{constant}, \tag{25}$$

where C_μ is the sample covariance matrix computed from the Hubble residuals (see Eq. (21)) $\{\Delta\mu_s^Y, \Delta\mu_s^J, \Delta\mu_s^H, \Delta\mu_s^K\}$, the collection of distance-modulus residuals from all SN Ia with observations in the four $YJHK_s$ bands. For supernovae with observations in only three, two, or one bands, we construct the respective covariance matrices based on those supernova subsamples, and the vector defined in Eq. (24) becomes three, two, or one dimensional, respectively. In Appendix D, we provide numerical values of the covariance matrix C_μ for these different subcases.

We derive an analytic expression for the minimization of Eq. (25) with respect to μ_s and obtain the maximum likelihood estimate for the combined distance modulus given by,

$$\hat{\mu}_s = \sum_b w_b\, \hat{\mu}_s^b \tag{26}$$

where $\hat{\mu}_s^b \in \{\hat{\mu}_s^Y, \hat{\mu}_s^J, \hat{\mu}_s^H, \hat{\mu}_s^K\}$ (the index b stands for *band*), and

$$w_b = \left[\sum_{b'} (C^{-1})_{bb'}\right] \times \left[\sum_{b',b''} (C^{-1})_{b'b''}\right]^{-1}. \tag{27}$$

Now, assuming that the uncertainties in the distance modulus estimated from each individual $YJHK_s$ band, $\hat{\sigma}_{\mathrm{fit},s,Y}$, $\hat{\sigma}_{\mathrm{fit},s,J}$, $\hat{\sigma}_{\mathrm{fit},s,H}$, $\hat{\sigma}_{\mathrm{fit},s,K}$, are independent between bands b and also independent of the intrinsic scatter σ_{int}, then we can propagate the uncertainty in the combined distance modulus due to the fitting only as:

$$\hat{\sigma}_{\mathrm{fit},s} = \sqrt{\sum_b w_b^2\, \hat{\sigma}_{s,b}^2} \tag{28}$$

where $\hat{\sigma}_{s,b} \equiv \hat{\sigma}_{\mathrm{fit},s,Y}$, $\hat{\sigma}_{\mathrm{fit},s,J}$, $\hat{\sigma}_{\mathrm{fit},s,H}$, $\hat{\sigma}_{\mathrm{fit},s,K}$.

The last column in Tables 11-13 show the combined distance moduli we obtain with this procedure for the template and GP methods respectively. The reported uncertainties correspond to $\hat{\sigma}_{\mathrm{fit},s}$ in all cases.

4.4. *Distance modulus from optical bands*

We wish to assess how well the SN Ia observed in NIR bands perform as standard candles, specifically when using t_{NIRmax} as opposed to $t_{B\max}$, as the time reference to estimate their distance. To do so, we determine the distance moduli using only *optical BVR*-bands LCs for exactly the same 56 supernovae in the "any $YJHK_s$" Hubble diagram set that was used for the GP method (see left panel in Fig. 6 and the SN listed in Table 12). Then we can compare the intrinsic scatter and RMS or wRMS in the Hubble-diagram residuals between the optical-only and NIR-only Hubble diagrams. A smaller intrinsic scatter, wRMS, or RMS, including the uncertainties, would indicate evidence that SN Ia are better standard candles using that data and Hubble diagram construction method.

4.4.1. *SALT2 distance modulus*

We use the optical photometric data compiled in the public SNANA (Kessler et al. 2009) database[7] but replace the CMB redshift values in the SNANA photometric files with the z_{CMB} values in Table 2. Using the latest SALT2 model (SALT2.JLA-B14) (Guy et al. 2007) already trained on the JLA sample (Betoule et al. 2014), we fit the optical data and determine the SALT2 light-curve fit parameters for each supernova. For the CSP data, we added an additional 0.01 mag in quadrature to the photometric errors to have a more conservative

[7] http://snana.uchicago.edu. Version Oct 18, 2017.

uncertainties on those values when fitting the data in SALT2. We use the SALT2 outputs including the apparent magnitude m_B at B-band maximum light, the stretch parameter x_1, and the color term c, as well as their correlations.

We convert the SALT2-fit parameters to distance moduli for each supernova using the Tripp formula (Tripp 1998),

$$\mu_s = m_{B,s} - M_B + \alpha x_{1,s} - \beta c_s, \tag{29}$$

where M_B is the expected absolute magnitude at B-band maximum light for a SN Ia with $x_1 = 0, c = 0$, while α and β are coefficients parametrizing correlations between luminosity and stretch or luminosity and color, respectively.

For the global parameters M, α, β we use the values reported by Scolnic et al. (2018); $\alpha = 0.147$, $\beta = 3.00$, and assume the fiducial values of $H_0 = 73.24\ \mathrm{km\,s^{-1}\,Mpc^{-1}}$ and $M_B = -19.36$ mag. We then adjust the latter to $M_B = -19.44$ mag so that the weighted-average Hubble residual is zero.

The standard deviation of the measurement error $\sigma_{\mathrm{fit},s}$ from the SALT2 fitting comes from propagating the uncertainties on Eq. (29), including their correlations. Interestingly we found that for the supernovae with high Milky Way color excess $E(B-V) > 0.2$ the uncertainty on $m_{B,s}$ is larger than the propagated uncertainty on the SALT2 distance modulus, μ_s, derived from optical bands. This evidence further emphasizes how SN Ia are more negatively affected by dust when deriving distances using optical data, as compared to NIR observations.

The variance of the photometric distance modulus is given by

$$\sigma^2_{\mu,s} = \sigma^2_{\mathrm{fit},s} + \sigma^2_{\mathrm{int}}. \tag{30}$$

Using SALT2 in this way, we obtain an intrinsic scatter in the Hubble residuals of $\sigma_{\mathrm{int}} = 0.133 \pm 0.022$, an inverse-variance weighted RMS of wRMS$=0.174 \pm 0.020$ mag, and a simple RMS $= 0.179 \pm 0.018$ mag. The third column of Table 14 and the left panel of Fig. 9 show the distance moduli derived from the SALT2 fits, along with the Hubble diagram and residuals, respectively. The uncertainties shown in Table 14 and Fig. 9 are the values of $\sigma_{\mathrm{fit},s}$.

Note that we are not applying the usual SALT2 cuts to this subsample of SN because we are interested in comparing the scatter in the Hubble residuals using exactly the same 56 SN Ia used in the "any $YJHK_s$" Hubble diagram for the GP method. We find that when applying the SALT2 cut on color, $-0.3 < c < 0.3$, there is only 1 SN Ia in the subsample that does not pass this cut. All SN Ia in the sample pass these SALT2 cuts: $-3 < x_1 < 3$, uncertainty in $x_1 < 1$, and uncertainty in $t_{B\max} < 2$ days. However, 21 SN Ia fail to pass the SALT2 cut requiring that the probability that the data are represented by the model, given the χ^2 per degree of freedom of the fit, is larger than 0.001 (a.k.a, FITPROB > 0.001). However, a low fit probability does not necessarily indicate a poor SN Ia light curve fit and may instead be an indication that the photometric uncertainties or the model uncertainties are unrealistically small. We visually inspected the light curve fits of these 21 SN Ia, finding that they are reasonably well-fit by the model and can therefore be used to yield accurate distance measurements.

4.4.2. *SNooPy distance modulus*

As a second cross check of the scatter in the optical-only Hubble diagram, we also fit the BVR-bands LCs using the SNooPy LC fitting package's `EBV_model` (Burns et al. 2011), where every observed apparent magnitude m_s in band $O \equiv B, V, R$ is compared to the model

$$\begin{aligned} m_s(t) = {} & \mu_s + T_Q(t, \Delta m_{15,s}) + M_Q(\Delta m_{15,s}) \\ & + R_O E(B-V)_{\mathrm{MW},s} + R_Q E(B-V)_{\mathrm{host},s} + \\ & K^s_{OQ}\Big(z_s, t, E(B-V)_{\mathrm{MW},s}, E(B-V)_{\mathrm{host},s}\Big), \end{aligned} \tag{31}$$

where $T_Q(t, \Delta m_{15,s})$ is a light-curve template for the rest-frame band Q that depend on t and $\Delta m_{15,s}$, and $M_{Q,s}(\Delta m_{15,s})$ is the absolute magnitude band Q. In this model, the free parameters that SNooPy estimates (along with their uncertainties) are μ_s, $\Delta m_{15,s}$, $E(B-V)_{\mathrm{host},s}$ and $t_{B\max}$. We consider the estimated uncertainty on μ_s output by SNooPy as the $\sigma_{\mathrm{fit},s}$ in our analysis. We refer the reader to Burns et al. (2011) for details on how SNooPy estimates the uncertainty on μ_s.

We obtain an intrinsic scatter in the Hubble residuals of $\sigma_{\mathrm{int}} = 0.128 \pm 0.018$, a wRMS$= 0.159 \pm 0.019$ mag, and a RMS $= 0.174 \pm 0.021$ mag. The fourth column of Table 14 and right panel of Fig. 9 show the distance moduli derived from the SNooPy fits, along with the Hubble diagram and residuals, respectively.

5. DISCUSSION

Tables 7 and 8 summarize the scatter in the Hubble residuals measured with the either the intrinsic scatter σ_{int}, the wRMS, or the RMS. We compute these both for our fiducial peculiar velocity uncertainty of $\sigma_{\mathrm{pec}} = 150$ km/s as well as the value $\sigma_{\mathrm{pec}} = 250$ km/s used in Scolnic et al. (2018).

While the formula for RMS in Eq. C23 does not depend on the assumed value of σ_{pec} (see Appendix C), the value of σ_{int} is quite sensitive to the assumed value of σ_{pec}. In particular, larger assumed values of σ_{pec} yield

Table 7. Hubble Residual Intrinsic Scatter, $\sigma_{\rm int}$, and RMS.

Band	Method	$N_{\rm SN}$	$\sigma_{\rm int}$ [mag] ($\sigma_{\rm pec} = 150$ km/s)	$\sigma_{\rm int}$ [mag] ($\sigma_{\rm pec} = 250$ km/s)	wRMS [mag] ($\sigma_{\rm pec} = 150$ km/s)	RMS [mag]
Optical BVR	SALT2	56	0.133 ± 0.022	0.107 ± 0.025	0.174 ± 0.020	0.179 ± 0.018
Optical BVR	SNooPy	56	0.128 ± 0.018	0.111 ± 0.020	0.159 ± 0.019	0.174 ± 0.021
any $YJHK_s$	Template	56	0.112 ± 0.016	0.096 ± 0.019	0.140 ± 0.016	0.138 ± 0.014
any $YJHK_s$	GP (NIR max)	56	0.047 ± 0.018	$0.000 \pm 0.000^*$	0.100 ± 0.013	0.117 ± 0.014
any $YJHK_s$	GP (B max)	56	0.066 ± 0.016	0.044 ± 0.023	0.106 ± 0.010	0.115 ± 0.011

NOTE— We compare the Hubble residual scatter for the optical and NIR bands using exactly the same 56 supernovae for several methods. We compute the intrinsic scatter, $\sigma_{\rm int}$ (see Appendix C), the inverse-variance weighted root-mean square (wRMS), and the simple RMS, using two standard LC fitters: SALT2 (Guy et al. 2007) and SNooPy (Burns et al. 2011) to fit the optical BVR-band LC data, as well as the three NIR methods we implement in this work: NIR LC templates at B-max [Template], and GP regression at NIR-max [GP (NIR max) or B-band maximum [GP (B max)]. We are limited to 56 SN Ia because these are all the supernovae that we can fit using the GP method. Columns 4 and 5 show $\sigma_{\rm int}$, assuming $\sigma_{\rm pec} = 150$ and 250 km/s respectively. The estimated intrinsic scatter $\sigma_{\rm int}$ decreases as the assumed peculiar velocity uncertainty $\sigma_{\rm pec}$ increases from commonly assumed values of 150 km/s (Radburn-Smith et al. 2004) to 250 km/s (Scolnic et al. 2018), making $\sigma_{\rm int}$ somewhat model dependent. By contrast, the wRMS value only changes by thousandths of a magnitude for $\sigma_{\rm pec}$ in the same range. Column 6 shows the wRMS assuming $\sigma_{\rm pec} = 150$ km/s. Column 7 shows the simple RMS, which makes no assumptions about error weighting and does not depend on $\sigma_{\rm pec}$. Both optical methods apply LC shape and dust corrections but still yield a larger scatter than the NIR methods quantified with any of $\sigma_{\rm int}$, wRMS or RMS (see also Table 8). Figs. 6-9 show Hubble diagrams and residuals for this subsample.

* For $\sigma_{\rm pec} = 250$ km/s, the estimated value of $\sigma_{\rm int}$ is consistent with 0. See the paragraph below Eq. (B.7) in Blondin et al. (2011) for the explicit approximation we use to estimate the uncertainty, which breaks down at $\sigma_{\rm int} = 0$.

smaller inferred values of $\sigma_{\rm int}$ (see columns 4 and 5 of Tables 7 and 8). The assumption of $\sigma_{\rm pec} = 150$ km/s in this work therefore yields a more conservative estimate of $\sigma_{\rm int}$ compared with larger values of $\sigma_{\rm pec}$ because, in the latter case, most of the scatter in the Hubble residuals can be explained as arising solely from peculiar velocities. For instance, the Hubble residuals using only H-band LCs from the GP (NIR max) method produce an intrinsic scatter of zero when assuming $\sigma_{\rm pec} = 250$ km/s.

We found that wRMS is less sensitive than $\sigma_{\rm int}$ to the assumed value of $\sigma_{\rm pec}$, producing differences of ~ 0.001 mag between $\sigma_{\rm pec} = 150$ and $\sigma_{\rm pec} = 250$ km/s.

Of the three NIR methods used to derive distance moduli, the GP method at NIR max yields smaller RMS, wRMS, and intrinsic scatter in the Hubble residuals than the template and GP methods at B max methods applied to the same 56 SN Ia with data from any of the $YJHK_s$ bands. When we combine the GP distance moduli for these same SN Ia referenced to the NIR maxima, we find an RMS $= 0.117 \pm 0.014$, wRMS $= 0.100 \pm 0.013$, and intrinsic scatter of $\sigma_{\rm int} = 0.047 \pm 0.018$ mag. Using the GP method instead referenced to B-max for the same SN Ia yields RMS $= 0.115 \pm 0.011$, wRMS $= 0.106 \pm 0.010$, and $\sigma_{\rm int} = 0.066 \pm 0.016$ mag. The NIR maxima thus yield comparable dispersion in the Hubble residuals than B-max for each individual NIR band subset with the GP method (see Table 10).

By comparison, when using the NIR template method referenced to B-max for these same SN Ia, we find a larger value of RMS $= 0.138 \pm 0.014$, wRMS $= 0.140 \pm 0.016$, and $\sigma_{\rm int} = 0.112 \pm 0.016$ mag.

When we create the Hubble diagram using optical-only LCs of the same 56 supernovae, we find RMS $= 0.179 \pm 0.018$, wRMS $= 0.174 \pm 0.020$, and $\sigma_{\rm int} = 0.133 \pm 0.022$ mag when using SALT2, and RMS $= 0.174 \pm 0.021$, wRMS $= 0.159 \pm 0.019$, and $\sigma_{\rm int} = 0.128 \pm 0.018$ mag with SNooPy.

Overall, as shown in Table 9, depending on the NIR $YJHK_s$ subset, the NIR-only GP method yields a RMS in the Hubble residuals that is as much as $\sim$ 2.3-4.1σ *smaller* than the SALT2 and SNooPy fits using optical-only BVR data. Furthermore, our "any $YJHK_s$" set of 56 SN Ia yields a RMS for our GP method at NIR max that is 0.057 ± 0.025 mag smaller than SNooPy and 0.062 ± 0.023 mag smaller that SALT2 applied to the corresponding BVR data, again at the $\sim 2.7\sigma$ level. We interpret the smaller intrinsic scatter as additional evidence, at the $\sim$ 2.5-3.1σ level, that NIR SN Ia LCs at NIR maximum, without LC shape or dust corrections, are already *better* standard candles than optical-only SN Ia LCs referenced to B-max that apply such corrections. In addition, it is possible that NIR data or a combination of NIR and optical could yield even smaller intrinsic scatter if employing a method that applies LC shape and dust corrections, for example, using

Table 8. Hubble Residual Intrinsic Scatter, $\sigma_{\rm int}$, and RMS.

Band	Method	$N_{\rm SN}$	$\sigma_{\rm int}$ [mag] ($\sigma_{\rm pec} = 150$ km/s)	$\sigma_{\rm int}$ [mag] ($\sigma_{\rm pec} = 250$ km/s)	wRMS [mag] ($\sigma_{\rm pec} = 150$ km/s)	RMS [mag]
Y	Template	44	0.105 ± 0.018	0.093 ± 0.021	0.139 ± 0.013	0.152 ± 0.016
Y	GP (NIR max)	29	0.066 ± 0.020	0.037 ± 0.032	0.102 ± 0.015	0.111 ± 0.018
Y	GP (B max)	29	0.080 ± 0.019	0.062 ± 0.024	0.110 ± 0.013	0.118 ± 0.017
J	Template	87	0.136 ± 0.016	0.122 ± 0.018	0.170 ± 0.013	0.175 ± 0.013
J	GP (NIR max)	52	0.107 ± 0.017	0.090 ± 0.021	0.136 ± 0.017	0.139 ± 0.016
J	GP (B max)	52	0.124 ± 0.019	0.110 ± 0.021	0.153 ± 0.020	0.151 ± 0.021
H	Template	81	0.126 ± 0.016	0.112 ± 0.018	0.162 ± 0.015	0.166 ± 0.016
H	GP (NIR max)	44	0.032 ± 0.027	$0.000 \pm 0.000^*$	0.095 ± 0.010	0.114 ± 0.015
H	GP (B max)	44	0.063 ± 0.020	0.037 ± 0.033	0.111 ± 0.011	0.120 ± 0.013
K	Template	32	0.175 ± 0.032	0.163 ± 0.035	0.211 ± 0.023	0.207 ± 0.020
K	GP (NIR max)	14	0.093 ± 0.054	0.077 ± 0.060	0.163 ± 0.033	0.179 ± 0.029
K	GP (B max)	14	0.094 ± 0.054	0.059 ± 0.069	0.162 ± 0.035	0.170 ± 0.027
any $YJHK_s$	Template	89	0.123 ± 0.014	0.107 ± 0.016	0.154 ± 0.013	0.161 ± 0.013
JH	Template	81	0.127 ± 0.015	0.112 ± 0.017	0.158 ± 0.015	0.164 ± 0.015
JH	GP (NIR max)	42	0.039 ± 0.024	$0.000 \pm 0.000^*$	0.096 ± 0.011	0.114 ± 0.016
JH	GP (B max)	42	0.069 ± 0.019	0.046 ± 0.028	0.112 ± 0.014	0.118 ± 0.015
YJH	Template	40	0.093 ± 0.018	0.080 ± 0.022	0.121 ± 0.013	0.137 ± 0.018
YJH	GP (NIR max)	21	0.044 ± 0.028	$0.000 \pm 0.000^*$	0.088 ± 0.014	0.087 ± 0.013
YJH	GP (B max)	21	0.068 ± 0.023	0.056 ± 0.031	0.097 ± 0.014	0.098 ± 0.014

Note— Scatter in the Hubble residuals for different NIR band subsets, quantified by the intrinsic scatter, $\sigma_{\rm int}$, the wRMS, and the simple RMS, using three methods: NIR LC templates at B-max [Template], and GP regression at NIR-max [GP (NIR max) or B-band maximum [GP (B max)]. Column 3 shows the number of SN Ia in each Hubble diagram. Also see Table 7. Columns 4 and 5 show $\sigma_{\rm int}$, assuming $\sigma_{\rm pec} = 150$ and 250 km/s respectively. Note that by increasing the value of $\sigma_{\rm pec}$, the $\sigma_{\rm int}$ decreases even to zero in some cases with uncertainty denoted by ∞. For the GP method, we use exactly the same supernovae at B-max or NIR-max. For all NIR band subsets, the GP (NIR max) method produces the smallest scatter, followed by the GP (B-max) method, while the template method always yields the largest scatter and wRMS. Figs. 5-7 and 11-13 show Hubble diagrams and residuals for most of the NIR subsets listed in this table.

* For $\sigma_{\rm pec} = 250$ km/s, the estimated value of $\sigma_{\rm int}$ in these cases is consistent with zero. See the paragraph below Eq. (B.7) in Blondin et al. (2011) for the explicit approximation we use to estimate the uncertainty, which breaks down at $\sigma_{\rm int} = 0$.

a hierarchical Bayesian approach like BayeSN (Mandel et al. 2009, 2011).

In Table 9, we note that the uncertainty on the difference in the dispersion estimates between any two methods has been computed conservatively. The uncertainty of the dispersion of each individual method has been computed independently, and then the uncertainty in the difference is found by adding in quadrature, assuming the independence of the samples and therefore the individual uncertainties. However, this ignores the fact that the supernovae in our optical sample are exactly the same ones as those in our NIR sample. Therefore, the actual peculiar velocity-distance errors must be the same in each sample (and not just the variance of these errors). Because of this common component of scatter, the dispersion estimate for the optical Hubble Diagram is (positively) correlated with that for the NIR Hubble Diagram in each comparison. The effect of this positive correlation is to reduce the variance in the differences in dispersion. Using our estimates of $\sigma_{\rm int}$, $\sigma_{{\rm fit},s}$ and $\sigma_{\mu_{\rm pec},s}$ for the sample and each method, we have run simulations to account for this correlation and quantify this effect. For example, we find that the uncertainty in ΔRMS for "SNooPy - any $YJHK_s$" is $\sim 30\%$ smaller than naive uncertainty assuming independent samples, resulting in a significance greater than 3σ.

For the Hubble diagrams created using just one of the $YJHK_s$ bands, when using the GP method at NIR max, the Y band has the smallest scatter with a RMS of 0.111 ± 0.018 mag. When using the template method, the Y band has also the smallest scatter with RMS $= 0.152 \pm 0.016$.

For every individual band and subset of NIR bands shown in Table 10, the GP method yields *smaller* intrinsic scatter when referencing to NIR max instead of B max, by mean amounts of up to ~ 0.03 mag for the same SN Ia at up to the $\sim$1.0σ level. While not as statistically significant as the NIR vs. optical comparison in Table 9, we note that the NIR maxima yield smaller intrinsic scatter $\sigma_{\rm int}$ and wRMS than B max *for all sub-*

Table 9. Optical - NIR intrinsic scatter

Optical BVR Method - NIR band(s)	$\Delta\sigma_{\rm int}$	n-σ	ΔwRMS	n-σ	ΔRMS	n-σ
SALT2 - Y	0.067 ± 0.029	2.3	0.073 ± 0.025	2.9	0.068 ± 0.026	2.6
SNooPy - Y	0.062 ± 0.027	2.3	0.057 ± 0.024	2.4	0.063 ± 0.028	2.2
SALT2 - J	0.027 ± 0.028	1.0	0.038 ± 0.026	1.5	0.040 ± 0.024	1.6
SNooPy - J	0.021 ± 0.025	0.8	0.023 ± 0.025	0.9	0.035 ± 0.027	1.3
SALT2 - H	0.101 ± 0.035	2.9	0.079 ± 0.022	3.6	0.065 ± 0.023	2.8
SNooPy - H	0.095 ± 0.033	2.9	0.063 ± 0.021	3.0	0.060 ± 0.026	2.3
SALT2 - K_s	0.040 ± 0.058	0.7	0.011 ± 0.039	0.3	0.000 ± 0.035	0.0
SNooPy - K_s	0.034 ± 0.057	0.6	-0.005 ± 0.038	-0.1	-0.005 ± 0.036	-0.1
SALT2 - any $YJHK_s$	0.086 ± 0.028	3.0	0.074 ± 0.024	3.2	0.062 ± 0.023	2.7
SNooPy - any $YJHK_s$	0.080 ± 0.026	3.1	0.059 ± 0.023	2.6	0.057 ± 0.025	2.3
SALT2 - JH	0.095 ± 0.032	2.9	0.078 ± 0.023	3.5	0.065 ± 0.024	2.7
SNooPy - JH	0.089 ± 0.030	2.9	0.062 ± 0.022	2.8	0.060 ± 0.026	2.3
SALT2 - YJH	0.089 ± 0.036	2.5	0.086 ± 0.024	3.5	0.092 ± 0.022	4.1
SNooPy - YJH	0.084 ± 0.034	2.5	0.070 ± 0.024	3.0	0.087 ± 0.025	3.5

NOTE— We show $\Delta\sigma_{\rm int}$, ΔwRMS, and ΔRMS, where the first is defined as the difference in Hubble residuals intrinsic scatter between the optical BVR data, fit using SALT2 or SNooPy, and the indicated subset of NIR data using the Gaussian process method at NIR max. The quantities ΔwRMS and ΔRMS are defined in a similar way to $\Delta\sigma_{\rm int}$ but using wRMS and RMS instead of the intrinsic scatter, respectively. The uncertainties are given by the quadrature sum of the $\sigma_{\rm int}$, wRMS, or RMS, uncertainties from columns 4, 6, or 7, respectively of Tables 7 and 8 for $\sigma_{\rm pec} = 150$ km/s. Columns 3, 5, and 6, show n-σ defined as the number n of standard deviations σ by which the NIR data yields *smaller* $\sigma_{\rm int}$, wRMS, or RMS, than the optical data using these methods, respectively. Excluding the K_s-band on its own, where our LC compilation contains much less data than the YJH bands, in general, NIR data subsets yield smaller RMS than the optical data at the ~ 1.3-4.1σ level. In the best case, the JH, YJH, and $YJHK_s$-bands perform ~ 2.3-4.1σ better than either SALT2 or SNooPy fits to the BVR data in terms of the RMS, while in the worst case, J-band, still performs 1.3σ better than optical data. For simplicity, the stated uncertainties on the difference in dispersion estimates between any two methods ignores the fact that the actual peculiar velocity-distance errors are exactly the same between the optical and NIR samples, since they contain exactly the same SN. The effect of accounting for this correlation is to decrease the uncertainty of the difference, and increase the significance (§5).

Table 10. GP Method intrinsic scatter for B max vs. NIR max

NIR band(s)	$\Delta\sigma_{\rm int}$	n-σ	ΔwRMS	n-σ	ΔRMS	n-σ
Y	0.014 ± 0.028	0.49	0.009 ± 0.020	0.42	0.007 ± 0.025	0.26
J	0.018 ± 0.025	0.70	0.017 ± 0.026	0.65	0.012 ± 0.026	0.46
H	0.031 ± 0.034	0.92	0.016 ± 0.014	1.12	0.006 ± 0.020	0.32
K_s	0.001 ± 0.076	0.01	-0.001 ± 0.048	-0.03	-0.009 ± 0.040	-0.23
any $YJHK_s$	0.019 ± 0.024	0.77	0.006 ± 0.016	0.38	-0.002 ± 0.018	-0.10
JH	0.030 ± 0.031	0.99	0.016 ± 0.018	0.89	0.004 ± 0.021	0.17
YJH	0.024 ± 0.037	0.66	0.008 ± 0.020	0.41	0.011 ± 0.019	0.58

NOTE— Similar to Table 9, we show $\Delta\sigma_{\rm int}$, ΔwRMS, and ΔRMS, defined here as the difference in Hubble residuals scatter between the Gaussian process method referenced to B max or NIR max. As in Table 9, the uncertainties are given by the quadrature sum of the $\sigma_{\rm int}$ or wRMS uncertainties from columns 4 or 6 of Tables 7 and 8 for $\sigma_{\rm pec} = 150$ km/s. Columns 3, 5, and 7, show n-σ defined as the number n of standard deviations σ by which the NIR data referenced to NIR max yields *smaller* intrinsic scatter, wRMS, or RMS, than when referenced to B-max, respectively. For every individual band and subset of NIR bands, the GP method yields smaller estimated intrinsic scatter when referencing to NIR max instead of B max, where the largest difference is n-$\sigma = 0.99\sigma$ for JH band. This trend is also observed when comparing the wRMS values, again, excluding, K_s band, where our sample lacks enough data to draw meaningful conclusions.

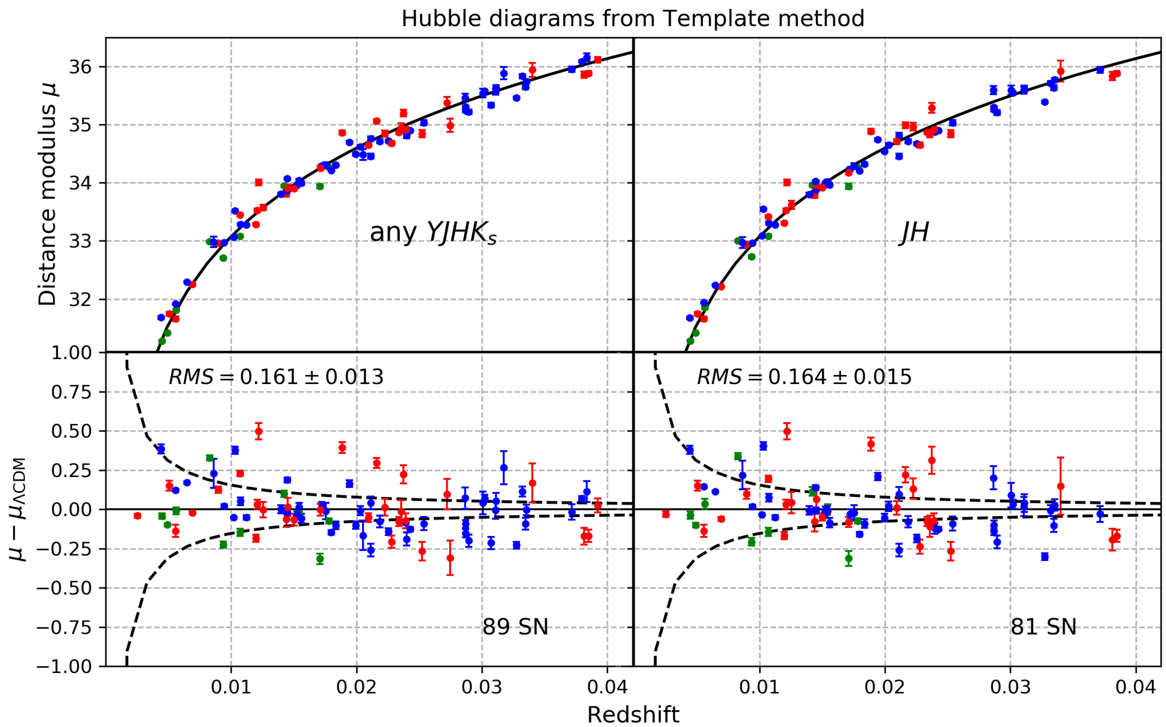

Figure 5. $YJHK_s$ Hubble diagrams (top row) and residuals (bottom row) using the template method on the 89 supernovae that passed our cuts. The error bars plotted for each supernova correspond to the fitting uncertainties $\hat{\sigma}_{\mathrm{fit},s}$. The left panel corresponds to the case when we determine a single distance modulus by combining any of the available 1, 2, 3, or 4 $YJHK_s$ distance moduli for a given SN Ia. The right panel shows the case when we require only SN Ia with J and H-band data, which allows us to include the majority of data from the CfA and CSP samples. Points are color coded by NIR photometric data source, including the CfA (red; Wood-Vasey et al. 2008; Friedman et al. 2015), the CSP (blue; Krisciunas et al. 2017), and other data from the literature (green; see Table 2 and references therein). Note that only the CSP used a Y-band filter. Table 8 summarizes the intrinsic scatter in the Hubble diagrams, while Table 11 reports the numerical values of the distance moduli from this figure.

Table 11. SN Ia $YJHK_s$ Distance Moduli from Template method

SN name	Source	$\hat{\mu}^{\mathrm{Y}}$ (mag)	$\hat{\mu}^{\mathrm{J}}$ (mag)	$\hat{\mu}^{\mathrm{H}}$ (mag)	$\hat{\mu}^{\mathrm{K}}$ (mag)	$\hat{\mu}$ (mag)
SN1998bu	CfA	...	30.11 ± 0.03	30.02 ± 0.02	29.97 ± 0.01	30.03 ± 0.013
SN1999ee	CSP	...	33.30 ± 0.02	33.27 ± 0.02	...	33.28 ± 0.016
SN1999ek	Others	...	34.27 ± 0.02	34.27 ± 0.02	...	34.27 ± 0.016
SN2000bh	CSP	34.83 ± 0.07	35.00 ± 0.06	34.83 ± 0.04	...	34.81 ± 0.041
SN2000ca	CSP	...	34.87 ± 0.02	34.92 ± 0.02	...	34.91 ± 0.016
SN2000E	Others	...	31.72 ± 0.04	31.91 ± 0.04	31.78 ± 0.04	31.81 ± 0.022
SN2001ba	CSP	...	35.56 ± 0.04	35.54 ± 0.04	35.66 ± 0.04	35.58 ± 0.023
SN2001bt	Others	...	33.94 ± 0.04	33.97 ± 0.03	33.92 ± 0.03	33.94 ± 0.021
SN2001cn	Others	...	34.06 ± 0.06	34.00 ± 0.06	33.95 ± 0.09	34.00 ± 0.039
SN2001cz	Others	...	33.88 ± 0.04	33.96 ± 0.06	33.96 ± 0.07	33.94 ± 0.034
SN2001el	Others	...	31.32 ± 0.03	31.27 ± 0.03	31.24 ± 0.03	31.28 ± 0.017
SN2002dj	Others	...	32.99 ± 0.03	33.00 ± 0.03	32.97 ± 0.03	32.99 ± 0.015
SN2003du	Others	...	32.64 ± 0.04	32.76 ± 0.03	32.72 ± 0.03	32.71 ± 0.020
SN2003hv	Others	...	31.38 ± 0.02	31.43 ± 0.02	31.45 ± 0.02	31.42 ± 0.011
SN2004ef	CSP	35.54 ± 0.07	35.66 ± 0.12	35.56 ± 0.10	...	35.54 ± 0.073
SN2004eo	CSP	33.91 ± 0.01	33.95 ± 0.01	33.98 ± 0.02	...	33.95 ± 0.013
SN2004ey	CSP	34.01 ± 0.02	33.95 ± 0.03	34.04 ± 0.04	...	34.04 ± 0.026
SN2004gs	CSP	35.36 ± 0.07	35.65 ± 0.10	35.57 ± 0.09	...	35.47 ± 0.068
SN2004S	Others	...	33.05 ± 0.04	33.10 ± 0.03	33.10 ± 0.05	33.08 ± 0.023
SN2005bo	CfA	...	33.77 ± 0.11	33.81 ± 0.08	33.87 ± 0.06	33.81 ± 0.050
SN2005cf	CfA	...	32.22 ± 0.02	32.21 ± 0.02	32.34 ± 0.01	32.25 ± 0.009
SN2005el	CSP	33.95 ± 0.02	34.02 ± 0.03	33.99 ± 0.03	...	33.97 ± 0.020
SN2005iq	CSP	35.69 ± 0.02	35.76 ± 0.03	35.78 ± 0.05	...	35.74 ± 0.033
SN2005kc	CSP	33.86 ± 0.02	33.88 ± 0.03	33.88 ± 0.02	...	33.87 ± 0.019
SN2005ki	CSP	34.58 ± 0.02	34.64 ± 0.03	34.65 ± 0.04	...	34.62 ± 0.029
SN2005lu	CSP	35.89 ± 0.11	...	...	...	35.89 ± 0.106
SN2005na	CfA	...	35.31 ± 0.13	...	35.48 ± 0.15	35.38 ± 0.097
SN2006ac	CfA	...	35.20 ± 0.08	35.32 ± 0.12	35.03 ± 0.09	35.20 ± 0.059
SN2006ax	CSP	34.18 ± 0.01	34.15 ± 0.02	34.23 ± 0.02	...	34.22 ± 0.014
SN2006bh	CSP	33.27 ± 0.03	33.32 ± 0.04	33.31 ± 0.03	...	33.29 ± 0.025
SN2006bt	CSP	...	35.33 ± 0.04	...	...	35.33 ± 0.039
SN2006cp	CfA	...	35.12 ± 0.11	34.90 ± 0.08	34.47 ± 0.10	34.85 ± 0.054
SN2006D	CfA	...	32.93 ± 0.03	32.94 ± 0.04	33.03 ± 0.04	32.97 ± 0.021
SN2006ej	CSP	34.42 ± 0.14	34.60 ± 0.09	...	...	34.49 ± 0.094
SN2006kf	CSP	34.65 ± 0.02	34.75 ± 0.02	34.74 ± 0.03	...	34.70 ± 0.022
SN2006lf	CfA	...	33.48 ± 0.03	33.54 ± 0.04	...	33.53 ± 0.030
SN2006N	CfA	...	34.05 ± 0.11	33.92 ± 0.09	33.74 ± 0.09	33.91 ± 0.058
SN2007A	CSP	34.30 ± 0.02	34.18 ± 0.05	34.26 ± 0.04	...	34.29 ± 0.029
SN2007af	CSP	31.91 ± 0.01	31.96 ± 0.01	31.93 ± 0.01	...	31.92 ± 0.009
SN2007ai	CSP	35.57 ± 0.02	35.42 ± 0.03	35.38 ± 0.03	...	35.46 ± 0.022
SN2007as	CSP	34.26 ± 0.02	34.27 ± 0.02	34.34 ± 0.04	...	34.31 ± 0.025
SN2007bc	CSP	34.68 ± 0.03	34.80 ± 0.04	34.82 ± 0.06	...	34.76 ± 0.042
SN2007bd	CSP	35.54 ± 0.03	35.58 ± 0.04	35.60 ± 0.08	...	35.57 ± 0.057
SN2007ca	CSP	34.17 ± 0.01	34.07 ± 0.01	34.01 ± 0.02	...	34.07 ± 0.016
SN2007co	CfA	...	...	...	34.99 ± 0.11	34.99 ± 0.110
SN2007cq	CfA	...	34.87 ± 0.03	34.84 ± 0.08	...	34.85 ± 0.060
SN2007jg	CSP	36.05 ± 0.02	36.16 ± 0.02	...	...	36.09 ± 0.014
SN2007le	CSP	32.36 ± 0.01	32.24 ± 0.01	32.24 ± 0.01	...	32.29 ± 0.007
SN2007qe	CfA	...	34.70 ± 0.17	34.91 ± 0.07	35.26 ± 0.15	34.95 ± 0.075
SN2007sr	CSP	31.68 ± 0.05	31.67 ± 0.06	31.68 ± 0.03	...	31.68 ± 0.029
SN2007st	CSP	...	34.22 ± 0.09	34.55 ± 0.04	...	34.46 ± 0.041
SN2008af	CfA	...	35.98 ± 0.19	35.90 ± 0.24	35.96 ± 0.18	35.94 ± 0.124
SN2008ar	CSP	35.30 ± 0.02	35.30 ± 0.04	35.17 ± 0.06	...	35.22 ± 0.038
SN2008bc	CSP	34.07 ± 0.02	34.02 ± 0.04	33.95 ± 0.04	...	34.00 ± 0.029
SN2008bf	CSP	34.96 ± 0.01	34.95 ± 0.01	35.07 ± 0.06	...	35.03 ± 0.042
SN2008C	CSP	34.27 ± 0.08	34.24 ± 0.09	34.31 ± 0.06	...	34.30 ± 0.053
SN2008fl	CSP	34.42 ± 0.03	34.52 ± 0.05	34.55 ± 0.03	...	34.49 ± 0.024
SN2008fr	CSP	36.11 ± 0.06	36.23 ± 0.14	...	...	36.16 ± 0.067
SN2008fw	CSP	33.07 ± 0.11	33.06 ± 0.14	32.94 ± 0.12	...	32.98 ± 0.091
SN2008gb	CfA	...	35.98 ± 0.08	35.78 ± 0.09	35.83 ± 0.11	35.86 ± 0.053
SN2008gg	CSP	35.63 ± 0.05	35.60 ± 0.10	35.63 ± 0.07	...	35.63 ± 0.051
SN2008gl	CSP	35.97 ± 0.02	35.70 ± 0.03	35.72 ± 0.05	...	35.83 ± 0.033
SN2008gp	CSP	35.55 ± 0.02	35.50 ± 0.03	35.69 ± 0.06	...	35.65 ± 0.038
SN2008hj	CSP	36.03 ± 0.05	36.02 ± 0.07	35.91 ± 0.07	...	35.95 ± 0.049
SN2008hm	CfA	...	34.59 ± 0.02	34.76 ± 0.06	34.57 ± 0.04	34.65 ± 0.027
SN2008hs	CfA	...	34.86 ± 0.06	34.90 ± 0.06	34.82 ± 0.07	34.86 ± 0.035
SN2008hv	CSP	33.80 ± 0.02	33.78 ± 0.02	33.81 ± 0.04	...	33.81 ± 0.026
SN2008ia	CSP	34.80 ± 0.02	34.72 ± 0.03	34.66 ± 0.03	...	34.72 ± 0.022
SN2009aa	CSP	35.23 ± 0.03	35.27 ± 0.04	35.25 ± 0.03	...	35.24 ± 0.026
SN2009ab	CSP	33.46 ± 0.02	33.51 ± 0.03	33.56 ± 0.03	...	33.52 ± 0.023
SN2009ad	CSP	35.24 ± 0.01	35.21 ± 0.02	35.33 ± 0.04	...	35.30 ± 0.025
SN2009ag	CSP	33.06 ± 0.00	33.11 ± 0.01	33.08 ± 0.01	...	33.07 ± 0.005
SN2009al	CfA	...	34.92 ± 0.05	34.84 ± 0.03	...	34.87 ± 0.028
SN2009an	CfA	...	33.46 ± 0.03	33.40 ± 0.03	33.51 ± 0.04	33.45 ± 0.017
SN2009bv	CfA	...	36.03 ± 0.05	35.82 ± 0.05	...	35.88 ± 0.040
SN2009cz	CSP	34.69 ± 0.05	34.68 ± 0.06	34.73 ± 0.04	...	34.71 ± 0.037
SN2009D	CSP	34.90 ± 0.02	34.90 ± 0.01	34.90 ± 0.02	...	34.90 ± 0.014
SN2009kk	CfA	...	33.92 ± 0.05	34.04 ± 0.07	...	34.01 ± 0.051
SN2009kq	CfA	...	33.53 ± 0.09	33.65 ± 0.09	33.52 ± 0.06	33.57 ± 0.048
SN2009Y	CSP	32.97 ± 0.01	32.96 ± 0.02	32.97 ± 0.01	...	32.97 ± 0.011
SN2010ai	CfA	...	35.04 ± 0.03	34.87 ± 0.06	...	34.92 ± 0.047
SN2010dw	CfA	...	36.12 ± 0.04	...	...	36.12 ± 0.045
SN2010iw	CfA	...	34.70 ± 0.04	34.63 ± 0.06	34.73 ± 0.10	34.68 ± 0.039
SN2010kg	CfA	...	34.24 ± 0.04	34.14 ± 0.04	34.40 ± 0.11	34.25 ± 0.037
SN2011ao	CfA	...	33.35 ± 0.03	33.29 ± 0.03	33.22 ± 0.06	33.29 ± 0.023
SN2011B	CfA	...	31.62 ± 0.07	31.68 ± 0.05	...	31.66 ± 0.038
SN2011by	CfA	...	31.76 ± 0.06	31.74 ± 0.04	...	31.75 ± 0.032
SN2011df	CfA	...	33.97 ± 0.01	33.90 ± 0.03	33.83 ± 0.12	33.90 ± 0.037
SNf20080514-002	CfA	...	35.03 ± 0.04	34.97 ± 0.07	35.23 ± 0.05	35.07 ± 0.032

NOTE— Distance moduli and their fitting uncertainties $\hat{\sigma}_{\mathrm{fit},s}$, estimated from the different NIR bands, either alone (see columns 3-6) or combined (column 7), using the template method. Corresponding Hubble diagrams are shown in Figs. 5 and 11.

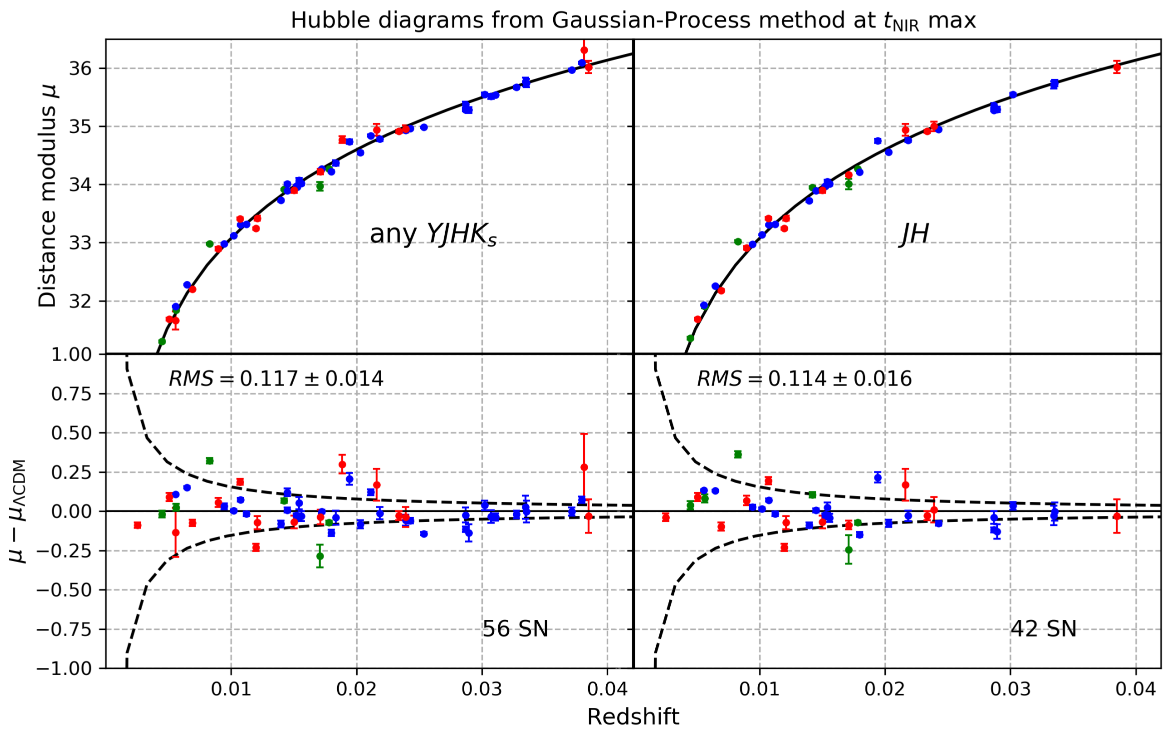

Figure 6. Similar to Fig. 5, but for $YJHK_s$ Hubble diagrams (top row) and residuals (bottom row) using the GP method at NIR max. Again, Tables 7 and 8 summarize the intrinsic scatter in the Hubble diagrams, while Table 12 lists numerical values of the distance moduli from this figure.

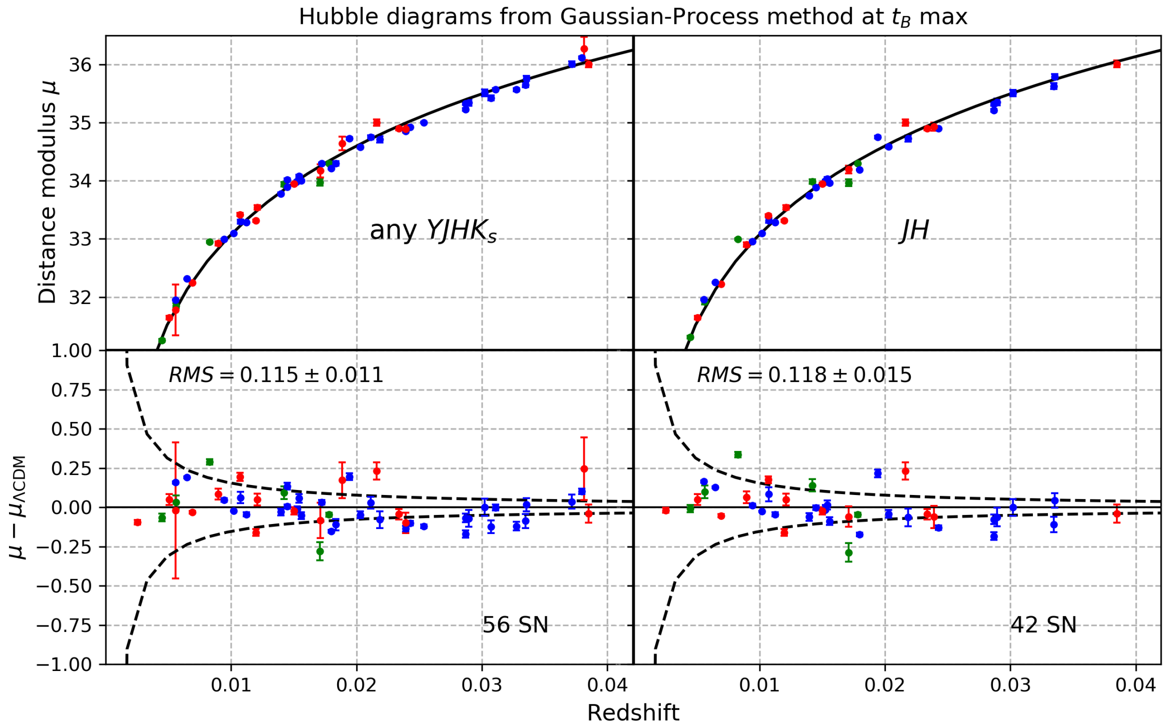

Figure 7. Similar to Fig. 6, but for $YJHK_s$ Hubble diagrams (top row) and residuals (bottom row) using the Gaussian-process method at B max. Again, Tables 7 and 8 summarizes the intrinsic scatter in the Hubble diagram while Table 13 shows numerical values of the distance moduli from this figure.

sets of the NIR data except for K_s.[8] While NIR data at NIR max are *better* standard candles in comparison to optical data, they are also *at least as good or better* than when referenced to B-max. Therefore, future analyses should consider using t_{NIRmax} as the reference time instead of the traditional $t_{B\mathrm{max},s}$.

As an additional comparison between NIR and optical Hubble residuals, in Fig. 10, we plot the histograms (dashed lines) with their Gaussian approximation (left panel), and the cumulative distribution function (right panel) for Hubble residuals using the same 56 SN Ia used for the "any $YJHK_s$" GP method at NIR max (lower left panel on Fig. 6), SALT2 (lower left panel of Fig. 9), and SNooPy (lower right panel of Fig. 9). The Gaussian approximations of the histograms in the left panel of Fig. 10 show that the Hubble residuals are more narrowly distributed for the NIR data (solid red curve) compared to both optical methods (solid green and blue), while in the right panel of Fig. 10 the cumulative distribution function curve for the NIR Hubble residuals is steeper than for either optical curve. Both approaches suggest that the Hubble residual scatter is smaller in the NIR compared to the optical. A larger sample of SN Ia in the NIR would strengthen the evidence for this conclusion.

[8] The only exception we tested is the K_s-band, which has only 14 SN Ia LCs, where we find an essentially equivalent wRMS $\sim$ 0.163 mag when referenced to either NIR max or B-max.

6. CONCLUSIONS

This work bolsters and confirms a growing body of evidence that SN Ia in NIR are excellent standard candles in the $YJHK_s$ bands in comparison to the optical BVR bands. Depending on the NIR data subset, our GP method performs 2.3-2.7σ better in RMS than either the SALT2 or SNooPy LC fitters for the same 56 SN Ia using BVR data and applying LC shape and color corrections. Using a suitable subset of the existing low-redshift sample including 89 spectroscopically normal SN Ia with NIR data, $YJHK_s$ photometry alone already provides a simple means to estimate accurate and precise host galaxy distances in each band, without the LC shape or host galaxy dust reddening corrections required for optical data.

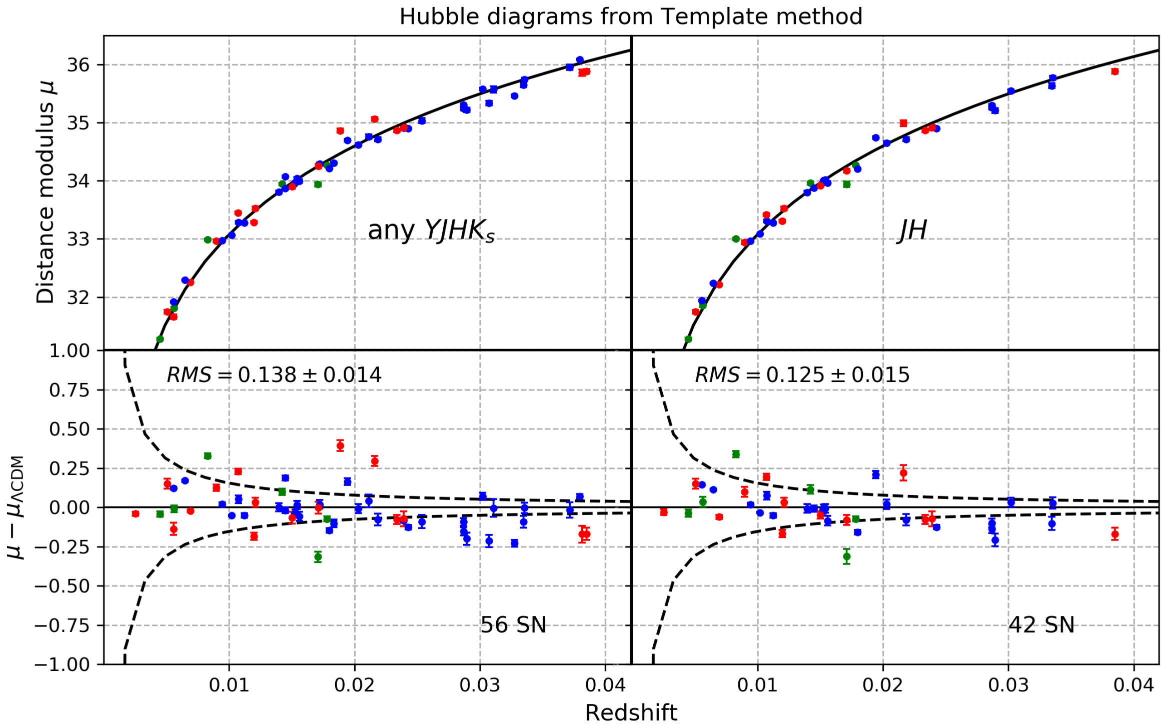

Figure 8. Similar to Fig. 5 but applying the template method to exactly same 56 supernovae shown in Fig. 6 and 7. Again, Table 7 summarizes the intrinsic scatter in the Hubble diagram while Table 11 shows numerical values of the distance moduli from this figure.

In this work, we employed a hierarchical Bayesian model, combined with a Gaussian process LC fitter, to construct new mean NIR LC templates. We then used these templates, along with Milky Way dust corrections, NIR K-corrections, and the measured spectroscopic redshifts (corrected for local velocity flows), and redshift independent distance information (e.g. Cepheids) for special cases, to estimate host galaxy distances and uncertainties and construct Hubble diagrams in each of the individual $YJHK_s$ bands. When considering NIR-only methods, our GP method referenced to the time of NIR maximum yields slight smaller Hubble diagram intrinsic scatter and error weighted RMS than when referenced to B max and significantly smaller intrinsic scatter compared to the template method.

Our approach is intermediate in complexity between earlier analyses by our group by Wood-Vasey et al. 2008 and the BayeSN approach detailed in Mandel et al. 2009, 2011. The BayeSN methodology presents a coherent, principled, hierarchical Bayesian model that takes into account the full correlation structure between all the input optical and NIR bandpasses, both in color and phase, in order to determine the posterior distributions for distance moduli μ, host galaxy dust estimates A_V, and separate R_V values for each supernova. Nevertheless, BayeSN is considerably more complex to implement than the simpler analysis methods in this work, which perform quite well for our sample of NIR data.

Compared to optical LCs, NIR SN Ia LCs have a narrow luminosity distribution, and are less sensitive to host galaxy dust extinction. This could help to limit systematic galaxy distance errors that arise from the degeneracy between the intrinsic supernova colors and reddening of light by dust, that affects optical-only SN Ia cosmology (Krisciunas et al. 2004a; Wood-Vasey et al. 2008; Folatelli et al. 2010; Burns et al. 2011; Burns et al. 2014; Kattner et al. 2012; Mandel et al. 2009, 2011, 2017; Scolnic et al. 2014b, 2017). Studies combining NIR and optical SN Ia photometry have already shown that the addition of NIR data is an extremely promising way to break the degeneracy between intrinsic color and dust reddening, allowing distance estimates to become increasingly insensitive to the assumptions behind individual LC fitting models (Mandel et al. 2011, 2014).

We have recently begun to augment the existing low-z SN Ia in NIR sample from the CfA, CSP, and other

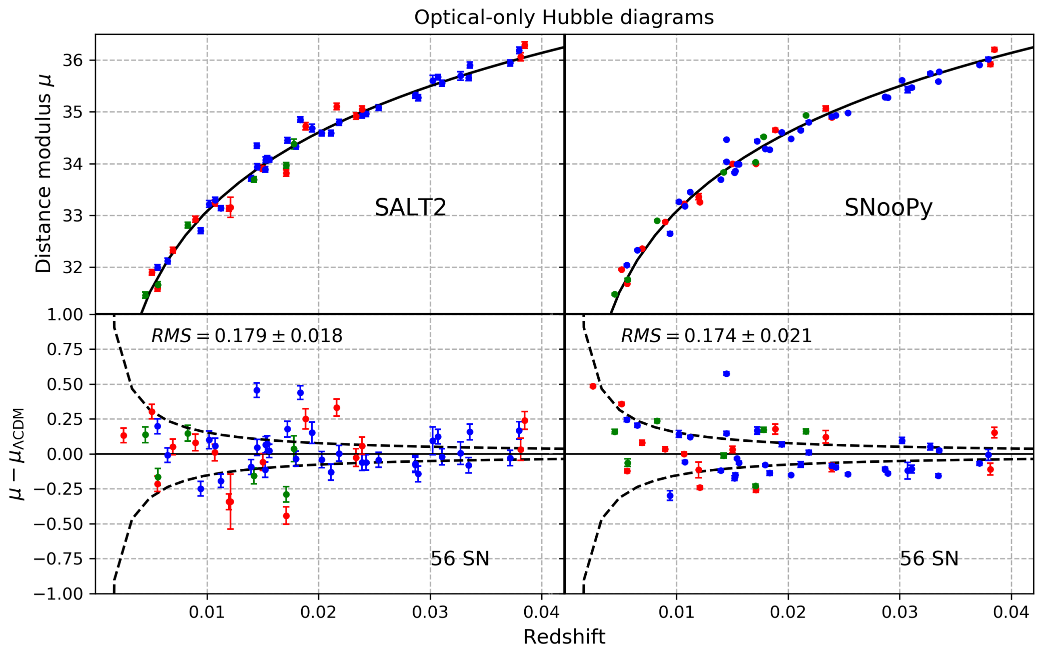

Figure 9. Hubble diagram (top row) and residuals (bottom row) using SALT2 and SNooPy to fit only the *optical* BVR-band LCs for exactly same sample of 56 SN Ia used for the "any $YJHK_s$ " GP (NIR max) Hubble diagram shown in the left panel of Fig. 6 and listed in Table 12. As emphasized in Tables 7-9, the intrinsic scatter is clearly larger in these optical only Hubble diagrams compared with the GP NIR max ones constructed for the same 56 SN Ia. Table 14 shows numerical values of the distance moduli from this figure.

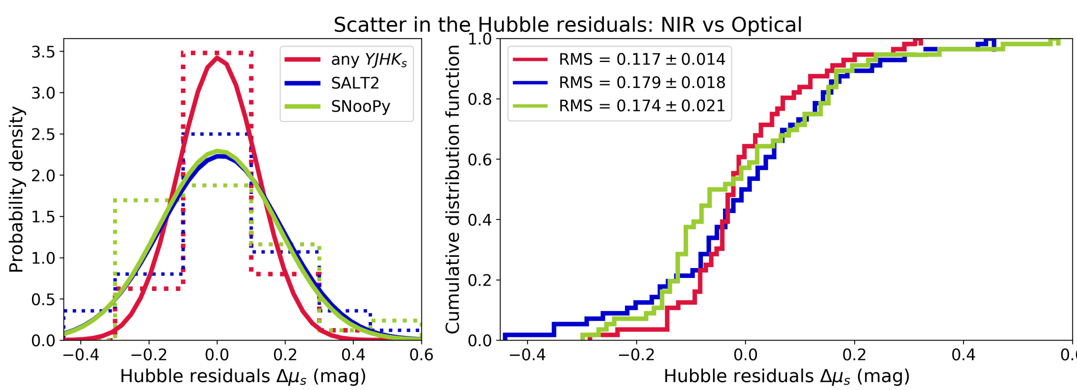

Figure 10. Comparing the scatter in the Hubble residuals, $\{\Delta\mu_s\}$, as defined in Eq. (21), using NIR and optical methods for the same 56 SN Ia. The red, green, and blue colors correspond to the Hubble residuals from the "any $YJHK_s$" GP (NIR max) method (lower left panel of Fig. 6), SALT2 (lower left panel of Fig. 9), and SNooPy (lower right panel of Fig. 9), respectively. The left panel shows histograms (dashed lines) and Gaussian approximation to the histograms (solid lines) of the Hubble residuals, where we observe that the distribution of the NIR Hubble residuals (red) is *narrower* than either optical distribution (blue or green). The right panel shows the corresponding cumulative probability distribution functions, where we also note that the slope of the NIR curve is *steeper* than the optical curves, asymptotic to 1 at a smaller value of $\Delta\mu$, again indicating that the Hubble residual scatter is smaller in the NIR compared to the optical.

Table 12. SN Ia $YJHK_s$ Distance Moduli from Gaussian-process Method at NIR max

SN name	Source	$\hat{\mu}^{\mathrm{Y}}$ (mag)	$\hat{\mu}^{\mathrm{J}}$ (mag)	$\hat{\mu}^{\mathrm{H}}$ (mag)	$\hat{\mu}^{\mathrm{K}}$ (mag)	$\hat{\mu}$ (mag)
SN1998bu	CfA	...	30.09 ± 0.03	30.03 ± 0.03	29.87 ± 0.02	29.99 ± 0.018
SN1999ee	CSP	...	33.30 ± 0.02	33.32 ± 0.02	...	33.32 ± 0.016
SN1999ek	Others	...	34.24 ± 0.02	34.28 ± 0.02	...	34.27 ± 0.014
SN2000ca	CSP	...	34.94 ± 0.03	...	...	34.94 ± 0.034
SN2000E	Others	...	31.72 ± 0.02	31.93 ± 0.03	31.71 ± 0.04	31.84 ± 0.022
SN2001ba	CSP	...	35.55 ± 0.02	35.55 ± 0.03	35.56 ± 0.08	35.55 ± 0.031
SN2001bt	Others	...	33.91 ± 0.03	33.96 ± 0.02	33.83 ± 0.03	33.91 ± 0.014
SN2001cz	Others	...	33.90 ± 0.05	34.03 ± 0.11	33.87 ± 0.11	33.97 ± 0.072
SN2001el	Others	...	31.45 ± 0.02	31.34 ± 0.03	31.17 ± 0.04	31.30 ± 0.022
SN2002dj	Others	...	33.01 ± 0.03	33.03 ± 0.02	32.89 ± 0.03	32.98 ± 0.017
SN2004eo	CSP	33.97 ± 0.01	33.97 ± 0.01	33.97 ± 0.01	...	33.97 ± 0.011
SN2004ey	CSP	34.03 ± 0.01	33.96 ± 0.01	34.06 ± 0.04	...	34.08 ± 0.038
SN2005cf	CfA	...	32.21 ± 0.06	32.17 ± 0.03	32.25 ± 0.03	32.20 ± 0.020
SN2005el	CSP	33.88 ± 0.01	33.95 ± 0.01	33.97 ± 0.01	...	33.96 ± 0.013
SN2005iq	CSP	35.76 ± 0.03	35.75 ± 0.04	35.74 ± 0.07	...	35.74 ± 0.069
SN2005kc	CSP	33.92 ± 0.01	33.90 ± 0.01	33.89 ± 0.02	...	33.90 ± 0.015
SN2005ki	CSP	34.58 ± 0.01	34.59 ± 0.01	34.55 ± 0.03	...	34.55 ± 0.027
SN2006ax	CSP	34.17 ± 0.01	34.16 ± 0.01	34.22 ± 0.02	...	34.22 ± 0.019
SN2006bh	CSP	33.31 ± 0.01	33.30 ± 0.01	33.31 ± 0.01	...	33.31 ± 0.012
SN2006bt	CSP	...	35.51 ± 0.04	...	...	35.51 ± 0.041
SN2006D	CfA	...	32.85 ± 0.02	32.92 ± 0.04	32.86 ± 0.06	32.90 ± 0.029
SN2006kf	CSP	34.73 ± 0.01	34.77 ± 0.01	34.75 ± 0.04	...	34.74 ± 0.039
SN2006lf	CfA	...	33.40 ± 0.03	33.42 ± 0.05	...	33.42 ± 0.043
SN2007A	CSP	34.26 ± 0.01	34.17 ± 0.02	...	...	34.27 ± 0.012
SN2007af	CSP	31.92 ± 0.01	32.00 ± 0.00	31.92 ± 0.01	...	31.90 ± 0.007
SN2007ai	CSP	35.67 ± 0.02	...	...	...	35.67 ± 0.025
SN2007as	CSP	...	...	34.37 ± 0.04	...	34.37 ± 0.044
SN2007bc	CSP	...	34.84 ± 0.02	...	...	34.84 ± 0.019
SN2007bd	CSP	35.54 ± 0.02	35.56 ± 0.04	...	...	35.54 ± 0.023
SN2007ca	CSP	...	...	34.01 ± 0.03	...	34.01 ± 0.025
SN2007jg	CSP	36.09 ± 0.02	36.11 ± 0.02	...	...	36.09 ± 0.021
SN2007le	CSP	32.33 ± 0.01	32.23 ± 0.01	32.26 ± 0.01	...	32.28 ± 0.006
SN2008ar	CSP	35.33 ± 0.01	35.34 ± 0.03	35.28 ± 0.05	...	35.28 ± 0.054
SN2008bc	CSP	34.02 ± 0.01	33.98 ± 0.02	34.01 ± 0.03	...	34.02 ± 0.031
SN2008bf	CSP	34.98 ± 0.01	34.87 ± 0.01	...	...	34.98 ± 0.010
SN2008gb	CfA	...	...	...	36.31 ± 0.21	36.31 ± 0.211
SN2008gp	CSP	35.63 ± 0.03	35.53 ± 0.05	35.75 ± 0.07	...	35.76 ± 0.074
SN2008hj	CSP	35.98 ± 0.02	36.08 ± 0.04	...	...	35.97 ± 0.026
SN2008hs	CfA	...	34.86 ± 0.05	...	34.67 ± 0.11	34.77 ± 0.059
SN2008hv	CSP	33.77 ± 0.00	33.72 ± 0.01	33.72 ± 0.02	...	33.73 ± 0.022
SN2009aa	CSP	35.31 ± 0.01	35.28 ± 0.01	35.28 ± 0.02	...	35.28 ± 0.018
SN2009ad	CSP	35.27 ± 0.01	35.27 ± 0.02	35.37 ± 0.05	...	35.37 ± 0.048
SN2009ag	CSP	33.20 ± 0.01	33.20 ± 0.01	33.12 ± 0.01	...	33.12 ± 0.009
SN2009al	CfA	...	35.07 ± 0.02	34.88 ± 0.03	...	34.91 ± 0.029
SN2009an	CfA	...	33.40 ± 0.02	33.42 ± 0.03	33.39 ± 0.03	33.41 ± 0.019
SN2009bv	CfA	...	36.07 ± 0.04	36.01 ± 0.13	...	36.02 ± 0.108
SN2009cz	CSP	34.77 ± 0.01	34.72 ± 0.02	34.77 ± 0.04	...	34.78 ± 0.038
SN2009D	CSP	34.98 ± 0.01	34.91 ± 0.01	34.95 ± 0.02	...	34.97 ± 0.018
SN2009Y	CSP	33.02 ± 0.01	32.98 ± 0.01	32.97 ± 0.02	...	32.98 ± 0.018
SN2010ai	CfA	...	35.05 ± 0.05	34.99 ± 0.10	34.85 ± 0.09	34.95 ± 0.063
SN2010kg	CfA	...	34.22 ± 0.03	34.16 ± 0.03	34.33 ± 0.14	34.22 ± 0.047
SN2011ao	CfA	...	33.33 ± 0.05	33.23 ± 0.03	...	33.24 ± 0.023
SN2011B	CfA	...	31.66 ± 0.16	...	...	31.66 ± 0.156
SN2011by	CfA	...	31.71 ± 0.05	31.68 ± 0.03	...	31.69 ± 0.026
SN2011df	CfA	...	33.94 ± 0.03	33.89 ± 0.05	...	33.90 ± 0.041
SNf20080514-002	CfA	...	35.03 ± 0.14	34.92 ± 0.12	...	34.94 ± 0.101

Note— Distance moduli and their fitting uncertainties $\hat{\sigma}_{\mathrm{fit},s}$, estimated from the different NIR bands, either alone (see columns 3-6) or combined (column 7) using the Gaussian-process method at NIR max. The Hubble diagrams from these data are shown in Figs. 6 and 12.

Table 13. SN Ia $YJHK_s$ Distance Moduli from Gaussian-process Method at B max

SN name	Source	$\hat{\mu}^{\mathrm{Y}}$ (mag)	$\hat{\mu}^{\mathrm{J}}$ (mag)	$\hat{\mu}^{\mathrm{H}}$ (mag)	$\hat{\mu}^{\mathrm{K}}$ (mag)	$\hat{\mu}$ (mag)
SN1998bu	CfA	...	30.11 ± 0.02	30.04 ± 0.02	29.90 ± 0.02	29.98 ± 0.014
SN1999ee	CSP	...	33.31 ± 0.02	33.28 ± 0.02	...	33.29 ± 0.013
SN1999ek	Others	...	34.26 ± 0.02	34.31 ± 0.02	...	34.30 ± 0.013
SN2000ca	CSP	...	34.86 ± 0.02	...	...	34.86 ± 0.019
SN2000E	Others	...	31.77 ± 0.04	31.96 ± 0.05	31.68 ± 0.06	31.85 ± 0.041
SN2001ba	CSP	...	35.43 ± 0.09	35.54 ± 0.07	35.47 ± 0.09	35.51 ± 0.055
SN2001bt	Others	...	33.86 ± 0.06	34.02 ± 0.05	33.81 ± 0.06	33.94 ± 0.039
SN2001cz	Others	...	33.81 ± 0.05	34.01 ± 0.07	33.90 ± 0.08	33.97 ± 0.058
SN2001el	Others	...	31.36 ± 0.02	31.30 ± 0.03	31.20 ± 0.04	31.25 ± 0.023
SN2002dj	Others	...	32.97 ± 0.02	33.00 ± 0.02	32.87 ± 0.03	32.95 ± 0.018
SN2004eo	CSP	33.96 ± 0.01	33.94 ± 0.01	33.99 ± 0.01	...	33.98 ± 0.009
SN2004ey	CSP	34.06 ± 0.02	33.92 ± 0.02	34.07 ± 0.04	...	34.08 ± 0.027
SN2005cf	CfA	...	32.23 ± 0.01	32.22 ± 0.01	32.28 ± 0.01	32.24 ± 0.009
SN2005el	CSP	33.96 ± 0.01	33.97 ± 0.02	34.01 ± 0.02	...	33.99 ± 0.017
SN2005iq	CSP	35.70 ± 0.02	35.76 ± 0.03	35.80 ± 0.06	...	35.76 ± 0.042
SN2005kc	CSP	33.90 ± 0.01	33.88 ± 0.02	33.89 ± 0.02	...	33.90 ± 0.013
SN2005ki	CSP	34.59 ± 0.02	34.61 ± 0.03	34.58 ± 0.03	...	34.58 ± 0.022
SN2006ax	CSP	34.20 ± 0.01	34.13 ± 0.01	34.21 ± 0.01	...	34.21 ± 0.010
SN2006bh	CSP	33.28 ± 0.03	33.34 ± 0.09	33.31 ± 0.05	...	33.30 ± 0.037
SN2006bt	CSP	...	35.43 ± 0.04	...	...	35.43 ± 0.041
SN2006D	CfA	...	32.89 ± 0.03	32.91 ± 0.05	32.94 ± 0.05	32.92 ± 0.035
SN2006kf	CSP	34.68 ± 0.01	34.73 ± 0.01	34.76 ± 0.03	...	34.73 ± 0.022
SN2006lf	CfA	...	33.45 ± 0.03	33.57 ± 0.05	...	33.54 ± 0.038
SN2007A	CSP	34.34 ± 0.01	34.19 ± 0.04	...	...	34.30 ± 0.015
SN2007af	CSP	31.95 ± 0.01	31.96 ± 0.01	31.96 ± 0.01	...	31.95 ± 0.007
SN2007ai	CSP	35.57 ± 0.03	...	...	...	35.57 ± 0.027
SN2007as	CSP	...	...	34.30 ± 0.04	...	34.30 ± 0.036
SN2007bc	CSP	...	34.75 ± 0.04	...	...	34.75 ± 0.037
SN2007bd	CSP	35.56 ± 0.02	35.60 ± 0.04	...	...	35.57 ± 0.020
SN2007ca	CSP	...	...	34.02 ± 0.02	...	34.02 ± 0.021
SN2007jg	CSP	36.08 ± 0.02	36.24 ± 0.03	...	...	36.12 ± 0.018
SN2007le	CSP	32.41 ± 0.01	32.24 ± 0.01	32.26 ± 0.01	...	32.32 ± 0.005
SN2008ar	CSP	35.37 ± 0.03	35.41 ± 0.05	35.34 ± 0.08	...	35.35 ± 0.053
SN2008bc	CSP	34.14 ± 0.02	34.08 ± 0.03	33.93 ± 0.03	...	34.00 ± 0.023
SN2008bf	CSP	35.01 ± 0.02	34.98 ± 0.02	...	...	35.00 ± 0.012
SN2008gb	CfA	...	...	...	36.28 ± 0.20	36.28 ± 0.200
SN2008gp	CSP	35.59 ± 0.01	35.50 ± 0.03	35.67 ± 0.06	...	35.65 ± 0.044
SN2008hj	CSP	35.99 ± 0.05	36.05 ± 0.10	...	...	36.01 ± 0.044
SN2008hs	CfA	...	34.96 ± 0.09	...	34.60 ± 0.13	34.64 ± 0.115
SN2008hv	CSP	33.88 ± 0.01	33.83 ± 0.02	33.72 ± 0.03	...	33.78 ± 0.022
SN2009aa	CSP	35.22 ± 0.02	35.18 ± 0.02	35.22 ± 0.03	...	35.23 ± 0.023
SN2009ad	CSP	35.28 ± 0.01	35.24 ± 0.02	35.35 ± 0.04	...	35.33 ± 0.027
SN2009ag	CSP	33.11 ± 0.00	33.12 ± 0.00	33.09 ± 0.00	...	33.10 ± 0.003
SN2009al	CfA	...	35.02 ± 0.04	34.86 ± 0.04	...	34.90 ± 0.033
SN2009an	CfA	...	33.48 ± 0.02	33.37 ± 0.03	33.49 ± 0.05	33.42 ± 0.026
SN2009bv	CfA	...	35.94 ± 0.08	36.03 ± 0.07	...	36.01 ± 0.058
SN2009cz	CSP	34.72 ± 0.08	34.77 ± 0.12	34.72 ± 0.06	...	34.71 ± 0.054
SN2009D	CSP	34.96 ± 0.02	34.90 ± 0.01	34.90 ± 0.02	...	34.92 ± 0.015
SN2009Y	CSP	33.01 ± 0.01	32.91 ± 0.02	32.98 ± 0.01	...	32.99 ± 0.011
SN2010ai	CfA	...	35.02 ± 0.03	34.91 ± 0.09	34.89 ± 0.08	34.89 ± 0.065
SN2010kg	CfA	...	34.42 ± 0.08	34.13 ± 0.08	34.26 ± 0.25	34.17 ± 0.113
SN2011ao	CfA	...	33.35 ± 0.03	33.30 ± 0.03	...	33.31 ± 0.022
SN2011B	CfA	...	31.78 ± 0.43	...	...	31.78 ± 0.434
SN2011by	CfA	...	31.67 ± 0.06	31.64 ± 0.04	...	31.65 ± 0.034
SN2011df	CfA	...	33.99 ± 0.01	33.93 ± 0.03	...	33.94 ± 0.022
SNf20080514-002	CfA	...	35.03 ± 0.04	34.99 ± 0.07	...	35.00 ± 0.054

NOTE— Same as Table 12 but using the Gaussian-process method at B max. The Hubble diagrams from these data are shown in Figs. 7 and 13.

groups using the Hubble Space Telescope RAISIN program in Cycles 20 and 23 (Kirshner 2012; Foley et al. 2013a,b; Kirshner & The RAISIN TEAM 2014). In RAISIN1, we observed 23 SN Ia at $z \sim 0.35$ in the rest-frame NIR with WFC3/IR, followed by observations of 24 additional SN Ia at $z \sim 0.5$ for RAISIN2. Each of these HST NIR observations was accompanied by well-sampled ground based optical photometry from Pan-STARRS (PS1; Rest et al. 2014; Jones et al. 2018; Scolnic et al. 2018) and the Dark Energy Survey (DES; Dark Energy Survey Collaboration et al. 2016; DES Collaboration et al. 2018c; Brout et al. 2018b). Analysis of the RAISIN data will be presented in future work.

The evidence from this work further emphasizes the promise of NIR wavelength observations not only for the ongoing HST RAISIN project, but also for future space studies of cosmic acceleration and dark energy (Gehrels 2010; Beaulieu et al. 2010; Astier et al. 2011; Hounsell et al. 2017; Riess et al. 2018c). Upcoming missions that could exploit nearby NIR data as a low-z anchor include the Large Synoptic Survey Telescope (LSST; Ivezic et al. 2008), the NASA Wide-Field Infrared Survey Telescope (WFIRST-AFTA; Gehrels 2010; Spergel et al. 2015), the European Space Agency's EUCLID mission (Beaulieu et al. 2010; Wallner et al. 2017), as well as the NASA James Webb Space Telescope (JWST; Clampin 2011; Greenhouse 2016).

NIR photometry can also augment our knowledge of the spectral energy distribution of SN Ia, for example the Type Ia parametrized SALT2 model, which is currently poorly constrained at infrared wavelengths (Pierel et al. 2018b,a). This will dovetail nicely with the NIR capabilities of JWST and WFIRST and be useful for future SN Ia surveys.

Methods such as BayeSN (Mandel et al. 2009, 2011), SNooPy, and SALT2ext (Pierel et al. 2018b,a) that use empirical LC fitters and provide host galaxy distance estimates using both optical and NIR data can be extended to obtain cosmological inferences and dark energy constraints using both low-z and high-z samples.

Table 14. SN Ia distance moduli from the optical BVR bands

SN name	Source	SALT2 (mag)	SNooPy (mag)
SN1998bu	CfA	30.214 ± 0.052	30.562 ± 0.009
SN2005cf	CfA	32.327 ± 0.056	32.355 ± 0.017
SN2006D	CfA	32.923 ± 0.060	32.877 ± 0.015
SN2006lf	CfA	33.153 ± 0.196	33.254 ± 0.013
SN2008gb	CfA	36.062 ± 0.079	35.920 ± 0.042
SN2008hs	CfA	34.721 ± 0.072	34.649 ± 0.036
SN2009al	CfA	34.916 ± 0.064	35.065 ± 0.045
SN2009an	CfA	33.236 ± 0.059	33.225 ± 0.013
SN2009bv	CfA	36.292 ± 0.064	36.204 ± 0.036
SN2010ai	CfA	35.051 ± 0.062	34.895 ± 0.029
SN2010kg	CfA	33.814 ± 0.062	33.999 ± 0.018
SN2011ao	CfA	33.130 ± 0.057	33.359 ± 0.056
SN2011B	CfA	31.585 ± 0.055	31.678 ± 0.014
SN2011by	CfA	31.898 ± 0.052	31.953 ± 0.012
SN2011df	CfA	33.909 ± 0.060	33.999 ± 0.022
SN1999ee	CSP	33.138 ± 0.048	33.454 ± 0.010
SN2000ca	CSP	34.933 ± 0.058	34.910 ± 0.014
SN2001ba	CSP	35.607 ± 0.100	35.609 ± 0.020
SN2004eo	CSP	33.884 ± 0.054	33.823 ± 0.017
SN2004ey	CSP	34.096 ± 0.057	33.991 ± 0.006
SN2005el	CSP	34.070 ± 0.057	33.853 ± 0.015
SN2005iq	CSP	35.903 ± 0.057	35.771 ± 0.011
SN2005kc	CSP	33.936 ± 0.057	34.038 ± 0.013
SN2005ki	CSP	34.589 ± 0.057	34.479 ± 0.007
SN2006ax	CSP	34.329 ± 0.053	34.284 ± 0.010
SN2006bh	CSP	33.292 ± 0.055	33.178 ± 0.011
SN2006bt	CSP	35.672 ± 0.052	35.429 ± 0.060
SN2006kf	CSP	34.686 ± 0.077	34.602 ± 0.017
SN2007A	CSP	34.447 ± 0.057	34.436 ± 0.025
SN2007af	CSP	31.993 ± 0.053	32.041 ± 0.015
SN2007ai	CSP	35.695 ± 0.081	35.742 ± 0.023
SN2007as	CSP	34.848 ± 0.049	34.273 ± 0.015
SN2007bc	CSP	34.588 ± 0.057	34.645 ± 0.020
SN2007bd	CSP	35.554 ± 0.059	35.467 ± 0.027
SN2007ca	CSP	34.343 ± 0.053	34.462 ± 0.012
SN2007jg	CSP	36.189 ± 0.062	36.014 ± 0.039
SN2007le	CSP	32.117 ± 0.053	32.330 ± 0.014
SN2008ar	CSP	35.274 ± 0.057	35.279 ± 0.010
SN2008bc	CSP	34.074 ± 0.047	33.990 ± 0.010
SN2008bf	CSP	35.083 ± 0.054	34.979 ± 0.010
SN2008gp	CSP	35.659 ± 0.055	35.584 ± 0.012
SN2008hj	CSP	35.943 ± 0.056	35.905 ± 0.013
SN2008hv	CSP	33.715 ± 0.054	33.691 ± 0.011
SN2009aa	CSP	35.318 ± 0.056	35.284 ± 0.007
SN2009ad	CSP	35.328 ± 0.056	35.289 ± 0.011
SN2009ag	CSP	33.219 ± 0.064	33.261 ± 0.025
SN2009cz	CSP	34.797 ± 0.057	34.803 ± 0.017
SN2009D	CSP	34.965 ± 0.054	34.930 ± 0.015
SN2009Y	CSP	32.700 ± 0.053	32.650 ± 0.034
SN1999ek	Others	34.380 ± 0.092	34.517 ± 0.017
SN2000E	Others	31.655 ± 0.060	31.756 ± 0.028
SN2001bt	Others	33.691 ± 0.057	33.836 ± 0.016
SN2001cz	Others	33.964 ± 0.056	34.026 ± 0.011
SN2001el	Others	31.457 ± 0.055	31.479 ± 0.017
SN2002dj	Others	32.810 ± 0.056	32.899 ± 0.014
SNf20080514-002	Others	35.102 ± 0.061	34.933 ± 0.017

Note— Distance moduli estimated by fitting the optical BVR bands for the same 56 supernovae listed in Table 12 using the SALT2 and SNooPy fitters. The Hubble diagrams for these 2 cases are shown in Fig. 9.

Combining the growing low-redshift SN Ia in NIR samples from the CfA, CSP, and other samples in the literature with higher redshift optical and NIR data sets will continue to lay the foundation for ongoing and future, ground and space-based, supernova cosmology experiments, which seek to further test whether dark energy is best described by Einstein's cosmological constant Λ or some other physical mechanism that varies on cosmic timescales.

Acknowledgments

The authors would like to thank Michael Wood-Vasey and Anja Weyant for help compiling redshifts for the nearby sample. We would also like to thank Dan Scolnic and Michael Foley for help determining the local flow corrected redshifts for our sample. We further thank Saurabh Jha, Suhail Dhawan, and Gautham Narayan for useful conversations. A.A. acknowledges support from the Harvard-Mexico fellowship sponsored by Fundación México en Harvard and CONACyT. A.S.F. acknowledges support from NSF Awards SES 1056580 and PHYS 1541160. R.P.K. acknowledges NSF Grants AST-1516854, AST 12-11196, AST 09-097303, and AST 06-06772. R.P.K, A.S.F, K.M. and A.A acknowledge Hubble Space Telescope Awards HST GO-14216 and HST GO-13046 supporting the HST RAISIN program. D.O.J. is supported by a Gordon and Betty Moore Foundation postdoctoral fellowship at the University of California, Santa Cruz. We gratefully made use of the NASA/IPAC Extragalactic Database (NED). The NASA/IPAC Extragalactic Database (NED) Is operated by the Jet Propulsion Laboratory, California Institute of Technology, under contract with NASA. This publication makes use of data products from the 2MASS Survey, funded by NASA and the US National Science Foundation (NSF). IAUC/CBET were very useful.

APPENDIX

A. GAUSSIAN PROCESS REGRESSION

Given the dataset of observations in an absolute magnitude NIR LC, $(\mathbf{M}, \mathbf{t})$ for a given supernova, we want to use this information to estimate the latent absolute magnitudes $\boldsymbol{\mathcal{M}}^*$ at a grid of phases $\mathbf{t}^*$ described in Section 3.2. To do so, we define a Gaussian process with these data and variables.

To model the covariance $\mathrm{Cov}[\boldsymbol{\mathcal{M}}^*, \boldsymbol{\mathcal{M}}^{*\top}]$ we choose the squared exponential GP kernel that is defined as

$$k(t_i, t_j) = \sigma_K^2 \exp\left[-\frac{(t_i - t_j)^2}{2l^2}\right], \tag{A1}$$

where σ_K and l are the GP kernel hyperparameters that we explain how to compute at the end of this section. We choose the GP kernel of Eq. (A1) because it is simple, produces smooth curves, and has the general properties we need to model the observed shapes of the NIR LCs: for two phases very close to each other, $t_i \sim t_j$, their covariance is close to 1, and for distant phases, $t_i \ll t_j$, then $k(t_i, t_j) \sim 0$, such that they are almost uncorrelated.

We also take into account the uncertainty associated with each datum $M(t_i)$ in the variance $\sigma_M^2 = \sigma_m^2 + \sigma_A^2 + \sigma_{\mathrm{Kcorr}}^2 + \sigma_{\mu_{\mathrm{pec}}}^2$ [see Eq. (7) for details], by defining the total covariance between two data points as

$$\mathrm{Cov}[M_i, M_j] = k(t_i, t_j) + \delta_{ij}(\sigma_m^2 + \sigma_{\mathrm{Kcorr}}^2) + \sigma_{\mu_{\mathrm{pec}}}^2 + \sigma_A^2 \tag{A2}$$

where δ_{ij} is the Kronecker delta function, and we assume that the measurement and K-correction errors are independent between two different M_i and M_j, but that both the peculiar velocity-distance error and the Milky Way extinction error are not independent at different times because they are the same over the whole LC in a single filter for a given supernova. In matrix notation we can write Eq. (A2) for all the data $\mathbf{M}$ in a LC as

$$\mathrm{Cov}[\mathbf{M}, \mathbf{M}^\top] = \mathbf{K}(\mathbf{t}, \mathbf{t}) + \mathbf{W} + (\sigma_{\mu_{\mathrm{pec}}}^2 + \sigma_A^2)\mathbf{1} \cdot \mathbf{1}^\top, \tag{A3}$$

where $\mathbf{K}(\mathbf{t}, \mathbf{t})$ is a square matrix with elements given by Eq. (A1), $\mathbf{W}$ is a diagonal matrix of dimension $n \times n$ with elements given by

$$W_{ij} = \delta_{ij}\left(\sigma_m^2 + \sigma_{\mathrm{Kcorr}}^2\right), \tag{A4}$$

and $\mathbf{1}$ is a vector of ones, so that the term $(\sigma_{\mu_{\mathrm{pec}}}^2 + \sigma_A^2)\mathbf{1} \cdot \mathbf{1}^\top$, is a square matrix of dimension $n \times n$ with elements all equal to $(\sigma_{\mu_{\mathrm{pec}}}^2 + \sigma_A^2)$.

Following the standard GP formalism (e.g., Chapter 2 of Rasmussen & Williams (2006)), we first write the joint distribution of the observed absolute magnitudes, $\mathbf{M}$, and latent absolute magnitudes, $\boldsymbol{\mathcal{M}}^*$, with a constant prior mean as

$$\begin{bmatrix} \mathbf{M} \\ \boldsymbol{\mathcal{M}}^* \end{bmatrix} \sim \mathcal{N}\left(\begin{bmatrix} a\mathbf{1} \\ a\mathbf{1}^* \end{bmatrix}, \begin{bmatrix} \mathbf{K}(\mathbf{t}, \mathbf{t}) + \mathbf{W} + (\sigma_{\mu_{\mathrm{pec}}}^2 + \sigma_A^2)\mathbf{1} \cdot \mathbf{1}^\top & \mathbf{K}(\mathbf{t}, \mathbf{t}^*) \\ \mathbf{K}(\mathbf{t}^*, \mathbf{t}) & \mathbf{K}(\mathbf{t}^*, \mathbf{t}^*) \end{bmatrix}\right) \tag{A5}$$

where $\mathbf{1}$ and $\mathbf{1}^*$ are vectors of ones and of dimensions n and n^* respectively, and a is a scalar that we assign the value of $-17.5, -17, -18$ and -18 mag for the Y, J, H and K_s bands, respectively. We assume these values of a just for computational convenience in the GP fitting, and verified that the final templates are insensitive to these choices over a wide range of values for a. The matrices $\mathbf{K}(\mathbf{t}, \mathbf{t})$, $\mathbf{K}(\mathbf{t}^*, \mathbf{t})$, $\mathbf{K}(\mathbf{t}, \mathbf{t}^*)$, and $\mathbf{K}(\mathbf{t}^*, \mathbf{t}^*)$, are of dimensions $n \times n$, $n^* \times n$, $n \times n^*$ and $n^* \times n^*$ respectively, with elements defined by Eq. (A1).

The conditional distribution of $\boldsymbol{\mathcal{M}}^*$ given $\mathbf{t}, \mathbf{t}^*$ and $\mathbf{M}$, can be written as

$$\boldsymbol{\mathcal{M}}^* | \mathbf{t}, \mathbf{t}^*, \mathbf{M} \;\sim\; \mathcal{N}\left(\boldsymbol{\mu}^{\mathrm{post}}, \boldsymbol{\Sigma}^{\mathrm{post}}\right) \tag{A6}$$

where the posterior mean $\boldsymbol{\mu}^{\mathrm{post}}$ and posterior covariance $\boldsymbol{\Sigma}^{\mathrm{post}}$ are given as

$$\boldsymbol{\mu}^{\mathrm{post}} \equiv \mathbb{E}[\boldsymbol{\mathcal{M}}^* | \mathbf{t}, \mathbf{t}^*, \mathbf{M}] = a\mathbf{1} + \mathbf{K}(\mathbf{t}^*, \mathbf{t})\left[\mathbf{K}(\mathbf{t}, \mathbf{t}) + \mathbf{W} + (\sigma_{\mu_{\mathrm{pec}}}^2 + \sigma_A^2)\mathbf{1} \cdot \mathbf{1}^\top\right]^{-1} (\mathbf{M} - a\mathbf{1}) \tag{A7}$$

$$\boldsymbol{\Sigma}^{\mathrm{post}} \equiv \mathrm{Cov}\left[\boldsymbol{\mathcal{M}}^*, \boldsymbol{\mathcal{M}}^{*\top} | \, \mathbf{t}, \mathbf{t}^*, \mathbf{M}\right] = \mathbf{K}(\mathbf{t}^*, \mathbf{t}^*) - \mathbf{K}(\mathbf{t}^*, \mathbf{t})\left[\mathbf{K}(\mathbf{t}, \mathbf{t}) + \mathbf{W} + (\sigma_{\mu_{\mathrm{pec}}}^2 + \sigma_A^2)\mathbf{1} \cdot \mathbf{1}^\top\right]^{-1} \mathbf{K}(\mathbf{t}, \mathbf{t}^*) \tag{A8}$$

Table 15. Values of the GP hyperparameters

band	l	σ_K
Y	7.90	0.70
J	7.02	0.95
H	9.81	0.75
K_s	8.19	0.55

The final values we obtain from the GP regression are the vector $\boldsymbol{\mu}^{\text{post}}$ and the matrix $\boldsymbol{\Sigma}^{\text{post}}$, that we estimate using Eqs. (A7) and (A8) respectively.

The coefficients σ_K and l in Eq. (A1) are called the *hyperparameters* of the GP kernel that we determine by assuming that the LCs for all the SN in a given NIR band are independent of each other, and that the GP hyperparameters describe the *population* of the SN LCs in a given band rather than each individual LC. With these assumptions, we can write the global marginal likelihood distribution

$$p\Big(\{\mathbf{M}\}_s|\{\mathbf{t}\}_s, \sigma_K, l\Big) \;=\; \prod_{s=1}^{N_{\text{T}}} \mathcal{N}\left(\mathbf{M}_s \mid a\, \mathbf{1}_s,\; \mathbf{K}_s(\mathbf{t}_s, \mathbf{t}_s) + \mathbf{W}_s(\mathbf{t}_s, \mathbf{t}_s) + (\sigma^2_{\mu_{\text{pec}},s} + \sigma^2_{A,s})\mathbf{1}_s \cdot \mathbf{1}_s^{\top}\right), \tag{A9}$$

where the subindex s refers to quantities for supernova s, N_{T} is the number of SN Ia used to construct the normalized LC template in a given NIR band, and "$\{\ \}_s$" means the collection of values from all the N_{T} SN Ia. To compute the MLE values for (σ_K, l), we minimize the negative of the logarithm of Eq. (A9), obtaining the values shown in Table 15.

A.1. *Normalization of the GP light curves*

In Section 3.2.1, we explained that we are primarily interested in the *shape* of the light curves. For this reason, after determining the posterior light curve described by $(\boldsymbol{\mu}^{\text{post}}, \boldsymbol{\Sigma}^{\text{post}})$, we *normalize* the LC using $t_{B\max}$ as the reference time where the light curve will have a value of zero.

First, for computational convenience, we rewrite the linear transformation of Eq. (9) as the matrix operation

$$\mathbf{L} = \mathbf{A}\boldsymbol{\mathcal{M}}^* \tag{A10}$$

where $\mathbf{A}$ is a $n^* \times n^*$ square matrix defined as $\mathbf{A} \equiv \mathbf{I} - \mathbf{V}_k$, where $\mathbf{I}$ is the identity matrix, and $\mathbf{V}_k$ is a matrix containing only 1s in the kth column and zeros everywhere else, assuming that the kth element of $\mathbf{t}^*$ correspond to phase $t^*_k = t_{B\max}$.

We compute the mean of the normalized LC as, $\boldsymbol{\mu}^{\text{L}} = \mathbb{E}[\mathbf{L}|\mathcal{D}] = \mathbf{A}\ \mathbb{E}[\boldsymbol{\mathcal{M}}^*|\mathcal{D}] = \mathbf{A}\boldsymbol{\mu}^{\text{post}}$, where $\mathcal{D} \equiv (\mathbf{t}, \mathbf{t}^*, \mathbf{M})$ is the conditional data in Eq (A6). And the covariance is given by

$$\boldsymbol{\Sigma}^{\text{L}} = \mathbf{A}\boldsymbol{\Sigma}^{\text{post}}\mathbf{A}^{\top}. \tag{A11}$$

From these expressions at $t^*_k = t_{B\max}$, the posterior mean and variance of the normalized LCs are both identically zero:

$$\mathbb{E}[L_k|\mathcal{D}] = 0, \qquad \text{Var}[L_k, L_k|\mathcal{D}] = 0, \tag{A12}$$

which is required for self-consistency with the definition of the normalized LC.

B. HIERARCHICAL BAYESIAN MODEL

Using Bayes' theorem, applying the product rule for probability, and assuming conditional independence of the means of the normalized LCs, μ^{L}_s's, with respect to the population mean and variance $(\theta, \sigma^2_\theta)$, we can write the joint posterior distribution in our hierarchical model as

$$p\left(\{\eta_s\}, \theta, \sigma_\theta|\{\mu^{\text{L}}_s, \sigma_{\eta,s}\}\right) \propto p\left(\theta, \sigma_\theta\right) \times p\left(\{\eta_s\}|\theta, \sigma_\theta\right) \times p\left(\{\mu^{\text{L}}_s\}|\{\eta_s\}, \{\sigma_{\eta,s}\}\right). \tag{B13}$$

Inserting Eqs. (10) and (11) into Eq. (B13), we obtain,

$$p\left(\{\eta_s\},\theta,\sigma_\theta|\{\mu^{\rm L}_s,\sigma_{\eta,s}\}\right) \propto p\left(\theta,\sigma_\theta\right) \times \prod_{s=1}^{N^*_{\rm T}} \mathcal{N}\left(\eta_s|\theta,\sigma^2_\theta\right) \times \prod_{s=1}^{N^*_{\rm T}} \mathcal{N}\left(\mu^{\rm L}_s|\eta_s,\sigma^2_{\eta,s}\right). \tag{B14}$$

where $N^*_{\rm T}$ is the number of supernovae for which we have determined the best fitting function at phase t^*. Note that since each LC has a *different* number of photometric data points over *different* phase ranges, this implies that $N^*_{\rm T}$ is different for each phase t^*.

For computation convenience, following Gelman et al. (2014), we decompose the joint posterior distribution using the product rule as

$$p\left(\{\eta_s\},\theta,\sigma_\theta|\{\mu^{\rm L}_s,\sigma_{\eta,s}\}\right) \propto p\left(\{\eta_s\}|\theta,\sigma_\theta,\{\mu^{\rm L}_s,\sigma_{\eta,s}\}\right) \times p\left(\theta|\sigma_\theta,\{\mu^{\rm L}_s,\sigma_{\eta,s}\}\right) \times p\left(\sigma_\theta|\{\mu^{\rm L}_s,\sigma_{\eta,s}\}\right), \tag{B15}$$

where the first factor to the right of the proportionality sign of Eq. (B15) can be written for the supernova s as

$$p\left(\eta_s|\theta,\sigma_\theta,\mu^{\rm L}_s,\sigma_{\eta,s}\right) = \mathcal{N}\left(\eta_s|\rho_s,R_s\right), \tag{B16}$$

where

$$\rho_s \equiv \frac{\mu^{\rm L}_s/\sigma^2_{\eta,s}+\theta/\sigma^2_\theta}{1/\sigma^2_{\eta,s}+1/\sigma^2_\theta}, \tag{B17}$$

and

$$R_s \equiv \frac{1}{1/\sigma^2_{\eta,s}+1/\sigma^2_\theta}. \tag{B18}$$

The middle factor to the right of the proportionality sign of Eq. (B15) can be written as

$$p\left(\theta\,|\,\sigma_\theta,\{\mu^{\rm L}_s,\sigma_{\eta,s}\}\right) = \mathcal{N}\left(\theta\,|\,\hat\theta,R\right), \tag{B19}$$

where

$$\hat\theta \equiv \frac{\sum_{s=1}^{N^*_{\rm T}} \mu^{\rm L}_s\left(\sigma^2_{\eta,s}+\sigma^2_\theta\right)^{-1}}{\sum_{s=1}^{N_{\rm SN}}\left(\sigma^2_{\eta,s}+\sigma^2_\theta\right)^{-1}}, \tag{B20}$$

and

$$R^{-1} \equiv \sum_{s=1}^{N^*_{\rm T}} \frac{1}{\sigma^2_{\eta,s}+\sigma^2_\theta}. \tag{B21}$$

Finally, the last term to the right of the proportionality sign can be written as

$$p\left(\sigma_\theta|\{\mu^{\rm L}_s,\sigma_{\eta,s}\}\right) \propto R^{1/2}\prod_{s=1}^{N^*_{\rm T}}\left(\sigma^2_{\eta,s}+\sigma^2_\theta\right)^{-1/2}\exp\left(\frac{-(\mu^{\rm L}_s-\hat\theta)^2}{2(\sigma^2_{\eta,s}+\sigma^2_\theta)}\right), \tag{B22}$$

where we are assuming a uniform prior distribution $p(\sigma_\theta)\propto 1$.

We use Eq. (B15) combined with Eqs. (B16)-(B22) to simultaneously determine the posterior best estimates of $(\{\eta_s\},\theta,\sigma_\theta)$ at phase t^*, given the data $\{\mu^{\rm L}_s,\sigma_{\eta,s}\}$, following the computational procedure described in Appendix C.3, subsection "Marginal and conditional simulation for the normal model", of Gelman et al. (2014). We use the R code presented there to build our R code to make the computations described in this work.

C. RMS, WEIGHTED RMS, AND THE INTRINSIC SCATTER

We use the RMS to quantify the scatter in the Hubble residuals because it is simple and straightforward to compute and compare with the Hubble residuals reported by other authors. The definition we use is

$$\mathrm{RMS} = \sqrt{N_{\mathrm{SN}}^{-1}\left(\sum_{s=1}^{N_{\mathrm{SN}}} \Delta\mu_s^2\right)}\,, \tag{C23}$$

where N_{SN} is the total number of SN Ia in the Hubble diagram. We compute the uncertainty on RMS using bootstrap resampling.

To weight the root mean square (RMS) by the uncertainties in each SN distance modulus estimate in each NIR band, we compute the inverse-variance weighted root mean square (wRMS) of the residuals as

$$\mathrm{wRMS} = \sqrt{\left(\sum_{s=1}^{N_{\mathrm{SN}}} w_s\right)^{-1} \sum_{s=1}^{N_{\mathrm{SN}}} w_s\, \Delta\mu_s^2}\,, \tag{C24}$$

where $w_s \equiv 1/(\hat{\sigma}^2_{\mathrm{fit},s} + \hat{\sigma}^2_{\mathrm{int}} + \sigma^2_{\mu_{\mathrm{pec}},s})$ and $\Delta\mu_s$ is defined in Eq. (21). We also compute the uncertainty on wRMS using bootstrap resampling.

We determine the *intrinsic scatter*, σ_{int}, in the Hubble residual following the procedure described in Eqs. (B.6)-(B.7) in Appendix B of Blondin et al. (2011). This dispersion tries to quantify the scatter due to intrinsic differences in the NIR SN Ia absolute magnitudes only and *not* due to the peculiar-velocity uncertainty of each SN. The intrinsic scatter corresponds to the remaining dispersion observed in the Hubble-diagram residuals *after* accounting for the uncertainty in distance modulus due to the peculiar-velocity uncertainty, $\sigma^2_{\mu_{\mathrm{pec}},s}$, and the photometric errors $\{\hat{\sigma}_{\mathrm{fit},s}\}$. When comparing our notation to Eqs. (B.6)-(B.7) of Blondin et al. (2011), note that where we use $\sigma_{\mathrm{fit},s}$, σ_{int} and $\sigma_{\mu_{\mathrm{pec}},s}$, Blondin et al. (2011) instead uses the notation $\sigma_{m,s}$, σ_{pred}, and $\sigma_{\mathrm{pec},s}$, respectively.

D. COVARIANCE MATRIX C_μ OF HUBBLE RESIDUALS

In this section we provide the numerical values for different cases of the covariance matrix C_μ.

For the template method, we find the following values of the sample covariance matrix C_μ for the YJH bands:

$$C_\mu = \begin{pmatrix} 0.0227 & 0.0192 & 0.0167 \\ 0.0192 & 0.0246 & 0.0201 \\ 0.0167 & 0.0201 & 0.0211 \end{pmatrix}\,, \tag{D25}$$

and for the JHK_s bands:

$$C_\mu = \begin{pmatrix} 0.0356 & 0.0276 & 0.0202 \\ 0.0276 & 0.0317 & 0.0237 \\ 0.0202 & 0.0237 & 0.0426 \end{pmatrix}\,. \tag{D26}$$

For the GP method, we find the following values for the sample covariance matrix for the YJH bands:

$$C_\mu = \begin{pmatrix} 0.0109 & 0.0110 & 0.0080 \\ 0.0110 & 0.0133 & 0.0084 \\ 0.0080 & 0.0084 & 0.0080 \end{pmatrix}\,, \tag{D27}$$

and for the JHK_s bands:

$$C_\mu = \begin{pmatrix} 0.0279 & 0.0217 & 0.0213 \\ 0.0217 & 0.0238 & 0.0192 \\ 0.0213 & 0.0192 & 0.0283 \end{pmatrix}\,. \tag{D28}$$

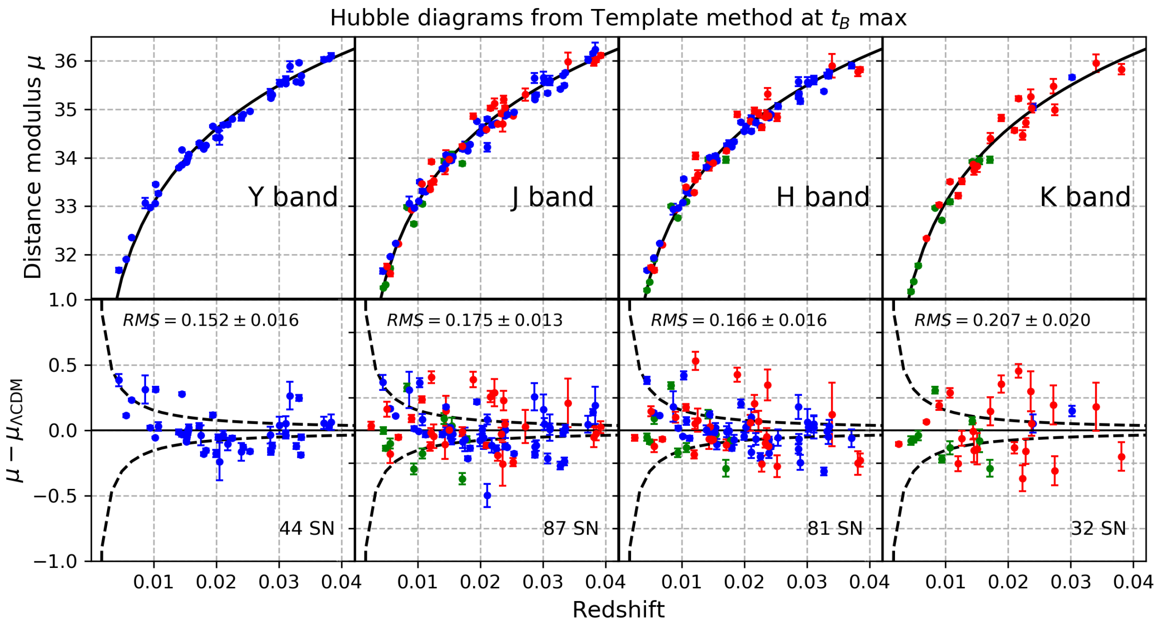

Figure 11. Individual $YJHK_s$ Hubble diagrams (top row) and residuals (bottom row) using the template method. Points are color coded by NIR photometric data source, including the CfA (red; Wood-Vasey et al. 2008; Friedman et al. 2015), the CSP (blue; Krisciunas et al. 2017), and other data from the literature (green; see Table 2). Note that only the CSP used a Y-band filter. In Table 11, we report the numerical values of the distance moduli shown in this figure. Table 8 shows the intrinsic scatter in the Hubble diagram.

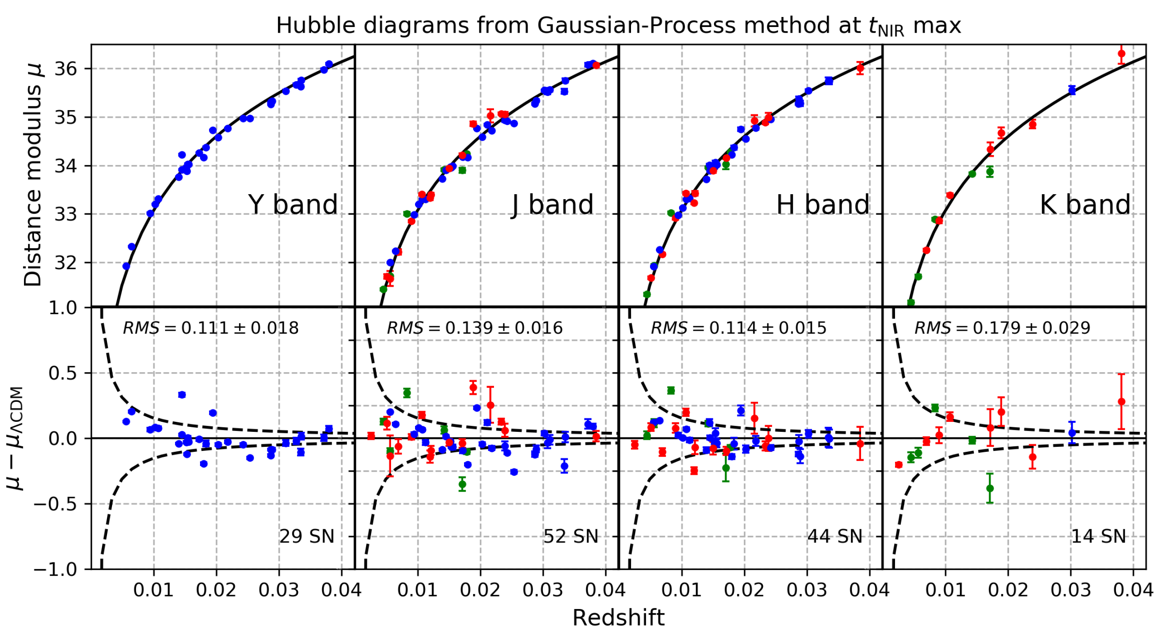

Figure 12. Individual $YJHK_s$ Hubble diagrams (top row) and residuals (bottom row) using the Gaussian-process method at NIR max. See the caption of Fig. 11. In Table 12, we report the numerical values of the distance moduli shown in this figure.

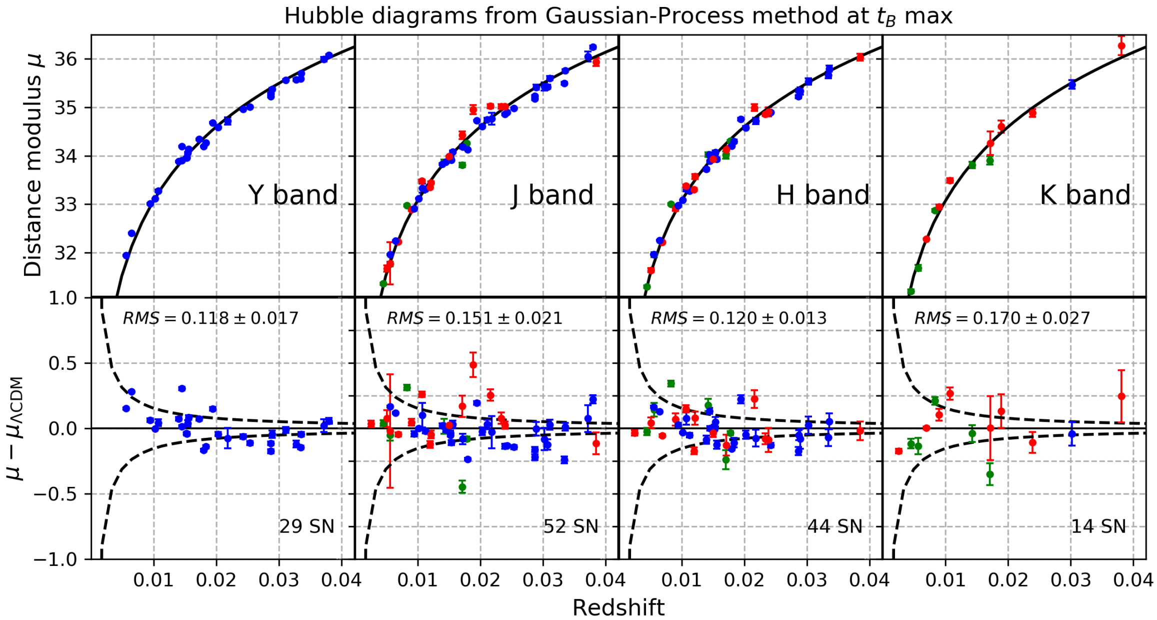

Figure 13. Individual $YJHK_s$ Hubble diagrams (top row) and residuals (bottom row) using the Gaussian-process method at B max. See the caption of Fig. 11. In Table 13, we report the numerical values of the distance moduli shown in this figure.

REFERENCES

Alam, S., et al. 2017, MNRAS, 470, 2617

Albareti, F. D., et al. 2017, ApJS, 233, 25

Astier, P., Guy, J., Pain, R., & Balland, C. 2011, A&A, 525, A7

Astier, P., et al. 2006, A&A, 447, 31

Barone-Nugent, R. L., et al. 2012, MNRAS, 425, 1007

—. 2013, MNRAS, 432, 90

Beaulieu, J. P., et al. 2010, in Astronomical Society of the Pacific Conference Series, Vol. 430, Pathways Towards Habitable Planets, ed. V. Coudé Du Foresto, D. M. Gelino, & I. Ribas, 266

Betoule, M., et al. 2014, A&A, 568, A22

Blondin, S., Mandel, K. S., & Kirshner, R. P. 2011, Astronomy and Astrophysics, 526, A81

Blondin, S., & Tonry, J. L. 2007, ApJ, 666, 1024

Brout, D., et al. 2018a, arXiv e-prints

—. 2018b, arXiv e-prints

Burns, C. R., et al. 2011, The Astronomical Journal, 141, 19

Burns, C. R., et al. 2014, ApJ, 789, 32

—. 2018, ApJ, 869, 56

Campbell, H., et al. 2013, ApJ, 763, 88

Cardelli, J. A., Clayton, G. C., & Mathis, J. S. 1989, ApJ, 345, 245

Cardona, W., Kunz, M., & Pettorino, V. 2017, JCAP, 3, 056

Carrick, J., Turnbull, S. J., Lavaux, G., & Hudson, M. J. 2015, MNRAS, 450, 317

Cartier, R., et al. 2014, ApJ, 789, 89

Childress, M., et al. 2011, ApJ, 733, 3

—. 2013, ApJ, 770, 107

Clampin, M. 2011, in Society of Photo-Optical Instrumentation Engineers (SPIE) Conference Series, Vol. 8146, Society of Photo-Optical Instrumentation Engineers (SPIE) Conference Series

Conley, A., Carlberg, R. G., Guy, J., Howell, D. A., Jha, S., Riess, A. G., & Sullivan, M. 2007, ApJL, 664, L13

Conley, A., et al. 2008, ApJ, 681, 482

—. 2011, ApJS, 192, 1

Contreras, C., et al. 2010, AJ, 139, 519

Courtois, H. M., & Tully, R. B. 2012, ApJ, 749, 174

D'Andrea, C. B., et al. 2018, arXiv e-prints

Dark Energy Survey Collaboration et al. 2016, MNRAS, 460, 1270

Davis, T. M., & Parkinson, D. 2016, ArXiv e-prints

Davis, T. M., et al. 2011, ApJ, 741, 67

DES Collaboration et al. 2018a, arXiv e-prints

—. 2018b, arXiv e-prints

—. 2018c, arXiv e-prints

Dhawan, S., Jha, S. W., & Leibundgut, B. 2018, A&A, 609, A72

Dhawan, S., Leibundgut, B., Spyromilio, J., & Maguire, K. 2015, MNRAS, 448, 1345
Efstathiou, G. 2014, MNRAS, 440, 1138
Folatelli, G., et al. 2010, AJ, 139, 120
Foley, R., Kirshner, R., Challis, P., Rest, A., Chornock, R., Riess, A., Scolnic, D., & Stubbs, C. 2013a, RAISIN: Tracers of Cosmic Expansion with SN Ia in the IR, NOAO Proposal
—. 2013b, RAISIN: Tracers of Cosmic Expansion with SN Ia in the IR, NOAO Proposal
Foley, R. J., et al. 2018, MNRAS, 475, 193
Freedman, W. L., et al. 2001, ApJ, 553, 47
Friedman, A. S. 2012, PhD thesis, Harvard University
Friedman, A. S., et al. 2015, ApJS, 220, 9
Frieman, J. A., Turner, M. S., & Huterer, D. 2008, Ann. Rev. Astron. Astrophys., 46, 385
Gehrels, N. 2010, arXiv:1008.4936
Gelman, A., Carlin, J. B., Stern, H. S., Dunson, D. B., Vehtari, A., & Rubin, D. B. 2014, Bayesian Data Analysis, third edition edn., Texts in Statistical Science (CRC Press)
Goldhaber, G., et al. 2001, ApJ, 558, 359
Goobar, A. 2015, in Thirteenth Marcel Grossmann Meeting: On Recent Developments in Theoretical and Experimental General Relativity, Astrophysics and Relativistic Field Theories, ed. K. Rosquist, 167–178
Goobar, A., & Leibundgut, B. 2011, Annual Review of Nuclear and Particle Science, 61, 251
Greenhouse, M. A. 2016, in Proc. SPIE, Vol. 9904, Space Telescopes and Instrumentation 2016: Optical, Infrared, and Millimeter Wave, 990406
Guy, J., Astier, P., Nobili, S., Regnault, N., & Pain, R. 2005, A&A, 443, 781
Guy, J., et al. 2007, A&A, 466, 11
—. 2010, A&A, 523, A7
Hamuy, M., Phillips, M. M., Suntzeff, N. B., Schommer, R. A., Maza, J., Smith, R. C., Lira, P., & Aviles, R. 1996, AJ, 112, 2438
Hicken, M., Wood-Vasey, W. M., Blondin, S., Challis, P., Jha, S., Kelly, P. L., Rest, A., & Kirshner, R. P. 2009a, ApJ, 700, 1097
Hicken, M., et al. 2009b, ApJ, 700, 331
—. 2012, ApJS, 200, 12
Hounsell, R., et al. 2017, ArXiv e-prints
Hsiao, E. Y., Conley, A., Howell, D. A., Sullivan, M., Pritchet, C. J., Carlberg, R. G., Nugent, P. E., & Phillips, M. M. 2007, ApJ, 663, 1187
Hsiao, E. Y., et al. 2019, PASP, 131, 014002
Ivezic, Z., et al. 2008, ArXiv e-prints
Jha, S., Riess, A. G., & Kirshner, R. P. 2007, ApJ, 659, 122
Jha, S., et al. 2006, AJ, 131, 527
Jones, D. O., et al. 2018, ApJ, 857, 51
Kattner, S., et al. 2012, PASP, 124, 114
Kessler, R., et al. 2009, ApJS, 185, 32
Kessler, R., et al. 2009, Publications of the Astronomical Society of the Pacific, 121, 1028
Kessler, R., et al. 2018, arXiv e-prints
Kirshner, R. 2012, RAISIN: Tracers of cosmic expansion with SN IA in the IR, HST Proposal
Kirshner, R. P. 2013, in IAU Symposium, Vol. 281, IAU Symposium, ed. R. Di Stefano, M. Orio, & M. Moe, 1–8
Kirshner, R. P., & The RAISIN TEAM. 2014, in American Astronomical Society Meeting Abstracts, Vol. 223, American Astronomical Society Meeting Abstracts #223, 116.10
Komatsu, E., et al. 2011, ApJS, 192, 18
Krisciunas, K., Hastings, N. C., Loomis, K., McMillan, R., Rest, A., Riess, A. G., & Stubbs, C. 2000, ApJ, 539, 658
Krisciunas, K., Phillips, M. M., & Suntzeff, N. B. 2004a, ApJL, 602, L81
Krisciunas, K., et al. 2003, AJ, 125, 166
—. 2004b, AJ, 127, 1664
—. 2004c, AJ, 128, 3034
—. 2005, AJ, 130, 350
—. 2007, AJ, 133, 58
—. 2009, AJ, 138, 1584
—. 2017, ArXiv e-prints
Leloudas, G., et al. 2009, A&A, 505, 265
Mandel, K. S., Foley, R. J., & Kirshner, R. P. 2014, ApJ, 797, 75
Mandel, K. S., Narayan, G., & Kirshner, R. P. 2011, ApJ, 731, 120
Mandel, K. S., Scolnic, D. M., Shariff, H., Foley, R. J., & Kirshner, R. P. 2017, ApJ, 842, 93
Mandel, K. S., Wood-Vasey, W. M., Friedman, A. S., & Kirshner, R. P. 2009, ApJ, 704, 629
Meikle, W. P. S. 2000, MNRAS, 314, 782
Mosher, J., et al. 2014, ApJ, 793, 16
Mould, J. R., et al. 2000, ApJ, 529, 786
Narayan, G., et al. 2016, ApJS, 224, 3
Narayan, G. S. 2013, PhD thesis, Harvard University
O'Donnell, J. E. 1994, The Astrophysical Journal, 422, 158
Perlmutter, S., et al. 1997, ApJ, 483, 565
—. 1999, ApJ, 517, 565
Phillips, M. M. 1993, ApJL, 413, L105
—. 2012, PASA, 29, 434
Phillips, M. M., Lira, P., Suntzeff, N. B., Schommer, R. A., Hamuy, M., & Maza, J. 1999, AJ, 118, 1766
Phillips, M. M., et al. 2019, PASP, 131, 014001
Pierel, J. D. R., et al. 2018a, PASP *accepted*

—. 2018b, SNSEDextend: SuperNova Spectral Energy Distributions extrapolation toolkit, Astrophysics Source Code Library
Pignata, G., et al. 2008, MNRAS, 388, 971
Pimbblet, K. A., Penny, S. J., & Davies, R. L. 2014, MNRAS, 438, 3049
Planck Collaboration et al. 2016a, A&A, 594, A8
—. 2016b, A&A, 594, A13
—. 2018, ArXiv e-prints
Prieto, J. L., Rest, A., & Suntzeff, N. B. 2006, ApJ, 647, 501
Prieto, J. L., et al. 2007, ArXiv e-prints
Radburn-Smith, D. J., Lucey, J. R., & Hudson, M. J. 2004, MNRAS, 355, 1378
Rasmussen, C. E., & Williams, C. K. I. 2006, Gaussian Processes for Machine Learning (The MIT Press)
Rest, A., et al. 2013, arXiv:1310.3828
—. 2014, ApJ, 795, 44
Riess, A. G., Press, W. H., & Kirshner, R. P. 1996, ApJ, 473, 88
Riess, A. G., et al. 1998, AJ, 116, 1009
—. 2016, ApJ, 826, 56
—. 2018a, ApJ, 861, 126
—. 2018b, ApJ, 855, 136
—. 2018c, ApJ, 853, 126
Schlafly, E. F., & Finkbeiner, D. P. 2011, The Astrophysical Journal, 737, 103
Schmidt, B. P., et al. 1998, ApJ, 507, 46
Schweizer, F., et al. 2008, AJ, 136, 1482
Scolnic, D., Jones, D., Rest, A., & Pan-STARRS Transients Team. 2017, in American Astronomical Society Meeting Abstracts, Vol. 229, American Astronomical Society Meeting Abstracts, 341.09
Scolnic, D., et al. 2013, arXiv:1310.3824
—. 2014a, ApJ, 795, 45
—. 2015, ApJ, 815, 117
Scolnic, D. M., Riess, A. G., Foley, R. J., Rest, A., Rodney, S. A., Brout, D. J., & Jones, D. O. 2014b, ApJ, 780, 37
Scolnic, D. M., et al. 2018, ApJ, 859, 101
Shariff, H., Dhawan, S., Jiao, X., Leibundgut, B., Trotta, R., & van Dyk, D. A. 2016, MNRAS
Smith, R. M., et al. 2014, in Proc. SPIE, Vol. 9147, Ground-based and Airborne Instrumentation for Astronomy V, 914779
Spergel, D., et al. 2015, ArXiv e-prints
Stanishev, V., et al. 2007, A&A, 469, 645
—. 2018, A&A, 615, A45
Stritzinger, M., et al. 2010, AJ, 140, 2036
Stritzinger, M. D., et al. 2011, AJ, 142, 156
Taddia, F., et al. 2012, A&A, 545, L7
Takanashi, N., Doi, M., & Yasuda, N. 2008, MNRAS, 389, 1577
Tonry, J. L., et al. 2003, ApJ, 594, 1
Tripp, R. 1998, A&A, 331, 815
Tully, R. B., Courtois, H. M., & Sorce, J. G. 2016, AJ, 152, 50
Tully, R. B., et al. 2013, AJ, 146, 86
Valentini, G., et al. 2003, ApJ, 595, 779
Wallner, O., Ergenzinger, K., Tuttle, S., Vaillon, L., & Johann, U. 2017, in Society of Photo-Optical Instrumentation Engineers (SPIE) Conference Series, Vol. 10565, Society of Photo-Optical Instrumentation Engineers (SPIE) Conference Series, 105650K
Wang, L., Goldhaber, G., Aldering, G., & Perlmutter, S. 2003, ApJ, 590, 944
Wang, L., Strovink, M., Conley, A., Goldhaber, G., Kowalski, M., Perlmutter, S., & Siegrist, J. 2006, ApJ, 641, 50
Weinberg, D. H., Mortonson, M. J., Eisenstein, D. J., Hirata, C., Riess, A. G., & Rozo, E. 2013, PhR, 530, 87
Weyant, A., Wood-Vasey, W. M., Allen, L., Garnavich, P. M., Jha, S. W., Joyce, R., & Matheson, T. 2014, ApJ, 784, 105
Weyant, A., et al. 2018, AJ, 155, 201
Wood-Vasey, W. M., et al. 2007, ApJ, 666, 694
—. 2008, ApJ, 689, 377
Zhan, H., & Tyson, J. A. 2017, ArXiv e-prints